㉝ Patentinhaber:

Institut für Physikalische Hochtechnologie e.V.,
07745 Jena, DE

㉞ Vertreter:

Pfeiffer, R., Dipl.-Phys. Fachphys. f. Schutzrechtsw.,
Pat.-Anw., 07745 Jena

㉜ Erfinder:

Andrä, Gudrun, Dr., 07749 Jena, DE; Falk, Fritz, Dr.,
07743 Jena, DE

㊋ Für die Beurteilung der Patentfähigkeit in Betracht
gezogene Druckschriften:

GB   20 19 829 A
GB   20 09 137 A

㊿ Lichtleiter zum Leiten von Licht im Infrarotbereich und Verfahren zu seiner H erstellung

㊐   Lichtleiter zum Leiten von Licht im Infrarotbereich von ≥ 2,5 μm, bestehend aus einem Kern (12) und einem Mantel (11), wobei der Mantel (11) als Kapillare oder als dünnes Rohr (1) ausgebildet ist und aus einem Material besteht, das eine Viskosität zwischen 10^7 bis 10^{13} dPas bei einer Temperatur T_1 aufweist, bei der ein den Kern bildendes Material bereits in Schmelze vorliegt, wobei das Kernmaterial entweder aus Silizium oder aus Germanium besteht.
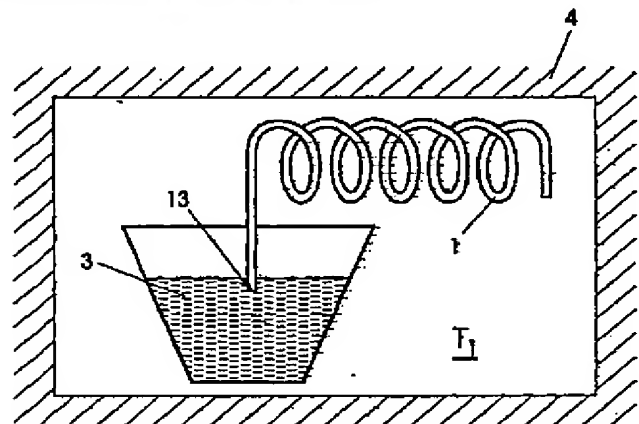
Beschreibung

[0001] Die Erfindung betrifft einen Lichtleiter zum Leiten von Licht im Infrarotbereich bei Wellenlängen $\geq 2,5$ µm, welcher bevorzugt bei Laseranwendungen, wo das Infrarotlicht zur Materialbearbeitung oder -veränderung dient, zum Einsatz gelangt. Insbesondere sollen erfindungsgemäße Lichtleiter in der Laserchirurgie Anwendung finden.

[0002] Als Materialien für Lichtleiter für Wellenlängen oberhalb 2,5 µm sind beispielsweise Fluoridgläser (ZrF_4, HfF_4), Chalkogenid-Gläser (AsS, AsSe, AsSeTe), Erdalkalihalogenid-Gläser (BeF_2, $ZnCl_2$), Silberhalogenidfasern (AgCl/Br), Thallium/Cäsiumhalogenid-Fasern als geeignet bekannt. Daraus gebildete Lichtleitfasern haben für den vorgesehenen bevorzugten Anwendungsfall mindestens einen, meist sogar mehrere der folgenden Nachteile:
die Materialien bzw. daraus gebildete Lichtleiter sind

– toxisch,
– chemisch unbeständig (Wasserlöslichkeit/Hygroskopizität),
– lichtempfindlich, wobei sie zur Degradation unter der zu leitenden IR-Strahlung neigen,
– mechanisch empfindlich, so daß sie nur relativ geringe Krümmungen erlauben.

[0003] Aus diesen Gründen konnten sich derartige Lichtleitfasern bislang in der Lasermedizin nicht durchsetzen, wo neben einer erforderlichen Toxizitätsfreiheit auch Krümmungsradien im Zentimeterbereich gegeben sein müssen. Andere konstruktive Ausführungen zur Lichtleitung, wie mit einer Flüssigkeit (CCl_4) gefüllte Schläuche erweisen sich hierbei wegen der Toxizität als ebenso unbrauchbar, wie innenverspiegelte Metallrohre, die nur geringe Krümmungen ermöglichen.

[0004] In GB 2 009 137 A ist ein Verfahren zur Herstellung IR-leitfähiger Fasern, nämlich das Taylor-Verfahren, beschrieben, bei dem das Kernmaterial in Form von Mischungen aus verschiedenen Materialien in ein Glasrohr mit einem sehr viel größeren Durchmesser als der späteren Lichtleitfaser eingefüllt und erschmolzen wird. Erst danach erfolgt ein Ausziehen des Körpers zu einer Faser unter weiterer Wärmeeinwirkung, wobei es aufgrund der langen Zeiten zu starken chemischen Reaktionen zwischen Kern- und Mantelmaterial kommt. Darüber hinaus reagieren Silizium und Quarzglas bei Temperaturen oberhalb ca. 1200°C zu gasförmigem SiO, weshalb bis heute keine Fasern unter Einsatz von Kernmaterialien aus reinem Germanium oder Silizium bekannt geworden sind.

[0005] Der Erfindung liegt die Aufgabe zugrunde, einen Lichtleiter zum Leiten von Licht im Infrarotbereich von $\geq 2,5$ µm anzugeben, der toxikologisch unbedenklich, wasserunlöslich und chemisch beständig ist und der eine solche mechanische Festigkeit besitzt, daß er bei Durchmessern für Lichtleiter, wie sie bspw. in der Laserchirurgie in Betracht kommen, Krümmungradien im Zentimeterbereich standhält. Auch sollen durch die Erfindung Lichtleiter bereitgestellt werden, die, bei Verzicht auf die gewünschte Verbiegbarkeit, ansonsten die gleichen oben genannten Eigenschaften aufweisen. Weiterhin liegt der Erfindung die Aufgabe zugrunde, ein Verfahren zur Herstellung eines solchen Lichtleiters anzugeben.

[0006] Die Aufgabe der Erfindung wird durch die Merkmale der Patentansprüche 1 und 8 gelöst. Vorteilhafte weitere Ausgestaltungen sind durch die nachgeordneten Ansprüche erfaßt.

[0007] Das Wesen der Erfindung besteht darin, dünne Rohre, insbesondere Kapillaren, aus einem Material, welches Licht im sichtbaren Spektralbereich leitet, mit schmelzflüssigem Germanium oder Silizium zu füllen und anschließend abzukühlen.

[0008] Die Erfindung soll nachstehend anhand von Ausführungsbeispielen näher erläutert werden. Es zeigen:

[0009] Fig. 1 einen Schnitt durch einen Teil des vorgeschlagenen neuen Lichtleiters und

[0010] Fig. 2 schematisch den Aufbau einer Anordnung zur Herstellung des genannten Lichtleiters.

[0011] In einem ersten Ausführungsbeispiel findet eine Kapillare 1, bestehend aus einem Glas, wie z. B. hochschmelzende Borosilicatgläser, Erdalkali-Alumo-Silicatgläser oder Übergangsgläser, Anwendung. Die Materialauswahl für das für die Kapillare 1 in Betracht kommende Glas erfolgt unter der Maßgabe, daß dieses bei einer Temperatur T_1, die geringfügig oberhalb der Schmelztemperatur des den späteren Kern 12 bildenden Kernmaterials liegt, eine Viskosität zwischen 10^7 bis 10^{13} dPas annimmt, und daß es bei den weiter unten beschriebenen Erstarrungszeiten des Kernmaterials zu keinen störenden chemischen Reaktionen zwischen Kern- und Kapillarenmaterial kommt. Im Rahmen der Erfindung ist der Kapillareninnendurchmesser d_2 in einem Bereich von 10 µm bis einige Millimeter, bevorzugt von 10 µm bis 200 µm festlegbar, wobei der Kapillarenwandung 11, insbesondere bei kleinen Kapillareninnendurchmessern, bspw. von 10–100 µm, jeweils eine Wandstärke d_1 gegeben ist, die in der Größenordnung des Kapillareninnendurchmessers d_2 liegt.

[0012] Bei diesem ersten Ausführungsbeispiel wird in einem geeigneten Ofen 4 in einem Tiegel eine Germaniumschmelze bei einer Temperatur T_1 wenig oberhalb ihres Schmelzpunktes vorrätig gehalten. Die nach obigen Maßgaben ausgewählte Glaskapillare 1 wird in den Ofen 4 eingebracht und dadurch ebenfalls auf die Temperatur T_1 erwärmt. Genannte Temperatur T_1 liegt in diesem Ausführungsbeispiel oberhalb 940°C. Bei Erreichen der vorgebbaren Temperatur T_1 wird ein Ende 13 der Kapillare 1 (siehe Fig. 2) in die Germaniumschmelze 3 getaucht. Je nach gewähltem Kapillareninnendurchmesser d_2 wird die Schmelze 3 durch Kapillarwirkung oder mit Hilfe einer nicht dargestellten Pumpe in die Kapillare 1 gesaugt. Ist die Kapillare 1 mit der Schmelze 3 in einer gewünschten Länge gefüllt, wird das Ende 13 aus dem Schmelzbehälter entfernt und die gefüllte Kapillare 1 einer Abkühlung unterworfen, wobei das Kernmaterial 12 erstarrt und der gewünschte Lichtleiter gebildet ist.

[0013] In einem weiteren Ausführungsbeispiel ist die Kapillare 1 aus Quarzglas gebildet und das Kernmaterial 12 soll aus Silizium bestehen. Die Art der Herstellung des Lichtleiters erfolgt analog zum ersten Ausführungsbeispiel, wobei in diesem Fall T_1 oberhalb 1420°C zu wählen ist.

[0014] Wie weit in jedem Fall die Temperatur T_1 oberhalb der Schmelztemperatur des Kernmaterials gewählt werden kann, ist vornehmlich abhängig davon, welche Viskosität das Kapillarenmaterial in diesem Temperaturbereich annimmt.

[0015] Die Materialauswahl für die im Ausführungsbeispiel verwendeten Kapillaren 1 ist für den bevorzugten Verwendungszweck besonders vorteilhaft, beschränkt die Erfindung jedoch nicht einzig darauf. Durch die vorgeschlagenen Materialien für die zum Einsatz gelangenden Kapillaren und die Dimensionierung des Kapillarenmantels 11 in bezug auf den Kapillareninnendurchmesser d_2 ist eine Leitung von sichtbarem Licht im Mantel 11 der Lichtleitfaser gewährleistet, was für das bevorzugte Verwendungsgebiet zu Justierzwecken von erheblichem Vorteil ist, wohingegen im Kern 12 des Lichtleiters infrarotes Licht geleitet wird, dessen Wellenlänge im Falle der Verwendung von Silizium zwi-

schen 2 µm–5 µm und im Falle von Germanium zwischen 3 µm–13 µm liegt.

[0016] Die mechanische Festigkeit der erhaltenen Lichtleiter ist so groß, daß mit einer Faser mit einem Kerndurchmesser von bspw. 50 µm ein Krümmungsradius von 1 cm durchaus möglich ist. Silizium und Germanium sind chemisch beständig, nicht wasserlöslich und lichtunempfindlich.

[0017] Durch die Erfindung werden Lichtleiter erhalten, die die Nachteile der bekannten IR-Fasern nicht aufweisen.

[0018] Auch liegt es im Rahmen der Erfindung, für den Fall, daß der Kapillarenmantel 11 bei speziellen anderweitigen Verwendungen der Lichtleitfaser nicht erforderlich ist, diesen bspw. durch einen Ätzschritt zu entfernen. Ebenso liegt es im Rahmen der Erfindung, wenn für bestimmte Verwendungen des Lichtleiters darauf verzichtet werden kann, daß dieser genannte Krümmungen schadlos standhält, diesen stab- bzw. taperförmig mit einem entsprechend größeren Durchmesser zu fertigen als auch der Kapillare eine vorgebbare Krümmung im noch plastischen Zustand aufzuprägen.

Patentansprüche

1. Lichtleiter zum Leiten von Licht im Infrarotbereich von ≥ 2,5 µm, bestehend aus einem Kern (12) und einem Mantel (11), wobei der Mantel (11) als Kapillare oder als dünnes Rohr (1) ausgebildet ist und aus einem Material besteht, das eine Viskosität zwischen 10^7 bis 10^{13} dPas bei einer Temperatur T_1 aufweist, bei der ein den Kern bildendes Material bereits in Schmelze vorliegt, wobei das Kernmaterial entweder aus Silizium oder aus Germanium besteht.

2. Lichtleiter nach Anspruch 1, dadurch gekennzeichnet, daß dem Mantel (11) der Kapillare eine Wandstärke (d_1) gegeben ist, die bei kleinen Kapillareninnendurchmessern, in der Größenordnung von 10 bis 100 µm, in der Größenordnung des Durchmessers (d_2) des Kerns (12) liegt.

3. Lichtleiter nach Anspruch 1 oder 2, dadurch gekennzeichnet, daß der Mantel (11) aus einem Material gefertigt ist, welches in einem anderen Spektralbereich als der Kern (12) Licht leitet.

4. Lichtleiter nach einem der vorstehenden Ansprüche, dadurch gekennzeichnet, daß der Mantel (11) aus einem Glas besteht, wenn das Kernmaterial durch Germanium gebildet ist.

5. Lichtleiter nach einem der Ansprüche 1 bis 3, dadurch gekennzeichnet, daß der Mantel (11) aus Quarzglas besteht, wenn das Kernmaterial durch Silizium gebildet ist.

6. Lichtleiter nach einem der vorstehenden Ansprüche, dadurch gekennzeichnet, daß die Wandstärke (d_1) des Mantels (11) und der Durchmesser (d_2) des Kerns (12) im Bereich von 10 µm bis 1 mm festgelegt sind.

7. Lichtleiter nach einem der vorstehenden Ansprüche, dadurch gekennzeichnet, daß die Wandstärke (d_1) des Mantels (11) und der Durchmesser (d_2) des Kerns (12) im Bereich von 10 µm bis 200 µm festgelegt sind.

8. Verfahren zur Herstellung eines Lichtleiters zum Leiten von Licht im Infrarotbereich von ≥ 2,5 µm, bei dem

ein den IR-lichtleitenden Kern (12) bildendes Material (3) in eine Schmelze überführt wird,

eine Kapillare oder ein dünnes Rohr (1), bestehend aus einem Glas oder Quarz ausgewählt wird, welches bei einer Temperatur T1, die geringfügig oberhalb der Schmelztemperatur des Kernmaterials liegt, eine Viskosität zwischen 10^7 bis 10^{13} dPas annimmt,

diese Kapillare oder dieses dünne Rohr (1) auf die genannte Temperatur T1 erwärmt wird und bei Erreichen der Temperatur T1 einseitig in das geschmolzene Material (3) eingetaucht und dieses in die Kapillare oder das Rohr (1) eingesaugt wird und

die Kapillare oder das Rohr (1) bis zur gewünschten Verfüllung auf der Temperatur T1 gehalten und anschließend im verfüllten Zustand einer unmittelbaren Abkühlung unterworfen wird.

9. Verfahren nach Anspruch 8, dadurch gekennzeichnet, daß für das den Kern (12) bildende Material Silizium und für die Kapillare oder das dünne Rohr (1) Quarzglas eingesetzt wird.

10. Verfahren nach Anspruch 8, dadurch gekennzeichnet, daß für das den Kern (12) bildende Material Germanium und für die Kapillare oder das dünne Rohr (1) ein Glas eingesetzt wird.
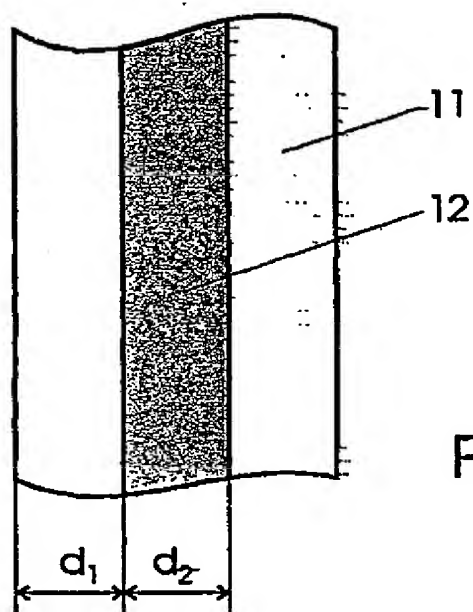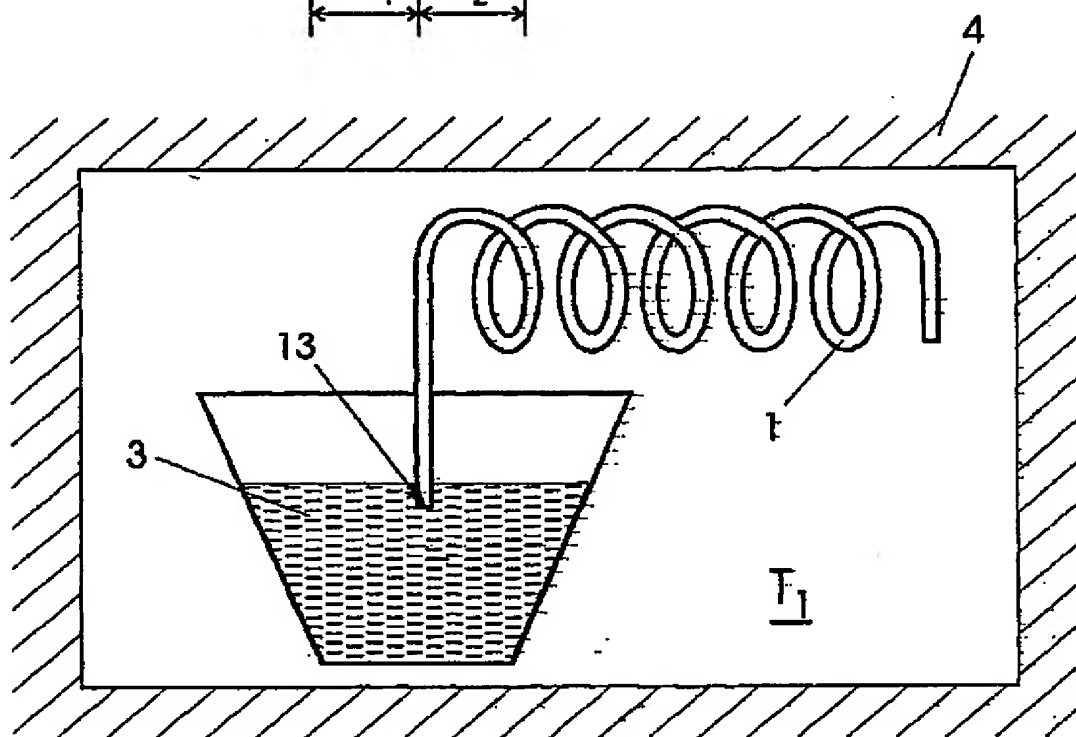
Hierzu 1 Seite(n) Zeichnungen

11
12

d_1 d_2

Fig. 1

4
13
3
1
$\underline{T_1}$

Fig. 2

201 620/151

Optical gain in silicon nanocrystals

L. Pavesi*, L. Dal Negro*, C. Mazzoleni*, G. Franzò† & F. Priolo†

* INFM & Dipartimento di Fisica, Università di Trento, Via Sommarive 14, 38050 Povo, Italy
† INFM & Dipartimento di Fisica e Astronomia, Università di Catania, Corso Italia 57, 95129 Catania, Italy

Adding optical functionality to a silicon microelectronic chip is one of the most challenging problems of materials research. Silicon is an indirect-bandgap semiconductor and so is an inefficient emitter of light. For this reason, integration of optically functional elements with silicon microelectronic circuitry has largely been achieved through the use of direct-bandgap compound semiconductors. For optoelectronic applications, the key device is the light source—a laser. Compound semiconductor lasers exploit low-dimensional electronic systems, such as quantum wells and quantum dots, as the active optical amplifying medium. Here we demonstrate that light amplification is possible using silicon itself, in the form of quantum dots dispersed in a silicon dioxide matrix. Net optical gain is seen in both waveguide and transmission configurations, with the material gain being of the same order as that of direct-bandgap quantum dots. We explain the observations using a model based on population inversion of radiative states associated with the Si/SiO₂ interface. These findings open a route to the fabrication of a silicon laser.

Silicon, the mainstay semiconductor in microelectronic circuitry, has been considered unsuitable for optoelectronic applications owing to its indirect electronic bandgap, which limits its efficiency as a light emitter. Recently, room-temperature light emission from silicon has been shown to be possible when the silicon is in the form of a low-dimensional system[1-5] or when selected active impurities (such as erbium[6]) and/or new phases (such as iron disilicide[7]) are inserted into the silicon lattice. All manner of low-dimensional silicon systems—such as porous silicon[1,2,5], silicon nanocrystals[3], silicon/insulator superlattices[4], silicon nano-pillars[8]—are being actively investigated as a means of improving the light-emission properties of silicon. The physical mechanism underlying high external quantum efficiencies for photoluminescence in low-dimensional silicon is mainly that of the quantum confinement of excitons in a nanometre-scale crystalline structure[9], although the silicon/dielectric interface is also thought to play an active role in both the passivation of non-radiative states and the formation of radiative states[10]. Such work has led to many claims of a future role for silicon in photonic applications[9,11-13], yet a silicon laser has remained unlikely[14].

To produce a silicon-based laser, we should demonstrate its light amplification or stimulated emission[15]. But light amplification in silicon is difficult because (1) it has efficient free carrier absorption, which reduces the net gain available for laser action[14]; (2) there is

significant Auger saturation of the luminescence intensity at high power[9]; and (3) there is significant size-dependence of the radiative energies in Si nanostructures, which yields large inhomogeneous broadening and significant optical losses in the system[16]. Here we report measurements of stimulated emission and light amplification in Si nanostructures and demonstrate optical gain in a single pass configuration. Population inversion is realized between the fundamental and a radiative state associated with the nanocrystal–oxide interface[10]. These findings could lead the way to a silicon-based laser.

Silicon nanocrystals

Low-dimensional silicon nanocrystals have been produced by negative ion implantation (80 keV; 1×10^{17} Si ions cm^{-2}) into ultra-pure quartz substrates or into thermally grown silicon dioxide layers on Si substrates, followed by high-temperature thermal annealing (1,100 °C for 1 h). Quartz wafers (hereafter referred to

Figure 2 Amplified spontaneous emission intensity (ASE, disks) versus excitation stripe length (l) of Si nanocrystals embedded in a quartz matrix. Recording wavelength, 800 nm. A fit to the data with equation (1) is shown as the dashed line. The inset shows the experimental method. A cylindrical lens was used to focus the laser beam on the sample surface on a stripe 10-µm wide and of variable length. Only the central part of the laterally unfocused laser spot was used to excite the sample. Measurements show that within these experimental conditions the laser power density on the sample surface is constant and independent of l. An optical 40 × objective imaged the sample edge on a 40-µm pinhole so that only the light coming from the near sample surface region was collected. The use of a pulsed laser avoided any thermal heating of the sample. The excitation conditions were 1 kW cm^{-2} mean power at a wavelength of 390 nm.
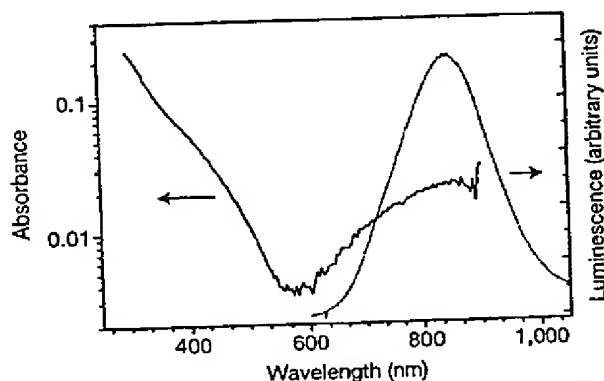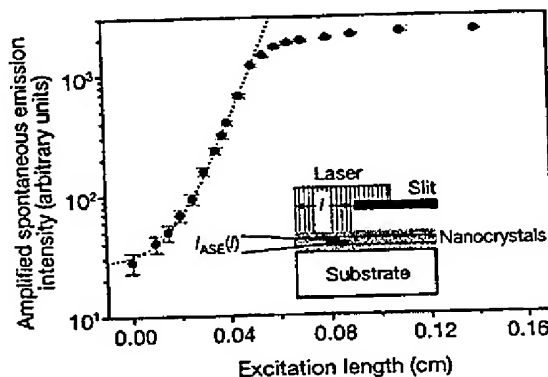

Figure 1 Room temperature absorbance and luminescence of Si nanocrystals embedded in a quartz matrix. The experimental set-up limited the absorbance measurement range. The absorbance of the quartz wafer was subtracted from the measured spectra. The 488 nm line of an Ar laser excited the luminescence.

as 'sample A') were used for optical transmission experiments, and silicon wafers (hereafter referred to as 'sample B') to demonstrate microelectronics compatibility. Transmission electron microscopy of these samples showed silicon nanocrystals embedded within the oxide matrix. They were formed in a region centred at a depth of 110 nm from the sample surface and extending for a thickness of 100 nm; they were ~3 nm in diameter, with a concentration of 2×10^{19} cm^{-3}. If we consider the Maxwell–Garnett approximation, we can estimate an effective refractive index of 1.89 for the nanocrystal region (see Fig. 3 in the Supplementary Information). For nanocrystals produced by plasma-enhanced chemical vapour deposition (PE-CVD)[17], an effective refractive index of 1.71 was measured by ellipsometry. We note that in sample A, this causes the formation of a planar waveguide with an optical filling factor of about 9.7% when a refractive index of 1.89 is considered, or of 1.17% when a refractive index of 1.71 is assumed (see Fig. 3 in the Supplementary Information).

Absorbance and luminescence spectra at room temperature for sample A are shown in Fig. 1. A single wide emission band peaked at 800 nm, characteristic of the radiative recombination of carriers in Si nanocrystals, is observed. Absorbance measurements revealed a band in the near-infrared and a rising absorption edge at shorter wavelengths. The rising edge is due to absorption in the quantum confined states of the nanocrystals[18], whereas the peculiar feature of the near-infrared absorption band is caused by a Si=O interface state[10,19,20]. As predicted by theory[10,21] and inferred from experiment, the interface state is formed at the interface between the Si nanocrystals and the SiO$_2$ matrix. The microscopic nature of these interface states is still under debate[10,21]. Very good quality SiO$_2$ and Si nanocrystals are needed to observe this interface state, which in other Si-based systems is hindered by interfaces with defects or the low quality of the oxide. We note the spectral coincidence of the emission band and the interface state absorption band, suggesting that radiative emission in Si nanocrystals occurs through a radiative state associated with the nanocrystal–oxide interface. Time-resolved luminescence, under picosecond excitation, on our nanocrystals showed a very fast rise time, within our experimental sensitivity (some nanoseconds)[22]. The decay time of the luminescence was in the microsecond range; it is dependent on the emission energy[23].

Light amplification

To measure light amplification we used the variable strip length method (see the inset of Fig. 2)[24]. The sample is optically excited by a doubled Ti:sapphire laser beam ($\lambda = 390$ nm, 2-ps pulse width, 82-MHz repetition rate) in a stripe-like geometry with variable length (l). The amplified spontaneous emission intensity I_{ASE} that is emitted from the sample edge (observation angle $\phi = 0$) is measured as a function of l. From a fit of the resulting curve, the optical gain g can be deduced at every wavelength. By assuming a one-dimensional amplifier model, I_{ASE} can be related to g by[15,24]

$$I_{ASE}(l) \propto \frac{I_{SPONT} \times l}{g - \alpha} \left(e^{(g-\alpha)l} - 1 \right) \tag{1}$$

where I_{SPONT} is the spontaneous emission intensity per unit length and α an overall loss coefficient. The gain measured in this way is the modal gain[15]. Figure 2 shows I_{ASE} versus l in Si nanocrystals measured at a wavelength of 800 nm. For small values of l (<0.05 cm), an exponential increase of I_{ASE} is observed that indicates the occurrence of amplified spontaneous emission. A fit with equation (1) yields the net modal gain $g - \alpha = 100 \pm 10$ cm^{-1}. For large values of l (>0.05 cm), I_{ASE} saturates as expected for any finite power supply amplification mechanism. At
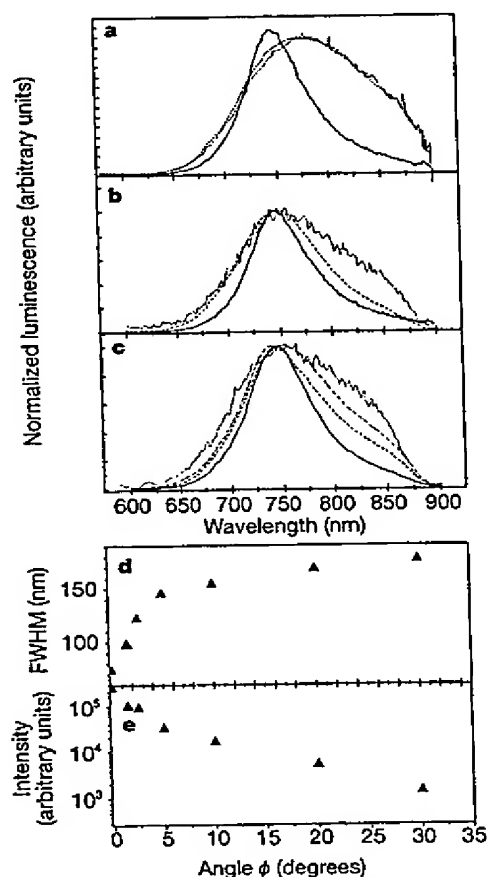
Figure 4 Amplified spontaneous emission spectra of sample A for different measurement conditions. **a**, Amplified spontaneous emission (ASE) spectra for a constant excitation length $l = 2,000$ μm and various power densities P: continuous line 2.3 kW cm^{-2}, dashed line 1 kW cm^{-2}, dotted line 170 W cm^{-2}. **b**, ASE spectra for constant $P = 2.3$ kW cm^{-2} and various l values: $l = 2,000$ μm continuous line, $l = 650$ μm dashed line, $l = 200$ μm dotted line. **c**, ASE spectra for constant $P = 1$ kW cm^{-2} and $l = 3,000$ μm and various observation angles ϕ. ϕ is defined with respect to the optical axis of the one-dimensional amplifier. Continuous line $\phi = 0°$, dashed line $\phi = 1.5°$, dash-dotted line $\phi = 2.5°$, dotted line $\phi = 20°$. The low energy cut-off of the photomultiplier used to record the data deforms the spectra for wavelength longer than 880 nm. **d**, Full-width at half-maximum (FWHM) of the ASE emission as a function of the observation angle ϕ. **e**, Peak intensity of the ASE signal as a function of ϕ.
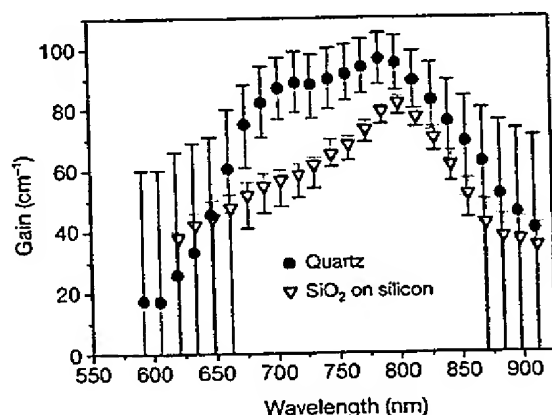

Figure 3 Spectral dependence of the net modal gain. Sample A, circles; sample B, triangles. The experimental conditions were as in Fig. 2. The large error bars result from both the low signal-to-noise ratio of the streak camera detection for low intensity signals and from the numerical procedure used for obtaining the modal gain from the ASE data[30,31].

low power density, we measured absorption; when the pump power was increased, the peak net modal gain increased and then saturated at values of about 100 cm^{-1} for power densities of about 5 kW cm^{-2}.

By measuring the amplified signal for various wavelengths we obtained the gain spectrum for both samples A and B (Fig. 3; see also Supplementary Information). A wide spectral band is observed which spectrally overlaps the wavelength range of the luminescence, demonstrating that amplification is produced by the radiative state associated with the nanocrystal–oxide interface. We noticed that both samples yielded similar shapes and values for the gain curve. A confirmation of these findings was the observation of a strong emission lineshape narrowing (Fig. 4), either when the pump power density P is increased with fixed excitation length l (Fig. 4a), or when the excitation length l is increased with a fixed P (Fig. 4b). When l and P are fixed and the observation angle ϕ is changed (Fig. 4c–e), a significant intensity decrease and a broadening of the amplified emission spectrum occur as soon as there is deviation from the strict one-dimensional amplifier configuration, that is, when $\phi > 0°$. These observations support also the waveguide formation in our samples.

The most direct evidence of light amplification from our systems was provided by pump and probe transmission measurements. An intense laser beam (pump) at 390 nm excites the sample in order to reach the population inversion needed for amplification, while a weak probe signal at ~800 nm passes through the active layer of thickness d. In the presence (absence) of the pump beam the probe beam is amplified (absorbed). In Fig. 5 we show the results. The probe signal is clearly amplified when passing through the excited nanocrystals. To our knowledge, this is the first evidence of light amplification in transmission, usually named single-pass gain, in Si-based systems. We deduced the net material gain values by using the formula given in Fig. 5; they are high enough to compare with those of self-assembled quantum dots made of III–V semiconductors[25,26]: 10,000 ± 3,000 cm^{-1}. This value has a very large error bar because of the geometry of the active nanocrystal layer and the losses in the quartz substrate. No change in probe intensity in the presence/absence of the pump beam was observed when the probe beam passed through pure quartz (without nanocrystals). Moreover, by decreasing the pump intensity (Fig. 5, right panel) we measured even absorption of the probe beam (population inversion is no

longer reached in nanocrystals). By changing the probe wavelength the net material gain decreased and eventually disappeared (amplification is lost when the probe energy is no longer in resonance with the transition for which population inversion is achieved) with an overall spectral dependence similar to that shown in Fig. 3 (see also Supplementary Information).

Gain cross-section per nanocrystal

By using the formalism of ref. 27 and the measured probe beam transmission under inversion conditions, we estimated a maximum-gain cross-section per nanocrystal $\gamma_T \approx 5 \times 10^{-16}$ cm^2. It is interesting to compare this gain cross-section per nanocrystal with the photon absorption cross-section per nanocrystal (σ). We have hence directly measured the absorption cross-sections of ion-implanted Si nanocrystals by studying the rise time of the photoluminescence intensity as a function of pump power in a fashion similar to that recently reported for porous Si[28].

The photoluminescence intensity is given by $1 \propto N^*/\tau_R$, where N^* is the concentration of excited nanocrystals and τ_R the radiative lifetime. The rate equation for nanocrystal excitation will be:

$$\frac{dN^*}{dt} = \sigma J(N - N^*) - \frac{N^*}{\tau} \quad (2)$$

where J is the photon flux, N is the concentration of nanocrystals and τ is the decay time, taking into account both radiative and non-radiative processes. If a continuous wave (CW) pumping laser is turned on at $t = 0$, N^* will change according to equation (2) and the photoluminescence intensity will increase according to the following law:

$$I(t) = I_0\left\{1 - \exp\left[-\left(\sigma J + \frac{1}{\tau}\right)t\right]\right\} = I_0\left\{1 - \exp\left[-\left(\frac{t}{\tau_{on}}\right)\right]\right\} \quad (3)$$

A measure of the photoluminescence rise time as a function of J will therefore give direct information on the absorption cross-section. The inset to Fig. 6 shows $I(t)$ at 850 nm for Si nanocrystals pumped at 488 nm for different pump powers P. As predicted by equation (3), the photoluminescence rise time becomes shorter and shorter
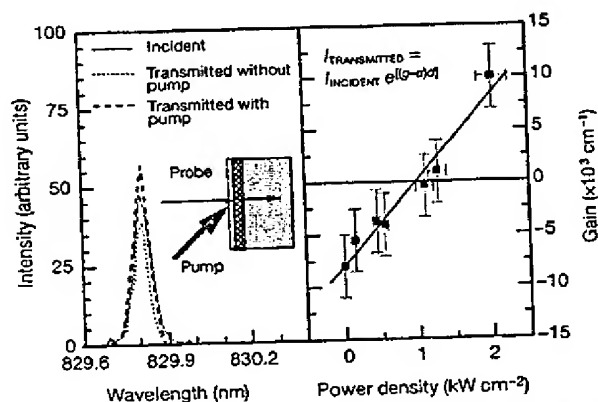

Figure 5 Gain measurements. Left panel, spectrum of the transmitted probe beam measured in presence (dashed line) or in absence (dotted line) of the pump beam. The spectrum of the transmitted probe beam in absence of the absorbing\amplifying nanocrystal medium is also reported (continuous line) and named the incident beam. The inset shows the principle of the experiment. The formula used to deduce the material gain is also reported, d being the thickness of the active region. The probe beam was provided by a Kr lamp, which was imaged to a spot size of about 0.01 mm^2 on the sample surface. The pump beam had a mean power of about 2 kW cm^{-2} and a wavelength of 390 nm. Right panel, dependence of the material gain value on the pump power density.
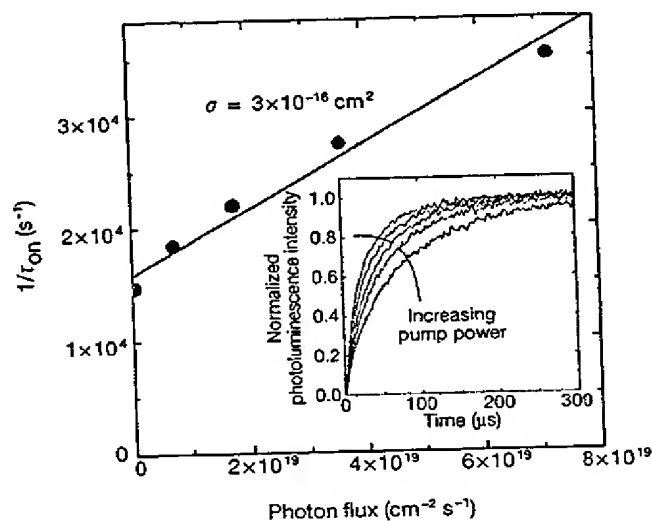

Figure 6 Reciprocal of the rise time τ_{on} as a function of the pump laser photon flux as obtained from a fit to the time resolved photoluminescence data shown in the inset. The slope gives the photon absorption cross-section σ. Inset: time resolved photoluminescence intensity at 850 nm switching on the 488 nm line of a CW Ar pumping laser at $t = 0$; data are taken at room temperature, at different pump powers (in the 0.8–80 mW range) and are normalized to the maximum intensity.

as P is increased. By fitting these curves with equation (3) we obtain the values of the rise time, τ_{on}, at the different P values. The reciprocal of τ_{on} is reported in Fig. 6 as a function of J. The data follow a straight line with a slope $\sigma \approx 3 \times 10^{-16}$ cm^2. The intercept of the fitted straight line with the vertical axis gives the lifetime of the Si nanocrystals in the system at the measured wavelength. The obtained value (70 μs) is in agreement with decay time measurements at 850 nm on the same sample. In this way we have been able to obtain a direct measurement of the photon absorption cross-section of the nanocrystals. Although this measurement is performed at an excitation wavelength of 488 nm, it should reflect the property of the 800 nm state because absorbance at these two wavelengths is identical (see Fig. 1). We note that, as theoretically predicted[15], the measured absorption cross-section σ is of the same order of magnitude as the gain cross-section γ_T. The same agreement is found when we compare the net material gain to the absorption coefficient deduced by the absorbance data of Fig. 1.

Another important issue concerns the comparison of the gain cross-sections that are derived from the modal and the material gain. It was shown in ref. 27 that in the variable stripe-length geometry, the gain cross-section per nanocrystal (γ_{ASE}) can be derived by using

$$\gamma_{ASE} = \frac{g}{(f_c - f_v)N\Gamma} \qquad (4)$$

where Γ is the optical filling factor of the amplified mode. By assuming a complete population inversion $f_c - f_v = 1$, an optical filling factor of 0.097 and the measured net modal gain $g \approx 100$ cm^{-1}, one finds $\gamma_{ASE} \approx 5 \times 10^{-17}$ cm^2. This is a lower limit to γ_{ASE}. If we consider an incomplete inversion or a weaker confining waveguide (that is, no step index profile in the waveguide and/or a lower effective refractive index for the nanocrystal), γ_{ASE} will significantly increase. For example, by using the Γ value computed for the refractive index measured in PE-CVD nanocrystals[17], we obtain $\gamma_{ASE} \approx 3 \times 10^{-16}$ cm^2. The difference between the two estimated values of γ_{ASE} may be an indication of the quantitative uncertainty on the gain cross-section values determined by the gain measurements.

A comparison of the gain cross-sections per nanocrystal derived by transmission (γ_T) and by the variable strip length method (γ_{ASE}) shows that the two values are in reasonable quantitative agreement. Indeed, the determined value of γ_{ASE} is only a lower limit and there are large error bars on the pump and probe determined gain coefficients.

Origin of gain

The wide spectral gain of inhomogeneous nature is energetically matching both the luminescence emission and the 800-nm interface state absorption band. For these reasons, a three-level model is proposed to explain the observed gain (Fig. 7): two levels correspond to the lowest unoccupied molecular orbital (LUMO), or the bottom of the conduction band, and to the highest occupied molecular orbital (HOMO), or the top of the valence band of the nanocrystal, respectively. The third level is due to the radiative interface state observed in absorption and responsible for the luminescence emission band at 800 nm. Optical excitation populates the LUMO, emptying the HOMO. Electrons from the LUMO relax very rapidly to the interface state. Electrons in the interface state have long lifetimes. Indeed, the absorption band at 800 nm, the Stokes shift between absorption and luminescence, the fast rise and the slow decay times of the 800-nm luminescence under picosecond excitation, and the efficient luminescence emission of the 800-nm luminescence all support this energy model. Within the model, the rate of depopulation of the initial state is much faster than its filling rate via a carrier recombination mediated by the interface state. Population inversion between the HOMO and the radiative state associated with the nanocrystal–oxide interface is thus possible. This model also explains why losses due to free carrier absorption that usually exceed the gain by stimulated emission in other Si based systems[29], or those due to Auger recombinations[22], are not effective here. In addition, model calculations[10] show that the size dependence of the radiative interface state energy is smaller than that of conduction-to-valence band transitions, relaxing issues related to the broad distribution of sizes.

Using the measured absorption cross-section σ per nanocrystal, we estimate that under our peak excitation condition of about 10^{22} photons cm^{-2} s^{-1}, more than 100 electron–hole pairs per nanocrystal are generated. As we have nanocrystals with about 500 Si atoms, of which about 35% are surface atoms, we have about 150 interface states available per Si nanocrystal when we assume that each surface Si atom is bound to an O atom. In Fig. 5, we show that to have optical gain the excitation level should be high enough to invert most of these states.

In Table 1 we report a compilation of data on the gain cross-section per quantum dot for some III–V semiconductors. It can be noticed that the silicon nanocrystal values are about three orders of magnitude lower than the one typically found in InAs quantum dots. We argue that this is due to the indirect bandgap of Si and to the fact that the gain is due to radiative interface states. Despite this difference, the net material gain is of the same order of magnitude between Si nanocrystals and InAs quantum dot systems, owing to the much higher areal density of nanocrystals that is achievable with the ion-implantation method used in this work. We note that the gain cross-section per nanocrystal γ is inversely proportional to the radiative lifetime τ_R (ref. 15). By looking at the γ data in Table 1, we infer large differences in lifetimes. Indeed radiative lifetimes in the microsecond range are measured for Si nanocrystals, whereas for InAs quantum dot lifetimes in the nanosecond range were reported[25,26].
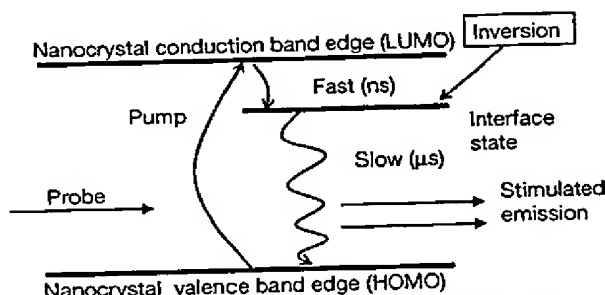

Figure 7 Schematic energy diagram for a nanocrystal showing how population inversion can be reached in this system.

Table 1 Gain cross-section per quantum dot or nanocrystal

Quantum dot material	Net model gain (cm^{-1})	Net material gain ($\times 10^4$ cm^{-1})	Areal dot density (cm^{-2})	Active layer thickness (nm)	Filling factor (10^{-4})	Gain cross-section per dot (10^{-16} cm^2)	Reference
InAs single layer quantum dot	8.2	9*	1×10^{11}	1.7	1.2	1,200	25
InAs 7 stacks quantum dot	70–85	1.5*	1×10^{11}	100	48	4,000	26
GaAs single layer quantum dot	13*		1×10^{10}			450*	27
Si nanocrystals	100	1	2×10^{14}	100	970	0.5–5	This work

*Calculated approximately.

articles

Conclusions

Modal and net material optical gains have been observed unambiguously in Si nanocrystals. Quantitative estimates of gain cross-section per nanocrystal show that the measured values are orders of magnitude lower than those found in III–V semiconductor quantum dots. However, owing to the much higher stacking density of Si nanocrystals with respect to direct-bandgap quantum dots, similar values for the material gain are observed. These findings open a route towards the realization of a silicon-based laser. □

1. Canham, L. T. Silicon quantum wire array fabrication by electrochemical and chemical dissolution of wafers. *Appl. Phys. Lett.* 57, 1045–1048 (1990).
2. Cullis, A. G. & Canham, L. T. Visible light emission due to quantum size effects in highly porous crystalline silicon. *Nature* 353, 335–338 (1991).
3. Wilson, W. L., Szajowski, P. F. & Brus, L. E. Quantum confinement in size-selected surface-oxidised silicon nanocrystals. *Science* 262, 1242–1244 (1993).
4. Lu, Z. H., Lockwood, D. J. & Baribeau, J.-M. Quantum confinement and light emission in SiO₂/Si superlattices. *Nature* 378, 258–260 (1995).
5. Hirschman, K. D., Tsybeskov, L., Duttagupta, S. P. & Fauchet, P. M. Silicon-based light emitting devices integrated into microelectronic circuits. *Nature* 384, 338–340 (1996).
6. Franzò, G., Priolo, F., Coffa, S., Polman, A. & Carnera, A. Room temperature electroluminescence from Er doped crystalline silicon. *Appl. Phys. Lett.* 64, 2235–2237 (1994).
7. Leong, D., Harry, M., Reeson, K. J. & Homewood, K. P. A silicon/iron disilicide light-emitting diode operating at a wavelength of 1.5 µm. *Nature* 387, 686–688 (1997).
8. Nassiopoulos, A. G., Grigoropoulos, S. & Papadimitriou, D. Electroluminescent device based on silicon nanopillars. *Appl. Phys. Lett.* 69, 2267–2269 (1996).
9. Bisi, O., Ossicini, S. & Pavesi, L. Porous silicon: a quantum sponge structure for silicon based optoelectronics. *Surf. Sci. Rep.* 38, 1–126 (2000).
10. Wolkin, M. V., Jorne, J., Fauchet, P. M., Allan, G. & Delerue, C. Electronic states and luminescence in porous silicon quantum dots: the role of oxygen. *Phys. Rev. Lett.* 82, 197–200 (1999).
11. Miller, D. A. Silicon sees the light. *Nature* 378, 238 (1995).
12. Iyer, S. S. & Xie, Y.-H. Light emission from silicon. *Science* 260, 40–46 (1993).
13. Silicon based optoelectronics. *Mater. Res. Bull.* 23(4), (1998).
14. Fauchet, P. M. The integration of nanoscale porous silicon light emitters: materials science, properties and integration with electronic circuitry. *J. Lumin.* 80, 53–64 (1999).
15. Yariv, A. *Quantum Electronics* 2nd edn (Wiley & Sons, New York, 1974).
16. Canham, L. T. in *Frontiers of Nano-Optoelectronic Systems* (eds Pavesi, L. & Buzaneva, E.) 85–98 (Kluwer Academic, Dordrecht, 2000).
17. Iacona, F., Franzò, G. & Spinella, C. Correlation between luminescence and structural properties of Si nanocrystals. *J. Appl. Phys.* 87, 1295–1303 (2000).
18. Kovalev, D., Heckler, H., Polisski, G. & Koch, F. Optical properties of Si nanocrystals. *Phys. Status Solidi* 251, 871–930 (1999).
19. Kanemitsu, Y. & Okamoto, S. Quantum confinement and interface effects on photoluminescence from silicon single quantum wells. *Solid State Commun.* 103, 573–576 (1997).
20. Kanemitsu, Y. & Okamoto, S. Phonon structures and Stokes shift in resonantly excited luminescence of silicon nanocrystals. *Phys. Rev. B* 58, 9652–9655 (1998).
21. Degoli, E. & Ossicini, S. Quantum confined and interface states related visible luminescence in Si/SiO₂ superlattices. *Surf. Sci.* (in the press).
22. Klimov, V. I., Schwarz, Ch., McBranch, D. W. & White, C. W. Initial carrier relaxation dynamics in ion-implanted Si nanocrystals: femtosecond transient absorption study. *Appl. Phys. Lett.* 73, 2603–2605 (1998).
23. Linnros, J., Galeckas, A., Lalic, N. & Grivickas, V. Time-resolved photoluminescence characterisation of nm-sized silicon nanocrystallites in SiO₂. *Thin Solid Films* 297, 167–170 (1997).
24. Shaklee, K. L., Nahaory, R. E. & Leheny, R. F. Optical gain in semiconductors. *J. Lumin.* 7, 284–309 (1973).
25. Kirstaedter, N. *et al.* Gain and differential gain of single layer InAs/GaAs quantum dot injection lasers. *Appl. Phys. Lett.* 69, 1226–1228 (1996).
26. Lingk, C. *et al.* Dynamics of amplified spontaneous emission in InAs/GaAs quantum dots. *Appl. Phys. Lett.* 76, 3507–3509 (2000).
27. Blood, P. On the dimensionality of optical absorption, gain and recombination in quantum-confined structures. *IEEE J. Quantum Electron.* 36, 354–362 (2000).
28. Kovalev, D. *et al.* Optical absorption cross sections of Si nanocrystals. *Phys. Rev. B* 61, 4485–4487 (2000).
29. von Behren, J., Kostoulas, Y., Ucer, K. B. & Fauchet, P. M. The femtosecond optical response of porous, amorphous and crystalline silicon. *J. Non-Cryst. Solids* 198–200, 957–960 (1996).
30. Jordan, V. Gain measurements of semiconductor laser diodes: requirements for wavelength resolution and sensitivity to noise. *IEE Proc. Optoelectron.* 141, 13–15 (1994).
31. Hvam, J. M. Direct recording of optical gain spectra from ZnO. *J. Appl. Phys.* 49, 3124–3126 (1978).

TOPICAL REVIEW

Will silicon be the photonic material of the third millenium?*

L Pavesi

INFM and Dipartimento di Fisica, Universita' di Trento, Via Sommarive 14, 38050-Povo Trento, Italy

E-mail: pavesi@science.unitn.it

Abstract

Silicon microphotonics, a technology which merges photonics and silicon microelectronic components, is rapidly evolving. Many different fields of application are emerging: transceiver modules for optical communication systems, optical bus systems for ULSI circuits, I/O stages for SOC, displays, ... In this review I will give a brief motivation for silicon microphotonics and try to give the state-of-the-art of this technology. The ingredient still lacking is the silicon laser: a review of the various approaches will be presented. Finally, I will try to draw some conclusions where silicon is predicted to be the material to achieve a full integration of electronic and optical devices.

(Some figures in this article are in colour only in the electronic version)

Contents

R1169

1. Why silicon photonics?

The big success of today's microelectronic industry is based on various factors, among others

- the presence of a single material, silicon, which is widely available, can be purified to an unprecedented level, is easy to handle and to manufacture and shows very good thermal and mechanical properties which render the processing of devices based on it easy [1],
- the availability of a natural oxide of silicon, SiO_2, which effectively passivates the surface of silicon, is an excellent insulator, is an effective diffusion barrier and has a very high etching selectivity with respect to Si,
- the presence of a single dominating processing technology, CMOS, which accounts for more than 95% of the whole market of semiconductor chips [2],
- the possibility to integrate more and more devices, 55 000 000 transistors in PENTIUM® 4 (figure 1), on larger and larger wafers (300 mm process and 400 mm research) with a single transistor size which is decreasing (gate lengths of 180 nm are in production while 15 nm have been demonstrated) [3], yielding a significant reduction in cost per bit,
- the ability of the silicon industry to face improvements when the technology is hitting the so-called red brick wall, e.g. the use of SiGe for high frequency operation and the introduction of low k-materials and of Cu to reduce RC delays,
- an accepted common roadmap which is dictating the technology evolution for processes, architectures or equipment [3] and
- the presence of big companies which define standards and trends (almost 90% of the market is shared by ten companies).

All these factors have rendered the microelectronics industry very successful. However, in recent years some concerns about the evolution of this industry have been raised which seem related to fundamental materials and processing aspects [4]. An important example is related to the limitations of the operating speed of microelectronic devices due to the interconnect [5]. Figure 2 shows the signal delay as a function of the generation of transistors [6]. For gate length shorter than 200 nm, a situation is reached where the delay is no longer dictated by the gate switching time but by the wiring delay. In addition, as the integration is progressing the length of the interconnects on a single chip is getting longer and longer. Nowadays chips have total interconnection length per unit area of the chip of some 5 km cm^{-2} with a chip area of 450 mm^2 while in ten years from now these lengths will become 20 km cm^{-2} for a chip area of 800 mm^2. The problem is not only related to the length of the interconnects but also to the complexity of their architecture. Nowadays, there are six layers of metal levels (figure 3), while in ten years from now there will be more than 12. All these facts introduce problems related to the delay in signal propagation causing RC coupling, signal latency, signal cross-talk and RL delays due to the reduction in dimension and increase in density of the metal line. A possible solution to these problems is looked for in optics [7]: the use of optical interconnects. Nowadays, optical interconnects through optical fibres and III–V laser sources are already used to connect different computers. It is predicted that optical interconnects will be used to connect computer boards in five years, while the use of optical interconnects within the chip is being investigated and will possibly be realized in 10–15 years from now [8]. Optical interconnects are one of the main motivations to look for silicon photonics. But this is not the only one. Photonics has seen a big development in recent years at the request of the communication market, where more and
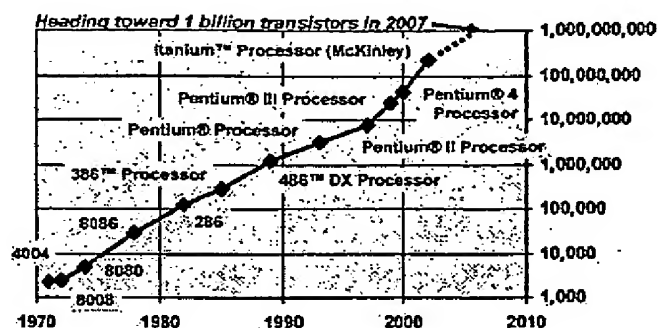
Figure 1. Evolution of the number of transistors in a single CPU (central processing unit) versus the year. This graph is based on the Intel CPU [6].
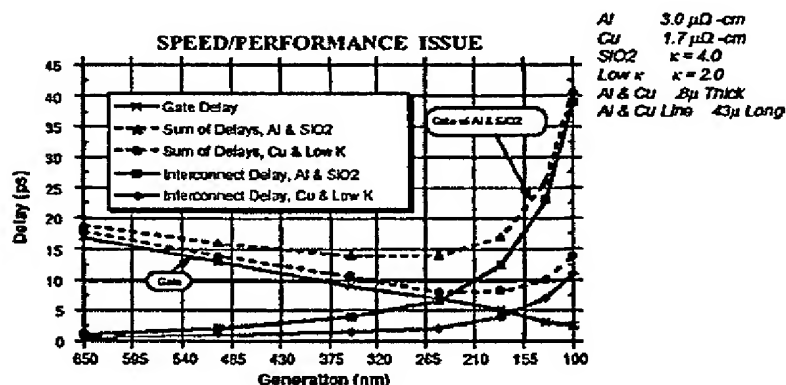

Figure 2. Calculated gate delay and wire delay as a function of the minimum feature size (device generation). From SIA Roadmap 1997 [3]. Interconnections and signal integrity, DAC tutorial. *38th Design Automation Conf.* ©2001 (www.amanogawa.com/epep2000/files/jose1.pdf).

more information has to be sent at higher and higher speed. Nowadays, the capacity of optical communication on long hauls is reaching some Tb/s^{-1} over thousands of kilometres. And all these are thanks to the progress in optical fibre fabrication, the use of DWDM, of EDFA and Raman amplifiers, modulators and single frequency lasers.

If one compares the photonic industry with microelectronics today one can see many differences.

(1) A variety of different materials is used: InP as substrate for source development, silica as material for fibres, lithium niobate for modulators, other materials for DWDM and EDFA and so on.

(2) No single material or single technology is leading the market. Some convergence is appearing towards the use of InP as the substrate material to integrate different optical functions.

(3) The industry is characterized by many different small companies which are specialized in specific devices: lasers, modulators etc. No big companies are dominating at present.

(4) The production technology is still very primitive. Chip scale integration of optical components, which enables low cost and high reproducibility, is not yet achieved. Neither
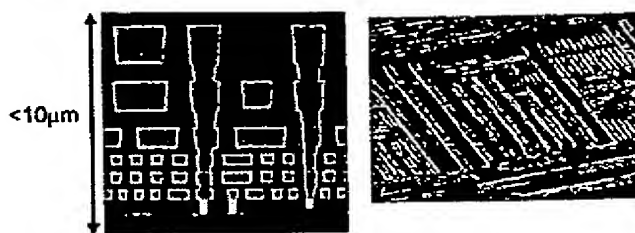
standardization of processes nor packaging of optical components, which is inherent for mass production and repeatability, are present.

(5) Roadmaps to dictate and forecast the evolution of photonics are only now being elaborated [9].

It is commonly accepted that the industrial model of microelectronics if applied to photonics will be a booster to the development and implementation of photonics. To describe this new technology the term of microphotonics has been proposed [11]. All the big players of microlectronics have aggressive programmes to develop microphotonics, mostly based on silicon [10].

The aim of this review is to try to give the state-of-the-art on the development of silicon photonics with the aim of settling the status and trying to weigh up whether silicon can be used as *the* photonics material. For this reason, all the different components are briefly reviewed (section 2) with a special emphasis on the subject which is at the forefront of today's discussion: the route to a silicon laser (section 3). The selection of the various experimental data is not intended to be exhaustive but simply representative of some of the more successful devices and integration schemes which have been reported. I apologize in advance to all those authors whose work I am not referring to.

2. Silicon photonics

It was predicted in the early 1990s that silicon based optoelectronics would be a reality before the end of the century [12, 13]. Indeed, all the basic components have already been demonstrated [14], except for a silicon laser.

2.1. Silicon based waveguides

The first essential component in silicon microphotonics is the medium through which light propagates: the waveguide. This has to be silicon compatible and should withstand normal microelectronics processing. Critical parameters are the refractive index of the core material, its electro-optical effects, the optical losses and the transparency region. To realize low loss optical waveguides, various approaches have been followed [15]: low dielectric mismatch structures (e.g. doped silica [16], silicon nitride [17] or silicon oxynitride on oxide [18], or differently doped silicon [19]) or high dielectric mismatch structures (e.g. silicon on oxide [11]). Low loss silica waveguides are characterized by large dimensions (see figure 4), typically 50 μm of thickness, due to the low refractive index mismatch ($\Delta n = 0.1–0.75\%$). Silica waveguides
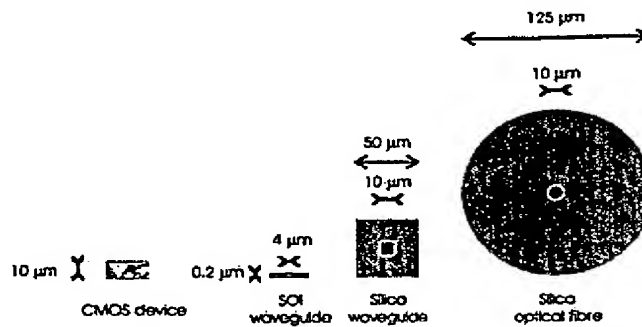
Figure 4. Comparison of the cross-sections of a CMOS chip, a typical SOI waveguide, a typical silica waveguide and a silica mono-mode optical fibre.

have a large mode spatial extent and, thus, are interesting for coupling with optical fibres but not for integration into/within electronic circuits because of a significant difference in sizes. The large waveguide size also prevents the integration of a large number of optical components in a single chip. Similar problems exist for silicon on silicon waveguides where the index difference is obtained by varying the doping density [19]. Silicon on silicon waveguides are very effective for realizing free-carrier injection active devices (e.g. modulators) as well as fast thermo-optic switches thanks to the high thermal conductivity of silicon. A major problem with these waveguides is the large free-carrier absorption which causes optical losses of some dB cm^{-1} for single-mode waveguides at 1.55 μm. Silicon nitride based waveguides [17] and silicon oxynitride waveguides [18] show losses at 633 nm lower than 0.5 dB^{-1} and bending radii of less than 200 μm. The nitride based waveguides are extremely flexible with respect to the wavelength of the signal light: both visible and IR.

At the other extreme, silicon on insulator (SOI) or polysilicon based waveguides allow for a large refractive index mismatch and, hence, for small size waveguides in the sub-micrometre range. This allows a large number of optical components to be integrated within a small area. Optical losses as low as 0.1 dB cm^{-1} at 1.55 μm have been reported for channel waveguides in SOI (optical mode cross-section 0.2 $\times$ 4 μm^2) [20]. Ideal for on-chip transmission, SOI waveguides have coupling problems with silica optical fibre due to both the large size difference and the different optical impedance of the two systems (figure 4). Various techniques have been proposed to solve these problems, among which are adiabatic tapers, V-grooves and grating couplers (figure 5) [21, 22]. Large single-mode stripe loaded waveguides on SOI can be achieved provided that the stripe and the slab are both made of silicon [23]. This SOI system provides low loss waveguides (<0.2 dB cm^{-1}) with single-mode operation with large rib structures (optical mode cross-section 4.5 $\times$ 4 μm^2) and low birefringence (<10^{-3}). Appropriate geometry with the use of an asymmetric waveguide allows bend radii as short as 0.1 mm [24]. A number of photonic components in SOI have been demonstrated [23] and commercialized [24]: directional couplers, dense WDM arrayed waveguide grating, Mach–Zehnder filters, star couplers, ...

2.2. Detectors

The optical signal is converted into an electrical signal by using silicon based photodetectors. Detectors for silicon photonics are based on three different approaches [25]: silicon photoreceivers for λ < 1.1 μm, hybrid systems (mostly III–V on Si) and heterostructure based systems. High speed (up to 8 Gb s^{-1}) monolithically integrated silicon photoreceivers

Adiabatic taper

Waveguide

Waveguide 1

Waveguide 2

Grating coupler

Waveguide   TIR mirror
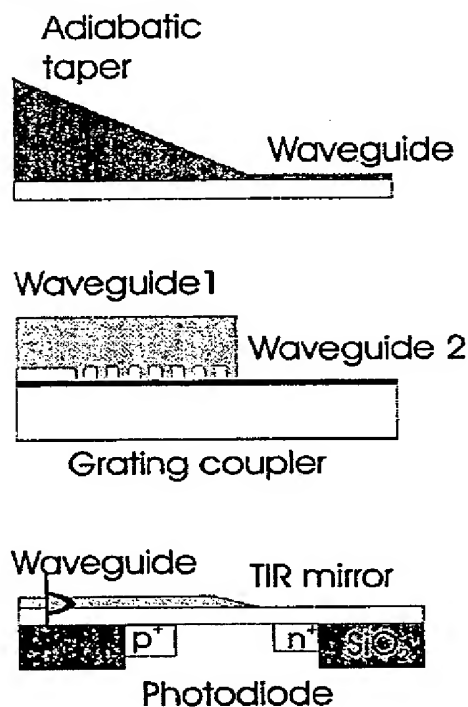
p⁺   n⁺   Si

Photodiode

Figure 5. Various schemes to couple the light from a fibre into a waveguide by using an adiabatic taper or a grating coupler, or from a waveguide into a photodiode by using a curved TIR (total internal reflection) mirror.

at 850 nm have been fabricated by using 130 nm CMOS technology on a SOI wafer [26]. Other recent results confirm the ability of silicon integrated photoreceivers to detect signals with a high responsivity of 0.46 A W^{-1} at 3.3 V for 845 nm light and 2.5 Gb s^{-1} data rate [27]. The heterostructure approach is mainly based on the heterogrowth of Ge rich SiGe alloys: Ge-on-Si photodetectors have been reported with a responsivity of 0.89 A W^{-1} at 1.3 μm and 50 ps response time [28]. 1% quantum efficiency at 1.55 μm in an MSM (metal–semiconductor–metal) detector based on a Si/SiGe superlattice shows that promising developments are possible [29]. Similarly a waveguide photodetector with Ge/Si self-assembled islands shows responsivities of 0.25 mW at 1.55 μm with zero bias [30].

2.3. Other photonics components

Almost all the other photonics components have been demonstrated in silicon microphotonics [13, 25]. Optical modulators, optical routers and optical switching systems have been all integrated into silicon waveguides [31]. Discussion of a series of photonics components realized with SOI waveguides is given in [23] which includes plasma dispersion effect based active gratings, evanescent waveguide coupled silicon–germanium based photodetectors and Bragg cavity resonant photodetectors.

2.4. Silicon photonic integrated circuits

Based on the technologies reported in the previous sections, various demonstrations of photonic integrated circuits based on silicon have been reported. Here we discuss some examples.
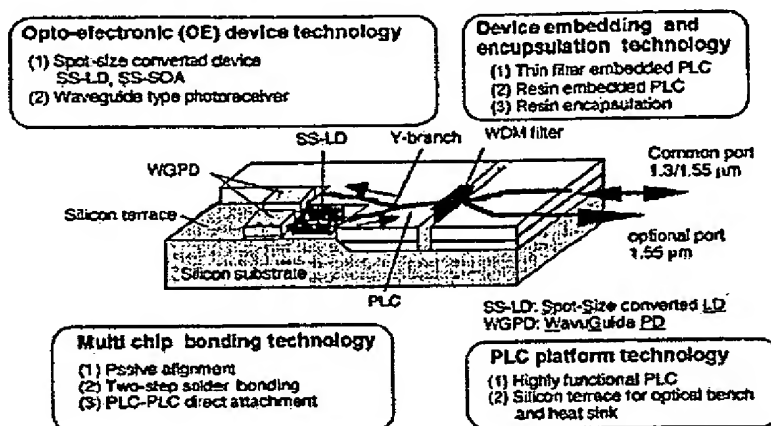
Figure 6. Example of the various devices that can be integrated on a silica based lightwave circuit. SS-LD stands for laser diode, WGPD stands for photodetectors (from [32]).

Hybrid integration of active components and silica-based planar lightwave circuits provides a full scheme for photonic component integration within a chip [32]. Passive components are realized by using silica waveguides while active components are hybridized within the silica (see figure 6). Active components (laser diodes, semiconductor optical amplifiers and photodiodes) are flip-chip bonded on silicon terraces where the optical waveguides are also formed. By using this approach, various photonic components have been integrated such as multi-wavelength light sources, optical wavelength selectors, wavelength converters, all optical time-division multiplexers etc [32]. Foreseen applications are WDM transceiver modules for fibre-to-the-home application.

A full integrated optical system based on silicon oxynitride waveguides, silicon photodetectors and CMOS transimpedance amplifiers has been realized [18]. Coupling of visible radiation to a silicon photodetector can be achieved by using mirrors at the end of the waveguide (figure 5). These are obtained by etching the end of the waveguide with an angle so that the light is reflected at almost 90° into the underlying photodetector. A schematic diagram of the cross-section of the device is shown in figure 7.

Commercial systems for the access network telecom market have been realized by using SOI waveguides and the silicon optical bench approach to interface the waveguides with both III–V laser sources and III–V photodetectors. The silicon optical bench (SOB) is a technology where the silicon wafer is used as a substrate (*optical bench*) where the various optical components are inserted by micromachining suitable lodging. In [24], lasers and photodetectors are stuck into etched holes in silicon and bump soldered in place. The system operates at 1.55 μm with a typical bit rate of 155 Mb s^{-1} [24]. A further advantage of the use of a large optical mode waveguide is the ease of interfacing to single-mode optical fibre. In the approach of [24], these are located in V-grooves etched into silicon.

A fully integrated system working at 1.55 μm has been demonstrated based on silicon waveguides with very small optical mode (cross-section 0.5×0.2 μm^2) which allows extremely small turn radii (1 μm) [11]. In this way a large number of optical components can be integrated on a small surface ($\approx$10 000 components cm^{-2}). Detectors are integrated within silicon by using Ge hetero-growth on silicon itself. Responsivity of 250 mA W^{-1} at 1.55 μm and response times shorter than 0.8 ns have been achieved [28]. A scheme for an optical clock distribution
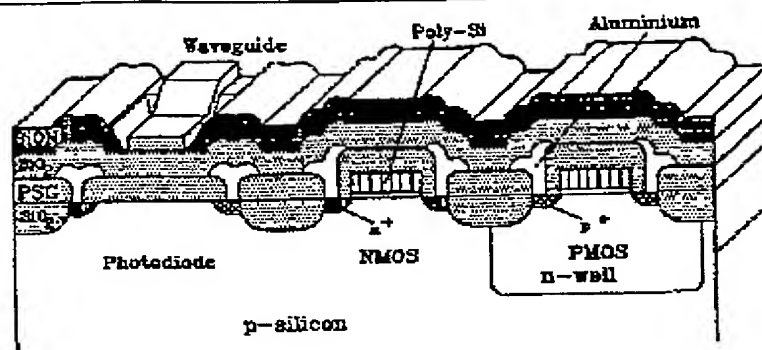
Figure 7. Cross section of an integrated device with a photodiode (PD) (left), the waveguide coupled to the PD by the TIR mirror and an amplifier stage realized with CMOS technology (from [18]).
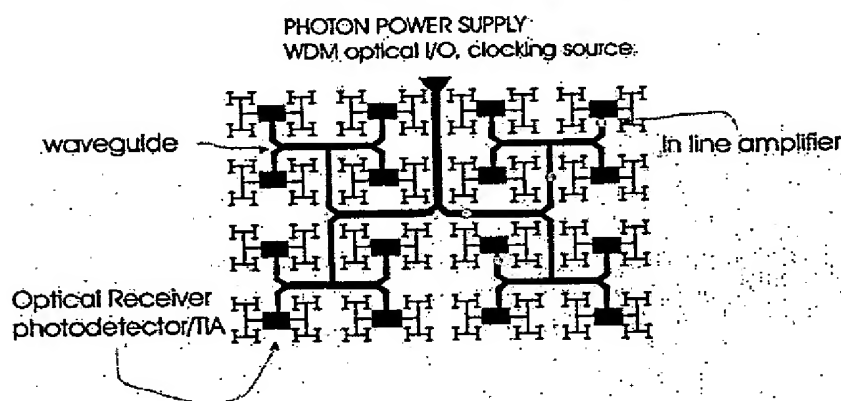

Figure 8. Scheme for an integrated optical circuit to distribute the clock signal on a chip (from [33]).

within integrated circuits based on this approach is shown in figure 8 [33]. Here the laser source is external to the chip and acts as a *photon battery* similarly to usual batteries for electrons.

A realistic bidirectional optical bus architecture for clock distribution on a Cray T-90 supercomputer board based on polyimide waveguides (loss of 0.21 dB cm^{-1} at 850 nm), a GaAs VCSEL and silicon MSM photodetectors has been investigated [34]. By using 45° TIR (total internal reflection) mirror coupling efficiencies as high as 100% among the sources or the detectors and the waveguides have been demonstrated. Examples of the connection scheme are shown in figure 9.

3. Silicon laser

To achieve monolithically integrated silicon microphotonics, the main limitation is the lack of any practical Si-based light sources: either efficient light emitting diodes (LEDs) or Si lasers. A laser is preferred as incoherent emission is probably not sufficient for dense, high speed interconnects mostly because of the basic optical inefficiencies in focusing incoherent light. A laser is ideal for optical interconnects, or more generally speaking, for silicon
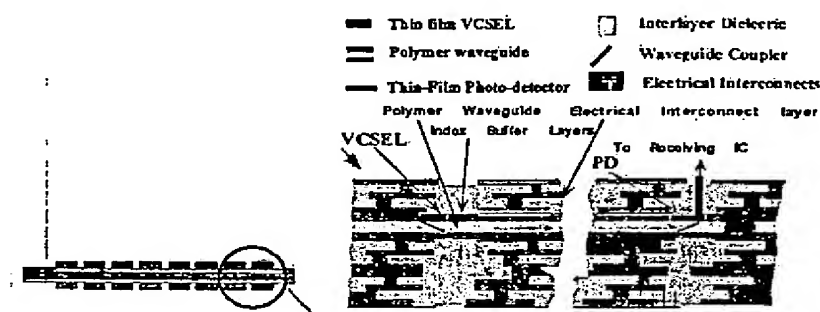
Figure 9. The optical interconnect scheme proposed in [34] for a supercomputer board: left, schematic diagram of the side view of the vertical integration layers; right, details of the schematic diagram (from [34]).

microphotonics. Unfortunately, today, the only viable solution is the hybrid approach where III–V semiconductor lasers are grown, bonded or connected to silicon photonic integrated circuits. To have a silicon laser, or in general a laser, one needs three key ingredients:

(i) an active material which should be luminescent in the region of interest and which should be also able to amplify light,

(ii) an optical cavity into which the active material should be placed to provide the positive optical feedback and

(iii) a suitable and efficient pumping scheme to achieve and sustain the laser action; for integration purposes the pumping mechanism is preferable via electrical injection.

Silicon is an indirect bandgap material; light emission is a phonon-mediated process with low probability (spontaneous recombination lifetimes in the milliseconds range) [35]. In standard bulk silicon, competitive non-radiative recombination rates are much higher than the radiative ones and most of the excited e–h pairs recombine non-radiatively. This yields very low internal quantum efficiency ($\eta_i \approx 10^{-6}$) for bulk silicon luminescence. In addition, fast non-radiative processes such as *Auger* or *free-carrier* absorption severely prevent population inversion for silicon optical transitions at the high pumping rates needed to achieve optical amplification. Despite all this, during the 1990s many different strategies have been employed to overcome these materials limitations [35]. The most successful ones are based on the exploitation of low dimensional silicon where silicon is nanostructured and hence the electronic properties of free carriers are modified by quantum confinement effects [13]. A steady improvement in silicon LED performances has been achieved and silicon LEDs are now within the strict market requirements [36]. In addition, many breakthroughs have been recently demonstrated showing that this field is very active and still promising [36–40]. Figure 10 shows a schematic sketch of the various strategies that are currently followed to build a silicon laser [41]. They differ both for spectral region of emission and for the physics behind. In the following, I will review all these approaches and try to weigh them up.

3.1. Bulk silicon

Silicon is an indirect bandgap material, thus the probability for a radiative transition is very low. This is reflected in very long times for radiative recombinations. Due to these long radiative lifetimes, excited free carriers have large probabilities of finding non-radiative recombination

Silicon nanocrystals

Er doped Silicon nanocrystals

Silicon-Germanium
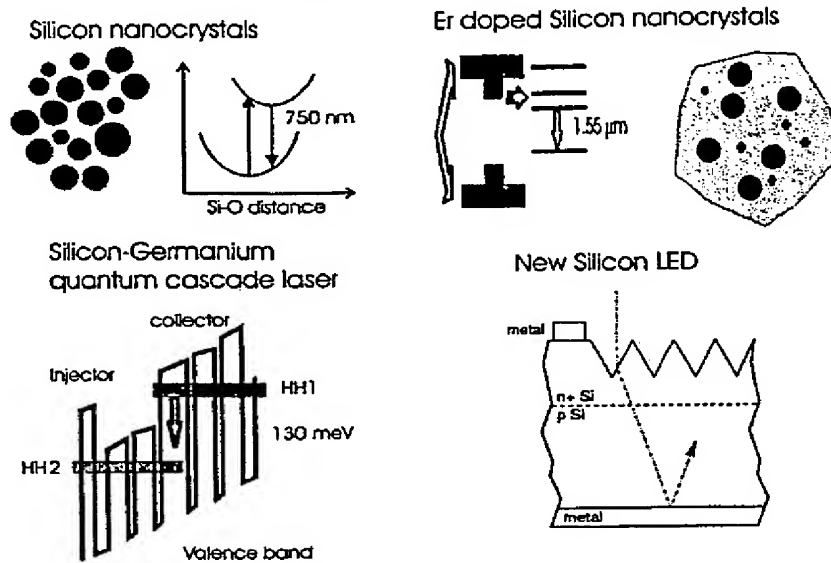quantum cascade laser

New Silicon LED

Figure 10. Various approaches proposed to realize a silicon laser.

centres and recombining non-radiatively. Room temperature emission in bulk silicon with high efficiency has only been observed in ultra-pure silicon with the surface passivated by a native oxide where excited carrier lifetimes are dominated by radiative recombination. Extremely slow recombination rates are possible with high efficiency if one is able to reduce to a minimum the competing non-radiative recombinations. This idea to increase the quantum efficiency of Si has been followed by two different approaches to develop Si based light emitting diodes [36, 42].

The first approach is based on the results achieved in high efficiency solar cells and on the consideration that, within thermodynamic arguments, absorption and emission are two reciprocal processes [36]. At first the non-radiative rates are reduced by using

(1) high-quality intrinsic Si substrates, float zone (FZ) being preferred over Czochralski (CZ),
(2) passivation of surfaces by high quality thermal oxide, in order to reduce surface recombination,
(3) small metal areas and
(4) limiting the high doping regions to contact areas, in order to reduce the Shockley–Read–Hall recombinations in the junction region.

Then, the parasitic absorption of photons once they have been generated is reduced to a minimum. For example, the reabsorption can be minimized by keeping the doping level to moderate values, such as $\sim 1.4 \times 10^{16}$ cm^{-3}. Finally, the extraction efficiency of light from bulk silicon can be enhanced by suitably texturizing the Si surface. The final device structure is shown in figure 11. Green *et al* [36] report the highest power efficiency to date for Si based LEDs, approaching 1%. Electroluminescence (EL) spectra of these devices (figure 12) are typical for band-to-band recombinations in silicon. In addition, a fully integrated opto-coupler device (LED coupled to a photodetector) was also demonstrated on the basis of this technology [43].
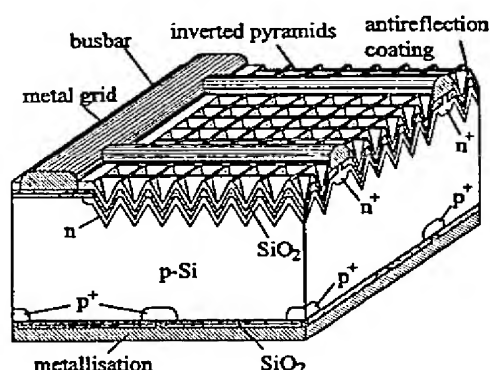
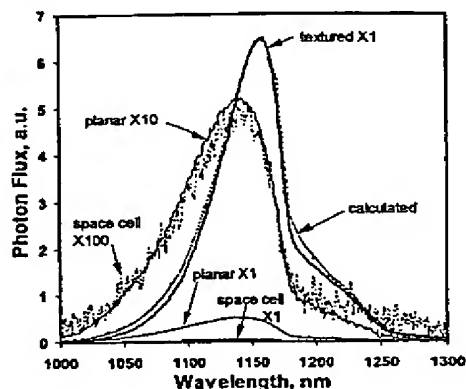Figure 11. Design of the textured Si light emitting device after [36].

Figure 12. EL spectra for textured, planar and baseline space cell diodes under 130 mA bias current at 298 K (diode area 4 cm^2). Calculated values assume a rear reflectance of 96% (after [36]).
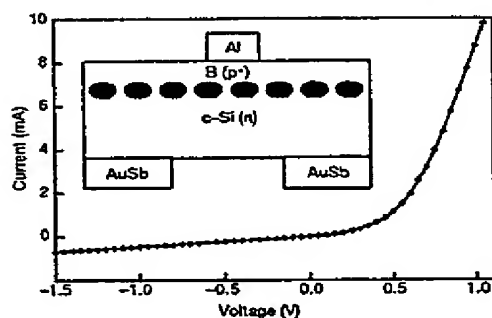

Figure 13. Current–voltage characteristics for the dislocation loop LED measured at room temperature. Inset: a schematic diagram of the LED where the grey circles evidence the region rich in dislocation loops (after [42]).

The main drawbacks of this approach for an integrated laser or light emitting diode are the following:

(i) the need for both high purity (low doping concentration) and surface texturing renders the device processing not compatible with standard CMOS processing;

(ii) the strong and fast free-carrier absorption typical of bulk Si, that can prohibit reaching the condition for population inversion, is not addressed [44];

(iii) the suitable integration of the active bulk Si into an optical cavity to achieve the required optical feedback to sustain a laser action can be a problem;

(iv) the modulation speed of the device can be limited by the long lifetime of the excited carriers (milliseconds) and by the need for a large optical cavity.

A somewhat different approach was reported in [42]; see figure 13. The idea was again a reduction of the non-radiative channels by exploiting the strain produced by localized dislocation loops to form energy barriers for carrier diffusion. Dislocations form potential pockets close to the junction which block the carriers and enhance radiative decay by localizing
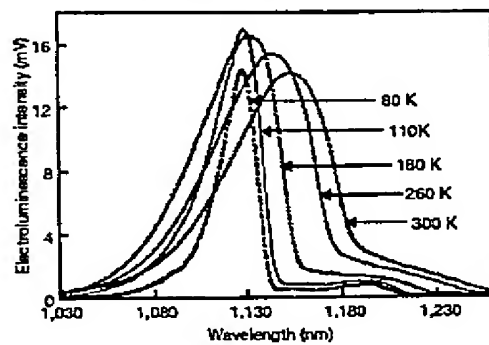
Figure 14. EL spectra against wavelength at various temperatures. The device was operated at a forward current of 50 mA for all temperatures (after [42]).

them in defect-free regions. The size of dislocation loops was in the range of 100 nm, i.e. not enough to cause a quantum confinement of the carriers, and the loop distances were of the order of 20 nm. Free carriers injected through the top electrode are not able to diffuse away and then are constrained to recombine in the near junction region. The onset of the EL at the band edge was observed as the diode turns on under forward bias. No EL was observed under reverse bias. An ultimate external quantum efficiency of about 1% is claimed for these LEDs. The EL spectrum does not present significant differences in lineshape and peak position compared to that of bulk Si (figure 14). A remarkable feature of this device is the high injection efficiency into the confined regions. This is due to the lack of quantum effects. In fact, since the density of states in the active zone is large (comparable to the bulk value), it is not a limiting factor for the free-carrier injection, in contrast to quantum confined structures. On the other hand, injection is also smooth because there is no wide bandgap material as confining barrier. Although not explained, this device has the additional and interesting feature of increasing the efficiency with temperature. The positive role of dislocation loops in enhancing luminescence from near surface silicon has been further confirmed by other authors [45, 46]. The main problem of this approach for a silicon laser is that it does not remove the two main problems of silicon which prevent population inversion, i.e. Auger recombination and free-carrier absorption [44].

Finally, a problem is also related to the wavelength of emission of these bulk silicon LEDs which is resonant with the silicon bandgap: that means that it is very difficult to control the region where the light is channelled in silicon if one wants to use these LEDs as a source for optical interconnects. Light will propagate through the wafer and will be absorbed in unwanted places.

3.2. Silicon nanocrystals

Another way to increase the emission efficiency of silicon is to turn it into a low dimensional material and, hence, to exploit quantum confinement effects to increase the radiative probability of carriers. This approach has been pioneered by the work on porous silicon (PS) [49] which shows that when silicon is partially etched in an HF solution via an electrochemical attack, the surviving structure is formed by small nanocrystals or nanowires which show bright red luminescence at room temperature. The explanation of the observed high luminescence efficiency in PS was
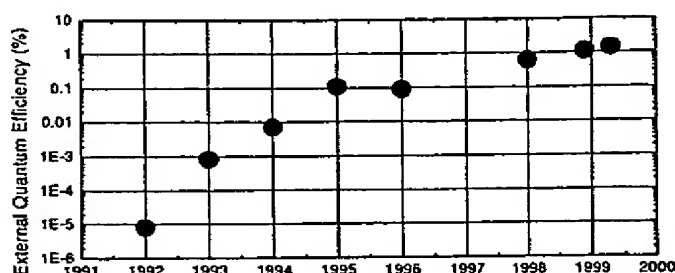
Figure 15. External quantum efficiency of PS LEDs over the year. The record in efficiency to date is that of [51].

(i) quantum confinement which leads to an enlargement of the bandgap and to an increased recombination probability,

(ii) the spatial confinement of the free carriers which prevents them reaching non radiative recombination centres and

(iii) the reduction of the refractive index of the material which increases the extraction efficiency via refractive index matching.

This result has motivated many research efforts in order to exploit these properties in LEDs [50]. The evolution of PS LED performances over the year is reported in figure 15 [51].

The PS approach has however a draw-back in the high reactivity of the spongelike texture which causes the rapid ageing of the LED and an uncontrollable variation of the LED performance with time [50]. No optical gain was reported in bulk PS. From PS, silicon nanocrystals (Si-nc) can be obtained by scrapping or ultrasonically dispersing PS [52]. Then the surface chemistry can be adjusted and, in particular, oxide passivated. Evidence of amplification in these materials has been presented [53].

An alternative way is to produce silicon nanocrystals (Si-nc) in a silica matrix to exploit the quality and stability of the SiO_2/Si interface and the improved emission properties of low dimensional silicon. Many different approaches have been proposed to form the silicon nanocrystals [13, 53]. The most widely used are based on the deposition of sub-stoichiometric silica films, with a large excess of silicon, followed by a high temperature annealing [54]. The annealing causes a phase separation between the two constituent phases, i.e. silicon and SiO_2 with the formation of small silicon nanocrystals. The size and density of the Si-nc can be controlled by the deposition and the annealing parameters. Recently, the anneal of amorphous SiO/SiO_2 superlattices has been proposed to control the size distribution. Almost monodispersed size distribution has been demonstrated [55].

The luminescence properties of Si-nc are very similar to those of PS: a wide emission band is observed at room temperature whose spectral position depends on the Si-nc sizes. In these systems optical gain has been observed [37, 53, 56–62]. Optical gain in Si-nc has been revealed as a superlinear increase of the luminescence intensity as a function of the pumping rate [53, 59], as the measurements of amplified spontaneous emission (ASE) in a waveguide geometry [37, 56, 57, 60–62] (see figures 16–18), as probe amplification in transmission experiments under high pumping excitation [37] or as collimated and speckled patterned emissions which show the coherent properties of the emitted light [59]. Some concerns have been raised about the methods used to measure the gain [63]. Almost all the authors agree on the fact that the gain is due to localized state recombinations either in the form of silicon dimers or in the form of Si=O bonds formed at the interface between the Si-nc and the oxide
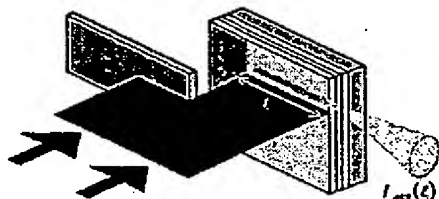
Figure 16. Sketch of the variable stripe length method to measure optical gain. The amplified spontaneous luminescence intensity I_{ASE} is collected from the edge of the sample as a function of the excitation length l. The laser beam is focused on a thin stripe by a cylindrical lens.
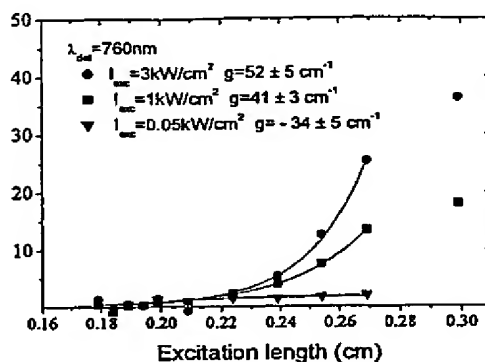
Figure 17. Room temperature VSL curves on a Si-nc sample as a function of the pumping intensities. The detection wavelength was 760 nm. By increasing the pumping intensity from 0.05 kW cm^{-2} to 1 kW cm^{-2} the optical losses turn into optical gain. The values of optical gain become saturated at an intensity of 3 kW cm^{-2} (from [62]).
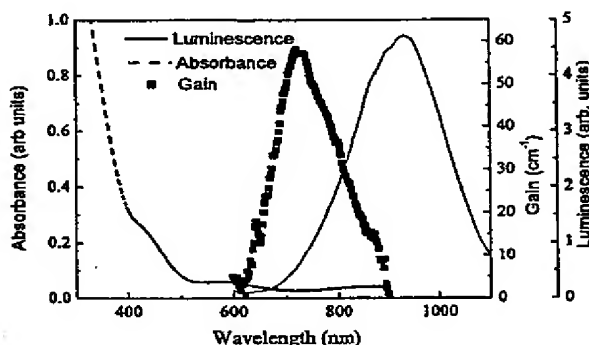

Figure 18. Absorbance (dashed curve), modal gain spectrum (solid squares) and luminescence spectrum (solid curve) for a Si-nc sample (from [62]).

or within the oxide matrix. The suggested scheme to explain population inversion, and hence gain, is a four-level model where a large lattice relaxation of the photoexcited localized centre gives rise to the four levels (figure 19) [56, 62].

Very interesting information can be achieved by time resolved experiments of the ASE from Si-nc in a waveguide geometry [56, 57, 62]. Figure 20 reports the decay lineshape of the ASE both as a function of the pumping fluences (figure 20(a)) and as a function of the excited length (figure 20(b)). In addition to the usual slow recombination of Si-nc (microseconds range), a fast contribution (nanosecond timescale) is observed which grows up either by increasing the fluence or by increasing the excitation length. This last observation rules out Auger recombination as the cause of the fast component because of its strongly non-linear dependence on the photo-excited carrier concentration, which in figure 20(b) is constant for all the various lengths. The origin of the fast component in these Si-nc is stimulated emission. This is also supported by other experimental data.
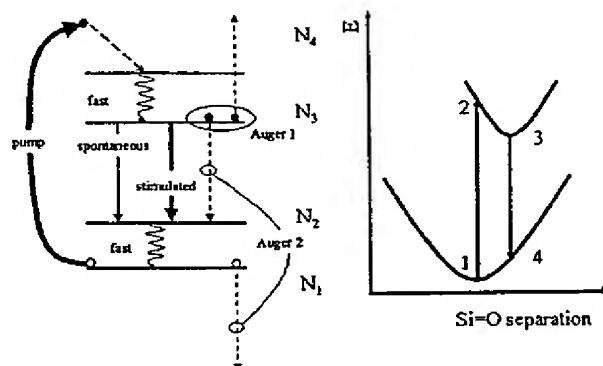
Figure 19. Left, effective four-level system based on the results of figure 18, which has been introduced to model qualitatively the recombination dynamics under gain conditions. From level 3 the excited carriers can recombine by spontaneous, stimulated or Auger recombinations. Right, schematic diagram of the energy configuration diagram of the silicon nanocrystals in an oxygen rich matrix. Localized radiative states are formed inside the nanocrystal bandgap by the interface oxygen atoms. The excited nanocrystal state can occur at a different lattice coordinate with respect to the ground state (from [62]).
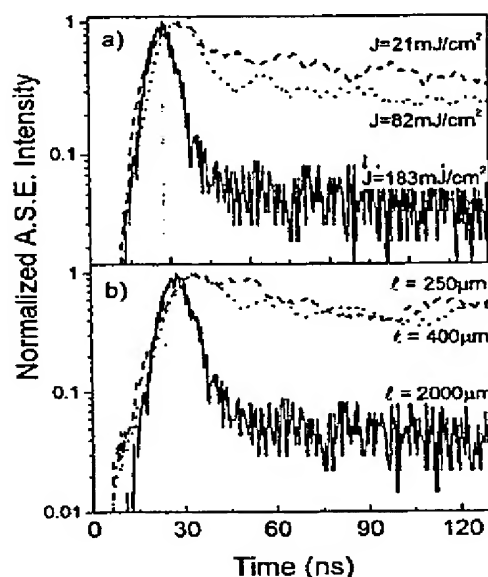

Figure 20. (a) Normalized ASE measured under VSL geometry with a pumping length $l = 2$ mm at the different pumping fluences reported in the figure. The measured sample is a Si-nc waveguide. Excitation wavelength was 355 nm. (b) Here the effect of the pumping length l on the fast ASE dynamics is shown. The pumping fluence is fixed at 183 mJ cm^{-2} and only the pumping length is varied according to the values reported in the figure (from [62]).

Figure 21(a) reports the exponential increase of the fast component intensity as a function of the photoexcited volume (which yields a net modal gain of 12 cm^{-1} under these pumping conditions). Figure 21(b) shows a clear fluence threshold over which the ASE increases
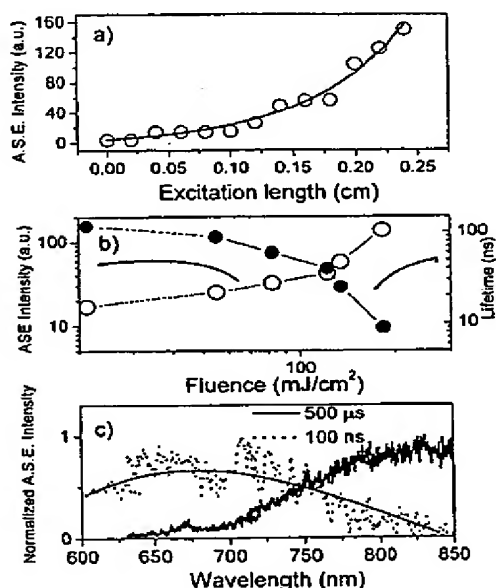
Figure 21. (a) Points: ASE peak intensity at 760 nm versus the excitation length at a pump fluence of 200 mJ cm^{-2}. Full curve: fit of the experimental data with the one-dimensional amplifier model which yields a net modal gain value of 12 ± 3 cm^{-1}. (b) Open circles: ASE peak intensity of the fast component versus the pumping fluence. Black discs: $1/e$ lifetime of the ASE decay as a function of the pumping fluence. Excitation length was approximately $l = 2$ mm. (c) ASE spectra measured for a fixed excitation length $l = 2$ mm and pumping fluence of 200 mJ cm^{-2} for two different integration time windows: dotted curve, 100 ns after the excitation; full curve, 500 μs after the excitation. All the data in this figure have been taken with an excitation wavelength of 355 nm (from [62]).

superlinearly with the fluences, and the decay lifetime of the emission decreases to a few nanoseconds. Figure 21(c) shows that the spectral shape of the fast component is different from the one of the slow component reflecting the typical blue shift of the gain band with respect to the luminescence (figure 18) which supports the four-level model of figure 19. The four-level model is also able to reproduce the decay of the luminescence at high fluences for Si-nc as demonstrated in figure 22. In the simulation of figure 22 both stimulated emission and Auger recombination are taken into account. At the peak fluence the lifetimes associated with these two processes are only slightly different. It is also this delicate interplay between Auger recombination and stimulated emission that governs the optical gain in Si-nc. As discussed in [62], the Si-nc density should be large enough to yield a significant optical gain. This means that optical gain cannot be achieved in all Si-nc samples. It is interesting to note that the data of figure 22 cannot be fitted with only Auger recombinations, even with peak Auger lifetimes as short as 90 ps. The contribution from stimulated emission is needed to accurately reproduce the luminescence decay.

The Si-nc system is very promising to achieve a laser. Indeed, other key ingredients for a laser have been demonstrated. Vertical optical micro-cavities based on a Fabry–Perot structure with mirrors constituted by distributed Bragg reflectors (DBRs) and where the central layer is formed by Si-nc dispersed in SiO$_2$ have been already fabricated [64]. The presence of the thick SiO$_2$ layer needed to form the DBR can be a problem for electrical injection when
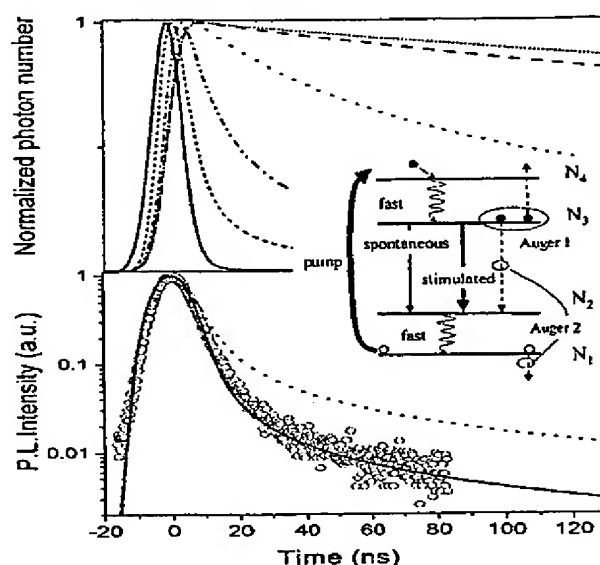
Figure 22. Top panel, simulations of the normalized PL intensity as a function of the incident photon flux ϕ_P. The peak of the incident photon flux ϕ_P was varied between 10^{16} and 10^{24} photons s^{-1} cm^{-2}. The main parameters used in the simulation were the pump absorption cross-section $\sigma_P = 10^{-14}$ cm^2, the emission cross-section $\sigma = 10^{-17}$ cm^2, the active centre concentration $N = 8 \times 10^{18}$ cm^{-3}, the spontaneous emission factor $\beta = 4.5 \times 10^{-4}$ and the optical losses $\alpha = 25$ cm^{-1}. No Auger recombination has been considered here. Bottom panel, PL decay (O) of Si-nc produced by PECVD deposition of 46 at.% Si annealed at 1250 °C for 1 h. The solid line is a simulation obtained with the same parameters as in the top panel plus an effective Auger coefficient $C_A = 10 \times 10^{-10}$ cm^{-3} s^{-1} (peak Auger lifetime of 3 ns) and a pump photon flux of 5×10^{22} photons s^{-1} cm^{-2}. The dashed line is a simulation where no stimulated emission was present, only Auger recombination. In this case an Auger coefficient of $C_A = 2 \times 10^{-8}$ cm^{-3} s^{-1} (peak Auger lifetime of 90 ps) is needed (courtesy of L Dal Negro).

current has to flow through the DBR. Lateral injection schemes can avoid these problems. On the other hand, the electrical injection into the Si-nc is a delicate task by itself[1]. Bipolar injection is extremely difficult to achieve. Despite some claims, most of the reported Si-nc LEDs are impact ionization devices: electron–hole pairs are generated by impact ionization by the energetic free carriers injected through the electrode. By exploiting impact ionization Si-nc LEDs have been demonstrated with EL spectra overlapping luminescence spectra, onset voltage as low as 5 V and efficiencies in excess of 0.1% [66]. Some unconfirmed claims of near-laser action of Si-nc LEDs have appeared in the literature [67, 68].

The problem of gain in Si-nc still has some unanswered issues:

(i) what is the role played by the Si-nc and by the embedding medium?
(ii) what are the key parameters which determine the presence of gain in the Si-nc?
(iii) is the nanocrystal interaction influencing the gain?
(iv) are low-losses active waveguides possible to achieve?
(v) what is the precise nature of the four levels in the model, in particular the location and role of Si–O bonds?

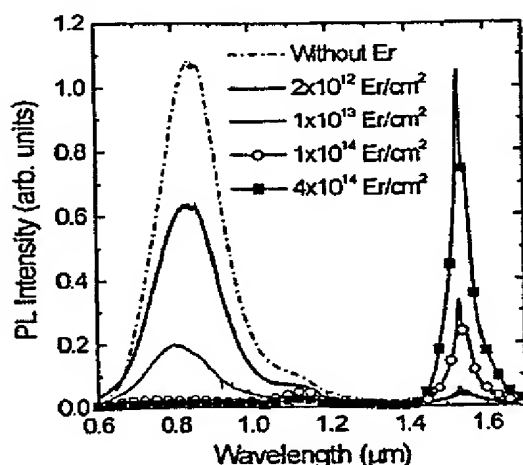[1] An introduction and up-to-date review can be found in [65].

Figure 23. Room temperature PL spectra of Er implanted Si nanocrystals at different Er doses. The pump power of the laser beam was 50 mW (after [74]).

3.3. Er coupled silicon nanocrystals

The recent increase in the transmission capacity of optical fibre based communication is also related to the availability of all-optical amplifiers based on Er doped fibres [69]. In this amplifier, a silica optical fibre is doped with Er^{3+} ions, whose internal atomic-like transition at $1.54\ \mu$m is exploited to achieve light amplification. In the past, several attempts have been made to reproduce a similar materials system in silicon. Several breakthroughs have been recently achieved in the field of Er doping of crystalline Si that allowed fabrication of LEDs operating at room temperature [71–73].

What it is more interesting for light amplification studies is the experimental finding of a strong enhancement of the Er luminescence when Er is implanted or deposited in a SiO_2 matrix where Si-nc have been formed, i.e. Si-nc act as sensitizers for erbium ions [74, 75]. Non-radiative de-excitation processes are reduced by widening the Si bandgap and thus avoiding one of the most detrimental sources of Er luminescence quenching. Indeed, the thermally activated back-transfer of excitation from Er^{3+} to Si-nc becomes less efficient than in bulk Si since the energy mismatch for the process becomes larger. Widening of the bandgap also produces a reduction in the free-carrier concentration, thus limiting the Auger processes. As demonstrated in figure 23, a strong luminescence comes from Er ions that are pumped through an electron–hole mediated process in which photo-excited excitons from Si nanocrystals transfer their energy to Er ions [74]. The number of Si-nc coupled to a single Er ion is still a debated issue (between one and ten) [74, 76]. As concerns where Er is placed, from high resolution luminescence it is clear that most of the Er is in the SiO_2 matrix, which is an ideal situation if one looks at reproducing the environment which is found in an Er doped fibre amplifier. Hence, Er coupled Si-nc benefits from the advantages of both silicon (efficient excitation) and SiO_2 (weak non-radiative processes, i.e. negligible temperature quenching of the luminescence), while it avoids their disadvantages (low excitation efficiency in SiO_2 and strong non-radiative processes in bulk Si). Indeed, MOS light emitting devices operating at room T have been made with this system, where a quantum efficiency larger than 1% [38] is demonstrated. Even higher efficiencies (10%) are reported for Er in silicon rich oxide films; however, in this system reliability is still an issue [39].
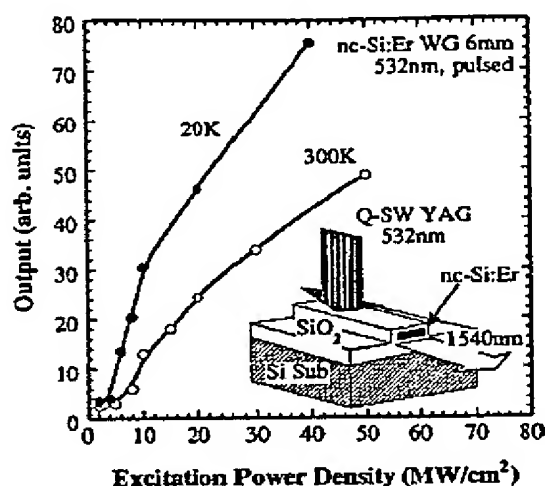
Figure 24. Pumping power density dependence of the 1540 nm emission of a 6 mm Er doped nc-Si waveguide (after [77]).

The layer co-doped with Si-nc and Er^{3+} ions has a refractive index which is larger than that of SiO_2, i.e. waveguides can be formed with a core containing Er^{3+} coupled to Si-nc. Experiments have shown luminescence increases (figure 24) [77] or even evidence of signal enhancement (figure 25) [78] are present in these waveguides. Even though no net optical gain was measured, an enhancement in the probe transmission at 1.535 μm was observed as the pump power was increased. By rather crude approximations, it is possible to write that the probe transmission when the pump is on, $I(P)$, is related to the probe transmission when the pump is off, $I(0)$, by $SE \equiv I(P)/I(0) = \exp(2(\sigma N_2 \Gamma)L)$, where SE is the signal probe enhancement, σ is the Er^{3+} emission cross-section at 1.535 μm, N_2 the density of excited Er ions, Γ the optical mode confinement factor and L the waveguide length. A fit to the experimental data yields an increased Er^{3+} emission cross-section with respect to Er ions in silica or in silicon (table 1) [40]. This is a quite unexpected result, which has however been confirmed by other research groups. The reason is still unclear; one can speculate about the role of the dielectric environment which is modified by the presence of the Si-nc [76]. What makes this finding interesting is the possibility of significantly reducing the cavity length in an amplifier or laser below the one usually employed in the silica doped fibre systems. Sizeable gain can be further obtained by low Er doping concentrations. To summarize the very interesting properties of the Er^{3+} coupled Si-nc system, table 1 compares the main cross-sections of Er^{3+} in silica and silicon and coupled with Si-nc.

The system Er^{3+} coupled to Si-nc is very promising for laser applications because the active material (Er^{3+} in SiO_2) has already shown lasing properties. In addition, the technology to produce the material is very compatible with CMOS processing. Microcavities with excellent luminescence properties have been also demonstrated [64], which allows design of both edge emitting and vertical emitting laser structures. The issue related to electrical pumping of the active material, which was believed to be a major short-cut of this approach, can be solved as extremely high efficiency LEDs have been demonstrated [38, 39]. A still open issue is to engineer the waveguide losses in order to be able to measure net optical gain and not only signal enhancement in a pump and probe experiment. This seems only a problem of time and
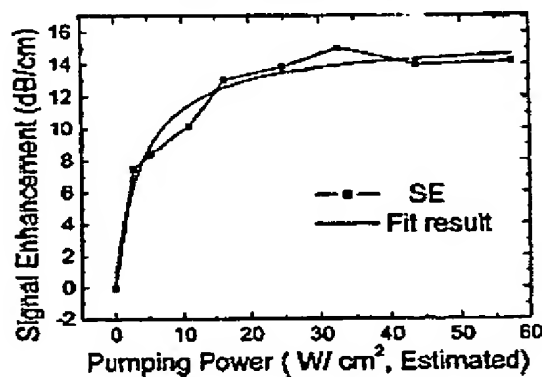
Figure 25. Pump power dependence of the signal enhancement SE and of a theoretical fit. An SE of up to 14 dB cm^{-1}, implying a possible net gain of up to 7 dB cm^{-1}, is found. From the fit, an emission cross-section of 2×10^{-19} cm^2 and an effective excitation cross-section of $> 10^{-17}$ cm^2 at 477 nm was deduced (from [78]).
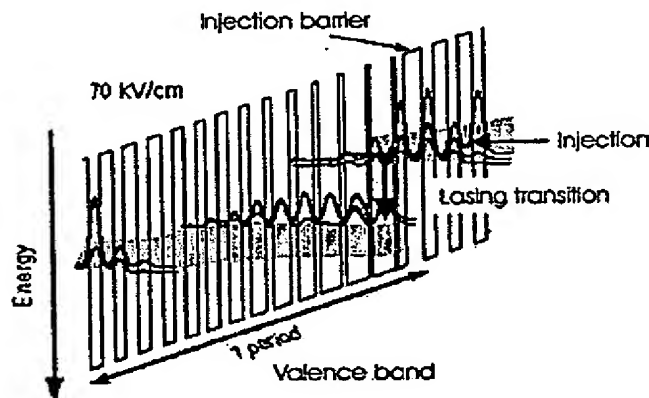

Figure 26. Schematic valence band diagram of one stage of the structure, under an applied electric field of 70 kV cm^{-1}. Only the HH band and the modulus squared of the relevant HH wavefunctions are shown for clarity. Note that the axis of the energy is turned upside down. Each period, starting from the injection barrier, consists of the following sequence of Si barrier (roman) and Si$_{0.2}$Ge$_{0.8}$ (bold) in Å: 25/11/4/26/5/26/6/24/7/21/8/19/9/18/10/17/11/15/12/15/13/14/15/14/16/13/17/13. The underlined numbers correspond to doped layers with a boron concentration of 5×10^{17} cm^{-3} (from [88]).

research efforts. Then further work should be spent to optimize the gain with respect to the waveguide parameters and develop a suitable optical cavity which can be electrically injected.

3.4. Si/Ge quantum cascade structures

One route to avoid the fundamental limitation to lasing in silicon, i.e. its indirect bandgap, is to avoid using interband transitions. Indeed, if one exploits only intraband transition, e.g. intra-valence-band transition, no fundamental problems exist to impede lasing in silicon [82]. This

Table 1. Summary of the various cross-sections related to Er^{3+} in various materials.

	Er in SiO_2 (cm^2)	Er in Si (cm^2)	Er in Si-nc (cm^2)	Reference for Er in Si-nc
Effective excitation cross-section of luminescence at a pumping energy of 488 nm	$(1-8) \times 10^{-21}$	3×10^{-15}	$(1.1-0.7) \times 10^{-16}$	[79, 80]
Effective excitation cross-section of EL		4×10^{-14}	1×10^{-14} by impact ionization	[38]
Emission cross-section at 1.535 μm	6×10^{-21}		2×10^{-19}	[40]
Absorption cross-section at 1.535 μm	4×10^{-21}	2×10^{-20}	8×10^{-20}	[81]

is indeed the approach of the quantum cascade (QC) Si/Ge system. With SiGe QC lasers, one is trying to use the concept that has already been successful in III–V semiconductors, which is advancing as a viable option for mid-IR emission, covering today a large wavelength range, 3–24 μm [83].

The idea of the device is shown in figure 26. The QC scheme can be implemented in the conduction or valence band. However, to achieve a conduction band discontinuity the growth of a Si/Ge superlattice on a relaxed SiGe buffer is necessary. For pseudomorphic growth on a Si substrate most of the band offset occurs in the valence band. Hence, the cascading scheme is usually designed in the valence band [84]. This differs from QC lasers based on III–V semiconductors that employ electron cascade structures. In figure 26, the valence band diagram of a cascading stage of a hole-injected p–i–p valence band device is shown. Injected holes make a vertical transition between subbands, and then they cascade down the electrically biased staircase. In order to assist population inversion, the lower laser level is rapidly depopulated by relaxation within the miniband. Practically, one has two identical active regions connected by an injector. EL from a SiGe QC structure grown on Si has recently been demonstrated [84, 88].

Starting from the possibility of monolithic integration with silicon microelectronics, the Si/SiGe system is more interesting than III–V heterostructures for QC laser applications. The non-polar electron–phonon interaction is the dominant loss process in III–V QC lasers. In silicon, due to the covalent bonding, the non-polar phonon scattering is absent. The optical phonon energy in Si is much higher than in GaAs (64 meV compared with 36 meV), providing a larger frequency window within which (non-polar) optical phonon scattering is suppressed. In Si the thermal conductivity is much larger than that of GaAs, giving better prospects of CW operation at non-cryogenic temperatures. On the other hand, some constraints are present [85]: the necessity to work in the valence band and thus the higher effective masses of the charge carriers, limited band offset of approximately 80 meV per 10% Ge concentration and splitting into heavy hole (HH) and light hole (LH) bands. Moreover, the high amount of strain, due to the lattice mismatch between Si and Ge, sets an upper limit to the number of wells per cascade and the number of cascades, as well as the thickness and Ge content of each individual well. Due to the mentioned constraints, the developed Si/SiGe cascade structure is a drastically simplified version of the typical III–V QC structures. As shown in figure 26, in a practical QC structure each cascade consists of only a few wells [85].

Figures 27 and 28 show the typical EL spectra recorded in QC structures grown on Si substrates [87, 88]. The levels involved are valence levels; the radiative transition is between HH states. The quantum efficiency estimate is about 10^{-5} for EL [85–88]. Temperature-
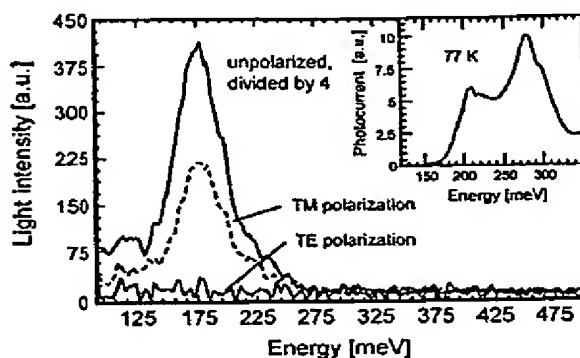
Figure 27. EL spectra of the sample with 15 repetitions, taken at 80 K with and without a polarizer placed in the light path. The parameters are 4.7 V, 550 mA, 94 kHz and a duty cycle of 10%. The polarized EL is measured at 5.2 V, 650 mA and a 20% duty cycle. The inset shows the results of a photocurrent measurement at 77 K (from [88]).
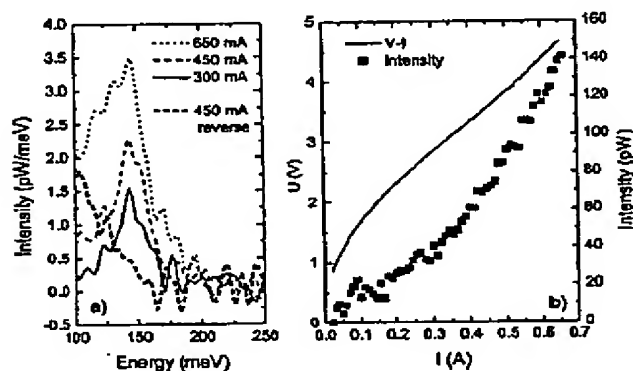

Figure 28. (a) Current-dependent EL spectra in forward bias and spectrum at reverse bias at 80 K. (b) I–V curve and integrated EL intensity (from [87]).

dependent measurements show nearly identical spectra between 20 and 90 K and a broadening and vanishing of the peak at about 160 K. It is possible to improve these results controlling the large accumulation of strain imposed by the use of a Si substrate. This has been done by using a $Si_{0.5}Ge_{0.5}$ substrate and growing on it strain compensated $Si_{0.2}Ge_{0.6}$/Si quantum wells. Intersubband transitions have been observed by absorption measurements at 235, 262 and 325 meV changing the well width from 3.5 to 2.5 nm; peaks are observed up to room temperature [88]. For similar structures EL has been detected at 80 K [88].

The QC concept works for III–V semiconductors. The SiGe system has some advantages and a fundamental limit posed on the number of periods of successive QW cascades which is given by the critical thickness for the formation of misfit dislocation. Hence, even though these devices show interesting EL properties for the prospect of the development of a Si based laser, highly evolved cascade structures have to be realized. As the gain per single element is low due to the nature of the intraband transition, a large number of cascading structures will be needed to accumulate a macroscopic gain. In fact, no stimulated emission in SiGe
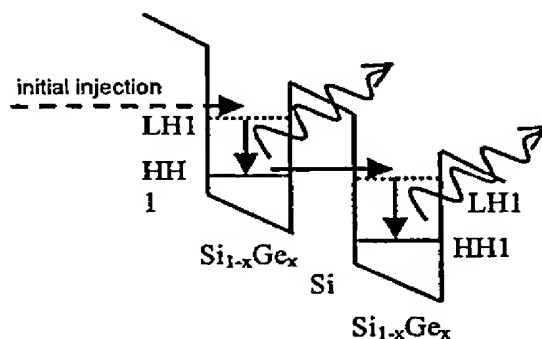
Figure 29. Schematic valence band profile of a Si/SiGe quantum staircase laser operating via radiative LH1–HH1 transitions (from [92] with kind permission of Kluwer Academic Publishers).

QC structures has been reported to date. In addition, all these have to be integrated within a waveguide cavity. In addition, the emission wavelength is different from those commonly used for optical interconnects. A waveguide for these wavelengths can be realized by using SOI substrates or thick, relaxed SiGe graded buffer. The other photonic components have still to be developed to achieve a photonic integrated system. Although some authors propose to use a QC laser for free-air optical interconnects, such a Si/Ge QC laser will be of little use for silicon photonics if all other compatible elements will not be developed.

3.5. THz emission

A gap in the frequency spectrum of electromagnetic waves opens across the THz region, where no semiconductor sources are available. At low frequencies, sources are made by electronic oscillators (high speed transistors) while at high frequencies the sources are made by injection lasers. Recently, a THz laser has been demonstrated by using III–V semiconductors which shows the way to cover this THz gap [89]. With the same aim, and using the many advantages of the SiGe system over the III–V systems for these frequencies, a research effort is made to implement the QC concept and make a laser in these frequency regions [90–92]. A typical structure is shown in figure 29 which by using p-type heterostructures is designed to emit radiation from LH–HH transitions. In this way both edge emission and surface-normal THz emission might be obtained. Growth of p-Si/SiGe QC structures comprising up to 100 periods has been demonstrated using low pressure CVD via a strain balanced approach on virtual substrates. Intersubband THz EL from a range of Si/SiGe QC structures has been observed in both edge and surface-emission geometries. An example is shown in figure 30. The LH–HH intersubband lifetime was measured to be ~20 ps, which is over an order of magnitude longer than high temperature values in III–V heterostructures, implying that a Si/SiGe THz QC laser may be capable of much higher operating temperatures than corresponding III–V devices. Emission power levels comparable to the one reported on III–V devices before laser processing have been measured which indicate that there are good prospects for realization of a THz Si/SiGe QCL via further optimization of the active region and appropriate cavity design [92].

Another approach to THz laser emission in silicon has been developed [93–96]. The idea is to make a THz laser using intra-shallow donor optical transitions in silicon. A band diagram showing the lasing transition is reported in figure 31. Very narrow spectral emission and the
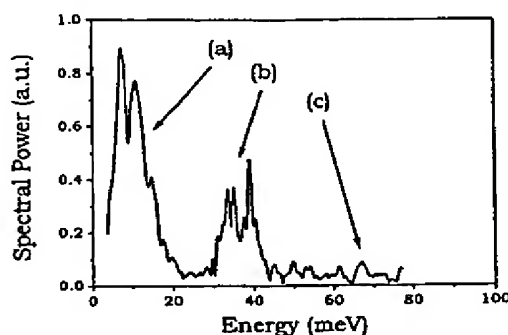
Figure 30. FTIR edge-emission spectrum for a QC structure, at a temperature of 4.2 K. The pulsed bias voltage was 7 V with a 10% duty cycle. The features marked (a), (b) and (c) correspond to the theoretically calculated emission peaks for the LH1–HH1, HH2–HH1 and LH2–HH1 intersubband transitions, respectively (from [92] with kind permission of Kluwer Academic Publishers).
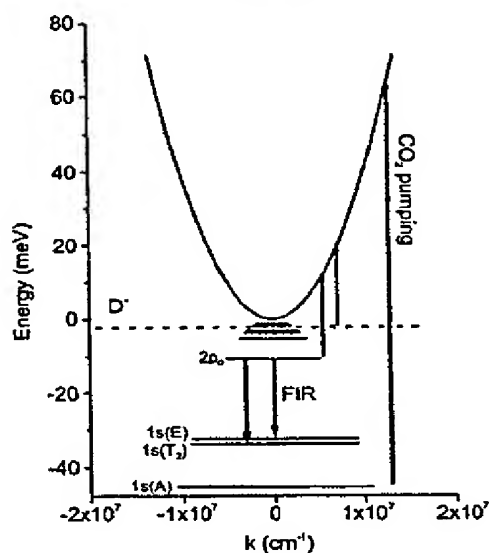

Figure 31. Optical transitions in Si:P. The dashed line represents the energy level of the D$^-$ centre state (from [96]).
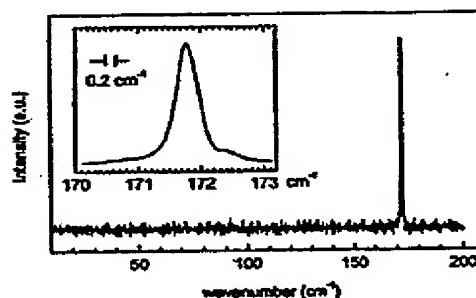
Figure 32. Stimulated emission spectrum from Si:Sb. The emission curve is identified with the 2p$_0$ → 1s intracentre Sb transition (from [96]).

light intensity threshold versus pumping power are reported in figures 32 and 33. All these data should indicate that lasing has been achieved in this system. However, some points need to be clarified, such as the optical mode pattern in the simple cavity structure used, the evolution from spontaneous to stimulated emission and the coherent property of the light. Other concerns are related to the dilute doping of the system in order to avoid impurity–impurity interaction which will prevent population inversion and the schemes for electrical injection. It is clear that the use of THz laser sources for silicon microphotonics requires a complete reshaping of the scheme developed up to now.
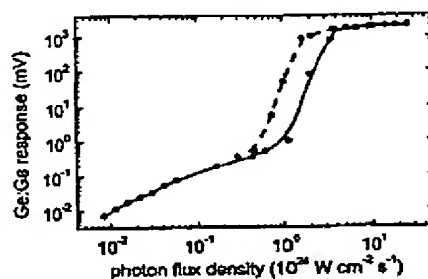
Figure 33. Dependence of the emission on the pump power for 9.6 μm excitation (dashed curve) or the 10.6 μm excitation (solid curve) (from [96]).

4. Conclusion

Throughout this review, I have tried to describe the status of silicon microphotonics and the recent advances that cause people to be optimistic to the realization of an active silicon light source. Indeed, many claims to have a silicon based laser within a short period have appeared in the literature by many of the researchers involved in this field [97]. If this objective is realized all the major building blocks for monolithic silicon microphotonics will be available.

The final vision is to have Si microphotonics participating in every global application of the photonics industry: communications, computing, information displays, optical-and-infrared imaging, medicine, optical printing, optical command-and-control, optical sensing of physical chemical and biological inputs, optical signal processing, optical storage and optical control of microwave devices or systems [98]. We indeed propose silicon as the unifying material where the next generation of photonics devices will be realized.

Acknowledgments

References

[1] Plummer J D, Deal M D and Griffin P B 2000 *Silicon VLSI Technology* (Upper Saddle River, NJ: Prentice-Hall)
[2] Clemens J T 1997 *Bell Lab. Tech. J.* Autumn 76
[3] International Technology Roadmap for Semiconductors, 2000 Update, Interconnect (http://public.itrs.net)
[4] Risch L 2002 *Mater. Sci. Eng.* C 19 363
[5] Theis T N 2000 *IBM J. Res. Dev.* 44 379
[6] ftp://download.intel.com/labs/eml/download/EML_opportunity.pdf
[7] Miller D A 2000 *Proc. IEEE* 88 728
[8] Moore S K 2002 *Spectrum IEEE*
[9] http://mph-roadmap.mit.edu/TWiGs.html#Si
[10] http://www.intel.com/research/silicon/index.htm
http://www.zurich.ibm.com/st/optics/index.html

http://us.st.com/stonline/bin/hilite.exe?file=/stonline/press/magazine/challeng/3rdedi02/
chal4.htm&words=PHOTONIC

[11] Kimerling L C 2000 *Appl. Surf. Sci.* 159/160 8

[12] Soref R A 1993 *Proc. IEEE* 81 1687

[13] Bisi O, Campisano S U, Pavesi L and Priolo F (ed) 1999 *Silicon Based Microphotonics: from Basics to
Applications* (Amsterdam: IOS Press)

[14] Masini G, Colace L and Assanto G 2002 *Mater. Sci. Eng.* B 89 2–9

[15] Pal B P 1993 *Progress in Optics* vol 32, ed E Wolf (Amsterdam: Elsevier) p 1

[16] Miya T 2000 *IEEE J. Sel. Top. Quantum Electron.* 6 38

[17] Bulla D A P *et al* 1999 *IMOC'99 Proc. IEEE* p 454

[18] Hilleringmann U and Goser K 1995 *IEEE Trans. Electron. Devices* 42 841

[19] Cocorullo G, Della Corte F G, Iodice M, Rendina I and Sarro P M 1998 *IEEE J. Sel. Top. Quantum Electron.* 4
983

[20] Lee K K, Lim D R, Luan Hsin-Chiao, Agarwal A, Foresi J and Kimerling L C 2000 *Appl. Phys. Lett.* 77 1617

[21] Rosa M A, Ngo N Q, Sweatman D, Dimitrijev S and Harrison H B 1999 *IEEE J. Sel. Top. Quantum Electron.* 5
1249

[22] Ang T W, Reed G T, Vonsovici A, Evans A G R, Routley P R and Josey M R 1999 *Electron. Lett.* 35 977

[23] Jalali B, Yegnanarayanan S, Yoon T, Yoshimoto T, Rendina I and Coppinger F 1998 *IEEE J. Sel. Top. Quantum
Electron.* 4 938

[24] Bestwick T 1998 *48th IEEE Conf. on Electronic Components and Technology (May 1998)* pp 566–71

[25] Zimmermann H 2000 *Integrated Silicon Optoelectronics* (New York: Springer)

[26] Csutak S M, Schaub J D, Wu W E, Shimer R and Campbell J C 2002 *J. Lightwave Technol.* 20 1724

[27] Yang M, Rim K, Rogers D L, Schaub J D, Wieser J J, Kuchta D M, Boyd D C, Rodier F, Rabidoux P A,
Marsh J T, Icknor A D, Yang Q, Upham A and Ramac S C 2002 *IEEE Electron. Device. Lett.* 23 395

[28] Masini G, Colace L, Assanto G, Wada K and Kimerling L C 1999 *Electron. Lett.* 35 1467
Colace L, Masini G, Assanto G, Luan H C, Wada K and Kimerling L C 2000 *Appl. Phys. Lett.* 76 1231

[29] Winnerl S, Buca D, Lenk S, Buchal Ch, Mantl S and Xu D X 2002 *Mater. Sci. Eng.* B 89 73

[30] El kuedi M *et al* 2002 *J. Appl. Phys.* 92 1858

[31] Coppola G, Irace A, Breglio G, Iodice M, Zeni L, Cutulo A and Sarro P M 2003 *Opt. Laser Eng.* 39 317

[32] Kato K and Tohmori Y 2000 *IEEE J. Sel. Top. Quantum Electron.* 6 4

[33] Kimerling L 2003 *Towards the First Silicon Laser (NATO Series vol 93)* ed L Pavesi, S Gaponenko and L Dal
Negro (New York: Kluwer) p 465

[34] Chen R T *et al* 2000 *Proc. IEEE* 88 780

[35] at press Ossicini S, Pavesi L and Priolo F 2003 *Light Emitting Silicon for Microphotonics (Springer Tracts in
Modern Physics)* (Berlin: Springer)

[36] Green M A, Zhao J, Wang A, Reece P J and Gal M 2001 *Nature* 412 805

[37] Pavesi L, Dal Negro L, Mazzoleni C, Franzò G and Priolo F 2000 *Nature* 408 440

[38] Iacona F, Pacifici D, Irrera A, Miritello M, Franzó G, Priolo F, Sanfilippo D, Di Stefano G and Fallica P G 2002
Appl. Phys. Lett. 81 3242

[39] Castagna M E, Coffa S, Caristia L, Messina A and Bongiorno C 2002 *Proc. ESSDDERC2002* p 439

[40] Han Hak-Seung, Seo Se-Young, Shin Jung H and Park Namkyoo 2002 *Appl. Phys. Lett.* 81 3720

[41] Pavesi L, Gaponenko S and Dal Negro L (ed) 2003 *Towards the First Silicon Laser (NATO Series vol 93)* (New
York: Kluwer)

[42] Ng W L, Lourenço M A, Gwilliam R M, Ledain S, Shao G and Homewood K P 2001 *Nature* 410 192

[43] Zhao J, Green M A and Wang A 2002 *J. Appl. Phys.* 92 2977

[44] Dumke W P 1962 *Phys. Rev.* 127 1559

[45] Gusev O B, Bresler M S, Yassievich I N and Zakharchenya B P 2003 *Towards the First Silicon Laser (NATO
Series vol 93)* ed L Pavesi, S Gaponenko and L Dal Negro (New York: Kluwer) p 21

[46] Sotta D 2002 Milieux emetteurs de lumiere et microcavites optique en silicium monocristallin sur isolant *Thesis*
Specialite physique, Universite Joseph Fourier Grenoble I

[47] Delerue C, Lannoo M, Allan G, Martin E, Mihalcescu I, Vial J C, Romestain R, Muller F and Bsiesy A 1995
Phys. Rev. Lett. 75 2229

[48] Jonsson P, Bleichner H, Isberg M and Nordlander E 1997 *J. Appl. Phys.* 81 2256

[49] Canham L T 1990 *Appl. Phys. Lett.* 57 1046

[50] Bisi O, Ossicini S and Pavesi L 2000 *Surf. Sci. Rep.* 264 1–126

[51] Gelloz B and Koshida N 2000 *J. Appl. Phys.* 88 4319

[52] Yamani Z, Thompson H, AbuHassan L and Nayfeh M H 1997 *Appl. Phys. Lett.* 70 3404

[53] Nayfeh M H, Barry N, Therrien J, Akcakir O, Gratton E and Belomoin G 2001 *Appl. Phys. Lett.* 78 1131

[54] Iacona F, Franzò G and Spinella C 2000 *J. Appl. Phys.* 87 1295

[55] Zacharias M, Heitmann J, Scholz R, Kahler U, Schmidt M and Bläsing J 2002 *Appl. Phys. Lett.* 80 661

[56] Dal Negro L, Cazzanelli M, Daldosso N, Gaburro Z, Pavesi L, Priolo F, Pacifici D, Franzò G and Icona F 2003 *Physica* E 16 297

[57] Khriachtchev L, Rasanen M, Novikov S and Sinkkonen J 2001 *Appl. Phys. Lett.* 79 1249

[58] Nayfeh M H, Rao S and Barry N 2002 *Appl. Phys. Lett.* 80 121

[59] Luterova K, Pelant I, Mikulskas I, Tomasiunaset R, Muller D, Grob J-J, Rehspringer J-L and Honerlage B 2002 *J. Appl. Phys.* 91 2896

[60] Fauchet P M and Ruan J 2003 *Towards the First Silicon Laser (NATO Series)* ed L Pavesi, S Gaponenko and L Dal Negro (New York: Kluwer) p 197

[61] Ivanda M, Densica U V, White C W and Kiefer W 2003 *Towards the First Silicon Laser (NATO Series)* ed L Pavesi, S Gaponenko and L Dal Negro (New York: Kluwer) p 191

[62] Dal Negro L, Cazzanelli M, Gaburro Z, Bettotti P, Pavesi L, Priolo F, Franzò G, Pacifici D and Icona F 2003 *Towards the First Silicon Laser (NATO Series vol 93)* ed L Pavesi, S Gaponenko and L Dal Negro (New York: Kluwer) p 145

[63] Valenta J, Pelant I and Linnros J 2002 *Appl. Phys. Lett.* 81 1396

[64] Icona F, Franzò G, Moreira E C and Priolo F 2001 *J. Appl. Phys.* 89 8354

[65] An introduction and up-to-date review can be found in Gaburro Z and Pavesi L 2003 Light emitting diodes for Si integrated circuits *Handbook of Luminescence, Display Materials, and Nanocomposites* ed H S Nalwa and L S Rohwer (Stevenson Ranch: American Scientific)

[66] Franzò G, Irreira A, Moreira E C, Miritello M, Icona F, Sanfilippo D, Di Stefano G F, Fallica F and Priolo F 2002 *Appl. Phys.* A 74 1

[67] Lin Ching-Fuh, Chung Peng-Fei, Chen Miin-Jang and Su Wei-Fang 2002 *Opt. Lett.* 27 713

[68] Heikkila L, Kuusela T T and Hedman H P 1999 *Superlatt. Microstruct.* 26 157

[69] Becker P C, Olsson N A and Simpson J R 1999 *Erbium-Doped Fibre Amplifiers* (London: Academic)

[70] Priolo F 1999 *Silicon Based Microphotonics: from Basics to Applications* ed O Bisi, S U Campisano, L Pavesi and F Priolo (Amsterdam: IOS Press) p 279
Polman A 1997 *J. Appl. Phys.* 82 1

[71] Franzò G, Priolo F, Coffa S, Polman A and Carnera A 1994 *Appl. Phys. Lett.* 64 2235

[72] Coffa S, Franzò G and Priolo F 1996 *Appl. Phys. Lett.* 69 2077

[73] Coffa S, Franzò G, Priolo F, Pacelli A and Lacaita A 1998 *Appl. Phys. Lett.* 73 93

[74] Franzò G, Vinciguerra V and Priolo F 1999 *Appl. Phys.* A 69 3
Franzo G, Pacifici D, Vinciguerraa V, Priolo F and Iacona F 2000 *Appl. Phys. Lett.* 76 2167

[75] Zacharias M, Heitmann M S J and Streitenberger P 2001 *Physica* E 11 245

[76] Kik P G and Polman A 2003 *Towards the First Silicon Laser (NATO Series)* ed L Pavesi, S Gaponenko and L Dal Negro (New York: Kluwer) p 383

[77] Zhao X, Komuro S, Isshiki H, Aoyagi Y and Sugano T 1999 *Appl. Phys. Lett.* 74 120

[78] Han Hak-Seung, Seo Se-Young and Shin Jung H 2001 *Appl. Phys. Lett.* 79 4568

[79] Priolo F, Franzo G, Pacifici D, Vinciguerra V, Iacona F and Irrera A 2001 *J. Appl. Phys.* 89 264

[80] Kenyon A J, Chryssou C E, Pitt C W, Shimizu-Iwayama T, Hole D E, Sharma N and Humphreys C J 2002 *J. Appl. Phys.* 91 367

[81] Kik P G and Polman A 2002 *J. Appl. Phys.* 91 534

[82] Soref R A 1997 *Thin Solid Films* 294 325

[83] Gmachl C *et al* 2001 *Rep. Prog. Phys.* 64 1533

[84] Dehlinger G, Diehl L, Gennser U, Sigg H, Faist J, Ensslin K and Grützmacher D 2000 *Science* 290 2277

[85] Dehlinger G, Diehl L, Gennser U, Sigg H, Muller E, Stutz S, Faist J, Stangl J, Roch T, Bauer G and Grützmacher D 2002 *Mater. Sci. Eng.* B 89 30

[86] Diehl L *et al* 2003 *Towards the First Silicon Laser (NATO Series vol 93)* ed L Pavesi, S Gaponenko and L Dal Negro (New York: Kluwer) p 325

[87] Bormann I, Brunner K, Hackenbuchner S, Zandler G, Abstreiter G, Schmult S and Wegscheider W 2002 *Appl. Phys. Lett.* 80 2260

[88] Diehl L, Mentese S, Sigg H, Müller E, Grützmacher D, Gennser U, Sagnes I, Fromherz T, Stangl J, Roch T, Bauer G, Campidelli Y, Kermarrec O, Bensahel D and Faist J 2002 *Appl. Phys. Lett.* 81 4700

[89] Kohler R, Tredicucci A, Beltram F, Beere H, Linfield E, Davies G, Ritchie D, Iotti R C and Rossi F 2002 *Nature* 417 156

[90] Lynch S A, Bates R, Paul D J, Norris D J, Cullis A G, Ikonic Z, Kelsall R W, Harrison P, Arnone D D and Pidgeon C R 2002 *Appl. Phys. Lett.* 81 1543

[91] Lynch S A, Dhillon S S, Bates R, Paul D J, Amone D D, Robbins D J, Ikonic Z, Kelsall R W, Harrison P, Norris D J, Cullis A G, Pidgeon C R, Murzyn P and Loudon A 2002 *Mater. Sci. Eng.* B 89 10

[92] Kelsall R W, Ikonic Z, Harrison P, Lynch S A, Bates R, Paul D J, Norris D J, Liew S L, Cullis A G, Robbins D J, Murzyn P, Pidgeon C R, Amone D D and Soref R A 2003 *Towards the First Silicon Laser (NATO Series)* ed L Pavesi, S Gaponenko and L Dal Negro (New York: Kluwer) p 367

[93] Pavlov S G, Hübers H-W, Rümmeli M H, Hovenier J N, Klaasen T O, Zhukavon R Kh, Muravjov A V and Shastin V N 2003 *Towards the First Silicon Laser (NATO Series vol 93)* ed L Pavesi, S Gaponenko and L Dal Negro (New York: Kluwer) p 331

   Shastin V N, Orlova E E, Zhukavin R Kh, Pavlov S G, Hübers H-W and Riemann H 2003 *Towards the First Silicon Laser (NATO Series vol 93)* ed L Pavesi, S Gaponenko and L Dal Negro (New York: Kluwer) p 341

[94] Shastin N, Zhukavin R Kh, Orlova E E, Pavlov S G, Rummeli M H, Hubers H-W, Hovenier J N, Klaassen T O, Riemann H, Bradley I V and van der Meer A F G 2002 *Appl. Phys. Lett.* 80 3512

[95] Blom A, Odnoblyudov M A, Cheng H H, Yassievich I N and Chao K A 2001 *Appl. Phys. Lett.* 79 713

[96] Pavlov S G, Zhukavin R Kh, Orlova E E, Shastin V N, Kirsanov A V, Hubers H-W, Auen K and Riemann H 2000 *Phys. Rev. Lett.* 84 5220

   Pavlov S G, Hubers H-W, Riemann H, Zhukavin R Kh, Orlova E E and Shastin V N 2002 *J. Appl. Phys.* 92 5632

[97] Ascombe N 2003 Seeking a silicon laser *Photon. Spectra* February 62

[98] Soref R A 1999 *Silicon Based Microphotonics: from Basics to Applications* ed O Bisi, S U Campisano, L Pavesi and F Priolo (Amsterdam: IOS Press) p 1

Quasicontinuous gain in sol-gel derived CdS quantum dots

J. Butty,[a] Y. Z. Hu, and N. Peyghambarian
Optical Sciences Center, University of Arizona, Tucson, Arizona 85721

Y. H. Kao and J. D. Mackenzie
*Department of Material Science and Engineering, University of California at Los Angeles,
Los Angeles, California 90024*

We report evidence for quasicontinuous optical gain in CdS quantum dots fabricated by the sol-gel process and embedded in glass. The gain spectra are obtained using the pump and probe technique and nanosecond (quasiresonant) excitation at 11 K. The dots are in the intermediate quantum confinement regime and the concentration of CdS is relatively high. The gain, which is spectrally broad, develops on the low energy side of the absorption band edge. The reason why the gain region is broad is not only the size distribution of the dots, but also the nature of the gain, which originates from the recombination of several excited levels between two and one electron-hole pairs states (i.e., biexciton to exciton). The maximum measured gain reaches 200 cm^{-1} at 11 K and 17 cm^{-1} at 170 K. © *1995 American Institute of Physics.*

Three-dimensionally quantum confined semiconductors are attractive because of the predicted enhanced optical properties with increasing confinement. Semiconductor quantum dots (QDs) have been investigated extensively,[1] but they have not shown superior emission properties. One known problem is the reduced radiative efficiency with decreasing dot as a result of surface recombination. For QDs in glass especially, limitations are the large size distribution of the dots, the presence of trap states (such as vacancies, substitutional defects, and dangling bonds), the observed photodarkening and low density of microcrystallites (active material) in the glass matrix.

Semiconductor crystallites in glass have a number of advantages including the relatively easy growth of QDs of different II–VI semiconductors by heat treatment and the possibility of fabricating low loss waveguides with ion exchange in the high quality glass matrix. The quality of our QDs has been improved with the use of the sol-gel synthesis:[2] high dot density, dots sizes much smaller than the bulk exciton Bohr radius a_{Bohr}, with more uniform size distribution, and an almost complete elimination of the photodarkening effect.[3]

Femtosecond dynamics of optical gain in strongly confined CdSe QDs have been recently studied using femtosecond (fs) optical excitation.[4] Gain in the weak confinement regime for CuCl crystallites in glass has been also studied at 77 K.[5]

In this letter, we report our measurement of the gain spectra of sol-gel derived CdS QDs glasses in the intermediate confinement regime and compare the results with the calculated gain for a quasi-zero-dimensional electron-hole system, accounting for one and two electron-hole pair states. Using the variable-stripe length method, we analyze the temperature dependence of the gain between 11 and 170 K.

The CdS nanocrystallites we investigated were fabricated by the sol-gel process.[2] 5.6 wt % CdS nanocrystallites were embedded in a fully dense $5Na_2O-15B_2O_3-80SiO_2$ (mol %) glass after heating at 590 °C. The transmission electron micrograph (TEM) in Fig. 1(a) shows that the average dot radius R was 2.8 nm with a distribution of σ (standard deviation)=1.0. The average radius R of the dots was on the order of the bulk exciton Bohr radius a_{Bohr}. Figure 1(b) shows a typical image of these nanocrystallites with high resolution transmission electron microscope (HRTEM: Topcon 002B, 200 kV). These crystallites of $R \approx 2.5$ nm (graphitized carbon internal standard) are both oriented perpendicularly to the (101) reflection plane. The electron and x-ray diffraction pattern of our sample show that the crystallites are of hexagonal symmetry.
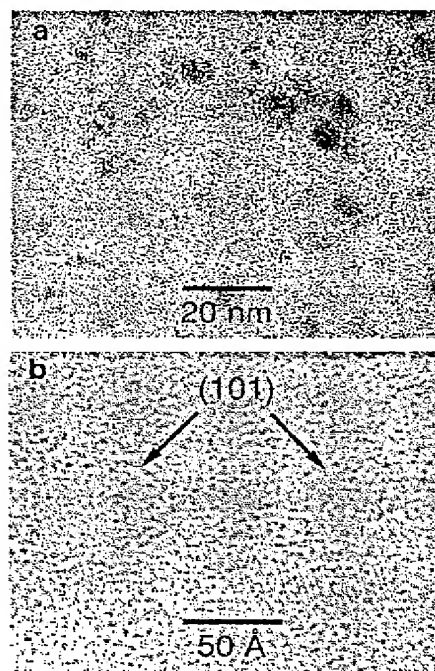

FIG. 1. (a) TEM micrograph and (b) HRTEM micrograph of the 5.6 wt % CdS-doped sodium borosilicate glass.

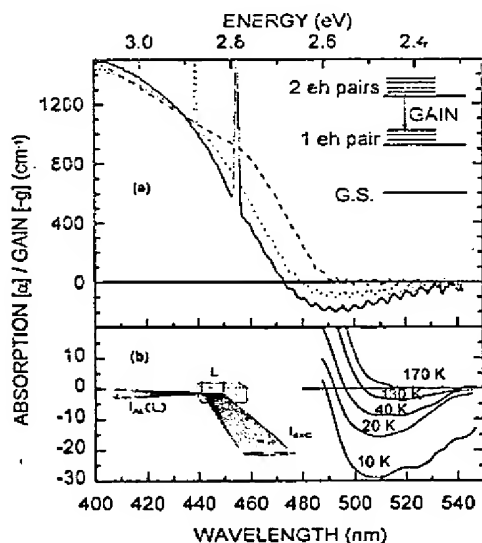[a] Electronic mail: jbutty@ccit.arizona.edu

FIG. 2. (a) Absorption (gain) spectra of CdS QDs measured at 11 K for different pump excitation intensities I_{exc}. The pump wavelength is 455 nm for the solid curve ($I_{exc}=I_0$) and 440 nm for the dotted curve ($I_{exc}=I_0/7$), with $I_0=570$ kW/cm^2. The dashed curve is the linear absorption spectrum. The inset shows a scheme of the energy levels considered for the model calculations: the ground state and the one and two electron-hole pairs levels with their excited states, and one of the recombinations which provides the optical gain. (b) Temperature dependence of the gain between 10 and 170 K. The spectra were measured with the variable-stripe-length method (see the inset), with an excitation intensity $I_{exc}=3I_0$ at 355 nm.

The glass sample was polished to a thickness of 17 ± 2 μm and held in a cryostat at $T=11$ K for optical characterization. Differential transmission (DTS) and absorption spectra have been measured in the common pump and probe technique, with 3 ns duration pump pulses at 10 Hz repetition rate. The probe beam, originating from the luminescence of a dye cell, had an 8 ns pulse duration and was cross polarized with respect to the pump to reduce the scattered light. The time delay between the pump and the probe pulses was less than 1 ns.

Figure 2(a) shows the absorption spectra for different pump intensities. A bleaching of the absorption spectrum is observed as the excitation intensity is increased. The position of the maximum (around 465 nm) does not change when we vary the pump wavelength, even for low excitation intensity. This can be interpreted as a low inhomogeneous broadening,[6] giving another indication of the relatively narrow size distribution of the QDs. A broad gain region (negative absorption), ranging from ≈470 to ≈540 nm, is observed for the highest pump intensity. These results are in agreement with the results of Dneprovskii *et al.*,[7] who have observed gain in CdSe QDs in the intermediate confinement regime. The maximum gain reaches about 200 cm^{-1} at 493 nm for an excitation intensity of $I_0=570$ kW/cm^2. The rapid oscillations in the gain region are Fabry–Pérot interferences, whose period corresponds to the sample thickness. The pump wavelength is 455 and 440 nm, respectively, for the two input intensities I_{exc}, as indicated by the sharp scattering signals. The comparison with the linear absorption spectrum (dashed curve) shows that the gain develops on the low energy side of the absorption band edge and extends well be-
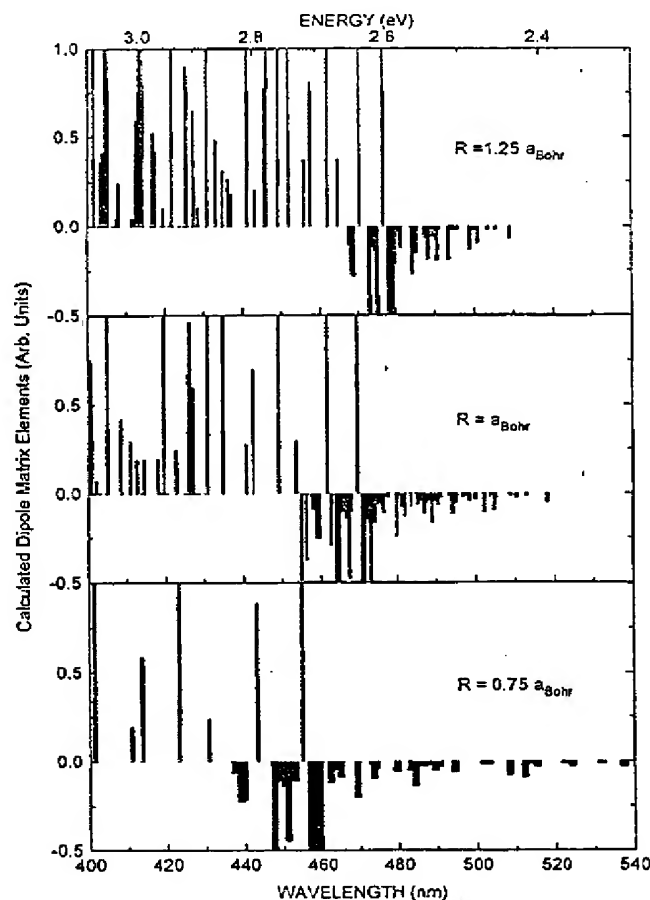

FIG. 3. Calculated absorption (gain) spectra. The bars correspond to the relative strength of the optical transitions between (i) the one electron-hole pairs and the ground state (positive=absorption) and (ii) the two electron-hole pairs and the one pairs states (negative=gain). Calculations are made for $R=0.75a_{Bohr}$, $R=a_{Bohr}$, and $R=1.25a_{Bohr}$ relative to the bulk bandgap value of CdS (2.56 eV) and without any broadening mechanism. The model takes into account the Coulomb interaction, the valence band mixing, and the surface polarization effects.

low the band edge. This behavior is expected of the gain involving two electron-hole (eh) pairs (biexciton) recombination.[8]

The temperature dependence of the gain between 11 and 170 K is presented in Fig. 2(b). The variable-stripe length method was used to measure the gain spectra.[9] The third harmonic of the Nd:YAG laser was focused onto the sample by using a cylindrical lens, to form a narrow rectangular stripe, 0.05–2 mm long and about 20 μm wide. The emitted light (i.e., amplified luminescence I_{AL}) was collected from the edge of the sample in the direction of the stripe, as shown in the inset of Fig. 2(b). The method allowed us to reproduce the gain spectra of Fig. 2(a) (solid line), when we pumped with $I_{exc}\approx8I_0$ at 355 nm. As expected, the gain decreases with increasing temperature, rapidly at the beginning (it is already two times smaller at 20 K), and it disappears around 170 K. With increasing the excitation intensity to 10 MW/cm^2, the maximum gain at 170 K was 17 cm^{-1}.

Figure 3 shows the calculated gain and absorption spectra in the absence of any broadening mechanism. The bars

Appl. Phys. Lett., Vol. 67, No. 18, 30 October 1995
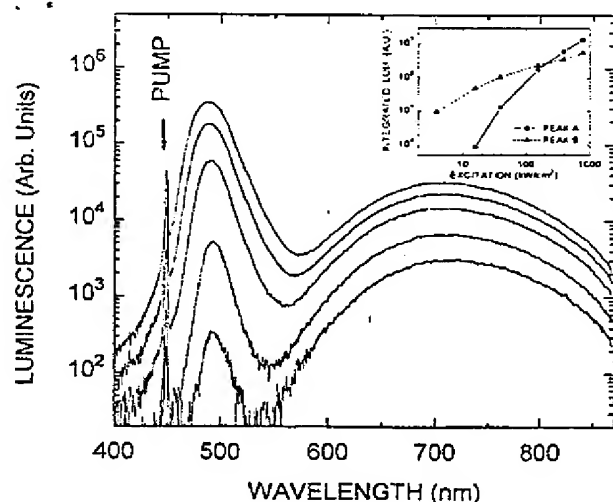
Butty et al.   2673

FIG. 4. Photoluminescence (PL) spectra at 11 K for different pump excitation intensities (from 4 to 770 kW/cm²). The intensities are in logarithmic scale. The narrow peak (at 490 nm) is attributed to excitonic recombination and the broad peak (around 700 nm) is probably due to trap states recombination. The pump wavelength is indicated on the figure. The inset shows the log–log plot of the integrated luminescence (areas) of the two PL peaks as a function of the pump excitation intensity. The circles are for the narrow peak surface (A) and the triangles are for the broad peak surface (B).

correspond to the calculated dipole matrix elements in relative units. The transitions between the one eh pair states and the ground state are shown as positive bars (above the baseline), and the transitions between two eh pairs and the one pair states are shown as negative bars (below the baseline). Calculations are made for three different confinement values: $R = 0.75a_{Bohr}$, $R = a_{Bohr}$, and $R = 125a_{Bohr}$, with an infinite quantum confinement potential. A detailed description of the calculation, which includes the numerical diagonalization of the Hamiltonian for the one and two eh pairs wave functions and the calculation of the eigenenergies and of the transitions dipole moments, will be published elsewhere.[8] The valence band mixing is accounted for by using the Luttinger Hamiltonian within the axial approximation [with $m_e = 0.1m_0$; $\gamma_1 = 5$; $\gamma_2 = \gamma_3 = 1.8$, $\epsilon = \epsilon_1/\epsilon_2 = 10$, where $\gamma_1, \gamma_2, \gamma_3$ are the Luttinger parameters and $\epsilon_1(\epsilon_2)$ is the dielectric constant inside (outside) the dot]. The model takes into account the several excited levels of the two and one eh pairs states (i.e., biexciton and exciton), which can have a recombination energy smaller than the ground states transition energy [see the inset of Fig. 2(a)]. The population among the different excited energy levels is assumed to be the same for each quantum dot level, as there is not a thermal distribution between the levels which can be populated by only one eh pair of the same quantum state. We see that the gain is due to these two eh pairs recombination which extend on the low energy side of the first one pair transition. As the quantum confinement is increased (see the lower part of Fig. 3), the gain reaches lower energies and the absorption is shifted to higher energies. Due to the size distribution of the QDs in our sample,

the light emitted by the strongest gain region around the band edge is reabsorbed by the bigger dots (upper part of Fig. 3).

We have taken photoluminescence (PL) spectra of the same sample (see Fig. 4). They show two emission bands as it is usually the case for the QDs in glass:[10] one broadband in the near-infrared, which is related to defects, and a narrower band at shorter wavelength, in the same range where the gain is observed. The excitation intensity dependence of the integrated luminescence of these two bands indicates that the narrow band is growing faster than the broad one with increasing excitation, supporting the fact that the broad emission is related to impurities or defects whereas the narrow emission band has an intrinsic character. The increase in the integrated luminescence of the narrow band is superlinear with the intensity. This can be understood because (i) the luminescence comes from biexcitonic recombination, (ii) there is stimulated emission in that region, and (iii) there are two different recombination channels, one intrinsic channel and one channel related to defects. At higher excitations, the defect-related channel saturates (see the inset in the Fig. 4).

In summary, CdS QDs in the intermediate quantum confinement regime show significant optical gain as high as 200 cm⁻¹ at low temperature. The gain persists up to 170 K, but it decreases with increasing temperature. The sample is fabricated by sol-gel process and has a relatively high concentration of CdS embedded in a borosilicate glass. Our model calculations indicate that the broad gain region we observe is not only due to the size distribution of the dots, but also to the fact that the gain originates from several excited states transitions between two and one electron-hole pairs.

[1] N. Peyghambarian, S. W. Koch, and A. Mysyrowicz, *Introduction to Semiconductor Optics* (Prentice-Hall, Englewood Cliffs, NJ, 1993), Chap. IX.
[2] Y. H. Kao, K. Hayashi, L. Yu, M. Yamane, and J. D. Mackenzie, SPIE Proc. **2288**, 752 (1994).
[3] K. Kang, A. D. Kepner, Y. Z. Hu, S. W. Koch, N. Peyghambarian, C.-Y. Li, T. Takada, Y. Kao, and J. D. Mackenzie, Appl. Phys. Lett. **64**, 1 (1994).
[4] H. Giessen, U. Woggon, B. D. Fluegel, G. Mohs, Y. Z. Hu, S. W. Koch, and N. Peyghambarian, Proceedings of the Non-Linear Optics, Hawaii, 1994, paper PD3.
[5] Y. Masumoto, T. Kawamura, and K. Era, Appl. Phys. Lett. **62**, 225 (1993).
[6] F. Henneberger and J. Puls, in *Optics of Semiconductor Nanostructures* (Akademie, Berlin, 1993), Sec. IV.3.
[7] V. S. Dneprovskii, V. I. Klimov, D. K. Okorokov, and Y. V. Vandyshev, Phys. Status Solidi B **173**, 405 (1992).
[8] Y. Z. Hu and S. W. Koch, Phys. Rev. B (to be published); see also Y. Z. Hu, S. W. Koch, M. Lindberg, N. Peyghambarian, E. L. Pollock, and F. F. Abraham, Phys. Rev. Lett. **64**, 1805 (1990).
[9] K. L. Shaklee, R. F. Nahory, and R. F. Leheny, J. Lumin. 7, 284 (1973).
[10] M. G. Bawendi, P. J. Carrol, W. L. Wilson, and L. E. Brus, J. Chem. Phys. **96**, 946 (1992).

Room-temperature gain at 1.3 μm in PbS-doped glasses

K. Wundke,[a) J. Auxier, A. Schülzgen, and N. Peyghambarian
Optical Sciences Center, University of Arizona, Tucson, Arizona 85721

N. F. Borrelli
Technology Group, Corning, Inc., Research and Development Center, Sullivan Park, Corning, New York 14831

We report on room-temperature optical gain at the ground exciton transition of PbS quantum-dot-doped glasses while optical pumping into the next-higher exciton resonance. The material gain in the quantum dots is as large as 80 cm^{-1}. The dot-size selective excitation provides tunability of the optical gain. This is demonstrated by tuning the gain from 1317 to 1352 nm by changing the pump wavelength from 900 to 980 nm. © *1999 American Institute of Physics.* [S0003-6951(99)00146-1]

A major advantage of semiconductor-doped glasses over epitaxially grown structures is that glass is an inexpensive and robust material. Recent improvements in the manufacture of quantum dots (QDs) embedded in glassy matrices have resulted in structures with more uniform-size distribution; fewer vacancies, substitutional defects, and dangling bonds; higher dot concentration; and reduced photodarkening. As in epitaxially grown QD structures, the three-dimensional quantum-confinement effects in the incorporated semiconductor QDs allow for tailoring the linear and nonlinear optical properties of these materials. Thus, semiconductor quantum-dot-doped glasses are very promising candidate materials for photonics applications and may have niche applications relative to the complicated and expensive epitaxially grown structures.

In this letter, we report on room-temperature optical gain in PbS quantum-dot-doped glasses in the communication-wavelength region. When pumping into the first-excited exciton transition, optical gain is observed in the vicinity of the ground exciton resonance. We demonstrate that the spectral position of the peak gain can be changed from 1317 to 1352 nm by tuning the pump wavelength between 900 and 980 nm, a wavelength range which is accessible with InGaAs laser diodes. This tunability relies on the strong carrier confinement and the inhomogeneous broadening in the sample due to dot-size fluctuations, whereas the actual spectral width and position of the gain is given by the pump pulse.

In our experiments, we used PbS quantum-dot-doped glasses which were fabricated by a thermal treatment of an oxide molten glass.[1] In this method, the subsequent thermal treatment of the melted glasses precipitates the microcrystalline phase. PbS quantum-dot-doped glasses exhibit strong three-dimensional quantum-confinement effects at moderate nanocrystal size because of the large bulk exciton Bohr radius of $a_B \approx 18$ nm. This, combined with the small band-gap energy of 0.41 eV (room temperature) of PbS, allows for tuning the ground exciton absorption from the visible to 3 μm. Figure 1(a) shows the room-temperature absorption spectra of PbS-doped glasses fabricated with different ther-

mal treatment schedules, which result in different average dot sizes. The strong quantum confinement in these structures is clearly observed in the large blueshift of the $1s$-absorption resonance with decreasing dot size. The appearance of defined subbanded peaks in all absorption spectra demonstrate the high quality of our samples and the relatively small size distribution of the PbS QDs. The average radii R of the QDs are deduced from fitting the spectral positions of the lowest-energy absorption peaks, which have been determined from the first derivative of the absorption spectra shown in Fig. 1(a), to the calculated $1s$-transition energies.[2] Here, we used the analytical hyperbolic band (HB) model,[3] which phenomenologically includes the nonparabolicity of the band structure and provides very good estimates for the $1s$-transition energies. Figure 1(b) compares the calculated dot-size-dependent energies of the $1s$ and $1p$ transition with the measured absorption maxima. As we can see, when the HB model is used to fit the $1s$-transition energy, the $1p$-transition energy is slightly underestimated.

To investigate the dynamics of the nonlinear absorption, we performed two-color pump–probe experiments. In these experiments, we used orthogonally polarized 130 fs pulses which are independently tunable in frequency. Pump and probe pulses are obtained from two optical parametric amplifiers, which are synchronously pumped by one regenerative Ti:sapphire amplifier at a repitition rate of 1 kHz. The zero time delay and the time resolution are given by the cross
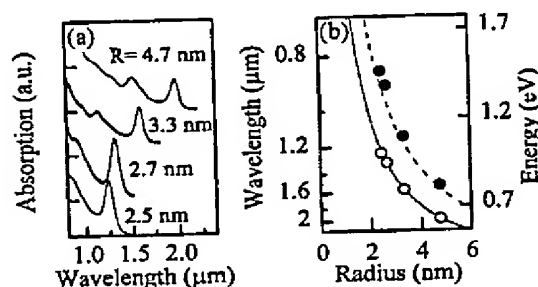

FIG. 1. (a) Room-temperature absorption spectra of PbS quantum-dot-doped glasses with different dot radii R. (b) Calculated $1s$- (solid line) and $1p$-transition (dashed line) energies; open (filled) circles; position of first (second) absorption peaks in (a).

[a)]Electronic mail: wundke@u.arizona.edu

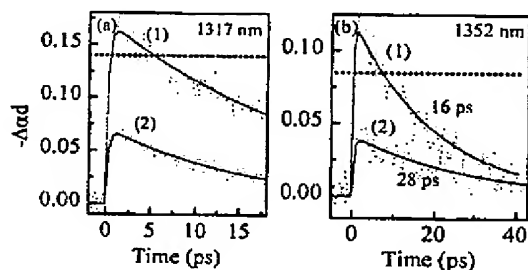Appl. Phys. Lett., Vol. 75, No. 20, 15 November 1999

Wundke et al.   3061

FIG. 2. Dynamics of the nonlinear absorption for the sample with R = 2.7 nm, (a) probe at 1317 nm, which is at the $1s$-absorption peak, with a pump fluence of 4 mJ/cm^2 and pumping at 900 nm (1), which is at the $1p$-absorption peak, or pumping at 980 nm (2), which is on the low-energy side of the $1p$-absorption peak [see Fig. 3(a)]; (b) probe at 1352 nm and pump at 980 nm with pump fluences of 4 mJ/cm^2 (1) or 2 mJ/cm^2 (2). No gain is observed for probing at 1352 nm and pumping at 900 nm; the linear absorption is marked by the dotted horizontal lines.
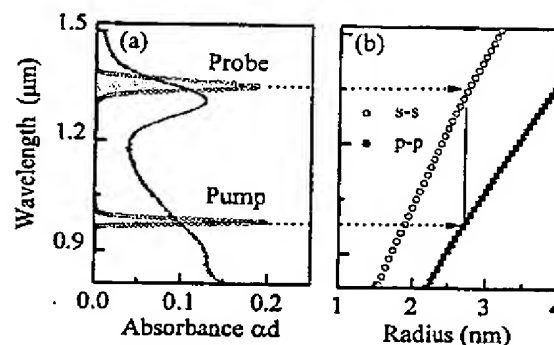

FIG. 3. (a) Absorption spectrum of the sample with R = 2.7 nm and pump and probe pulses of Fig. 2(b). (b) Calculated $1s$- (open circles) and $1p$-transition (full squares) energies; the arrows mark the positions of pump and probe pulses as shown in (a).

correlation of both pulses, which has been measured to 200 fs. To minimize the fluctuation in the detected signal due to the laser-intensity noise, we utilized a dual-beam setup for the probe beam: one invariant reference path and one signal path that contains the sample. The signals of both (probe) beams are then detected with an autobalanced photoreceiver (Nirvana, New Focus), which cancels out signals that are common to both channels. With this technique, we are able to detect small transmission changes; however, the spectral resolution is limited by the pulse spectral width due to the spectral-integrated detection.

In the following, we concentrate on results obtained at the sample with an average dot radius of 2.7 nm. Figure 2 shows the dynamics of the nonlinear absorption for two different probe wavelengths: (a) resonant with and (b) 35 nm below the maximum of the $1s$-absorption peak. In Fig. 2(a) the pump wavelength is tuned and set either to the maximum of the $1p$-absorption resonance [curve (1)] or 80 nm below this maximum [curve (2)]. Fig. 2(b) shows the bleaching dynamics for two different pump intensities, whereas the pump wavelength is fixed at 80 nm below the maximum of the $1p$-absorption peak.

The dynamics of the bleaching signal can be fitted using a simple asymmetric response function with exponential rise and decay times (solid lines). All transients shown in Fig. 2 exhibit the same ultrafast rise time of about 300 fs, which is only slightly above the time resolution of our experiments. The recovery dynamics of the bleaching signal changes with the pump fluence, i.e., the decay time decreases with increasing pump fluence from 28 to 16 ps. The dotted horizontal lines in Fig. 2 mark the value of the linear absorption $\alpha_0 d$ at the respective probe wavelength.

The sub-ps buildup of the bleaching signal is consistent with previous observations of the ultrafast $1s$ dynamics in glass samples[4–6] and indicates that the phonon bottleneck[7] is not effective in this system. Note the large excess energy of the excited carriers, which varies with the pump–probe detuning between approximately 12 and 16 LO-phonon energies.[8] Different mechanisms have been proposed to overcome the phonon bottleneck.[9–12] Klimov and McBranch[4] showed that in a glass sample, the observed short rise time can be explained in terms of an Auger-like mechanism,[12] which involves confinement-enhanced energy

transfer of the electron excess energy to a hole, with subsequent fast relaxation through its dense spectrum of states. The observed ps decay of the bleaching signal agrees well with the excitonic lifetime observed in various quantum-dot glass samples.[6,13–16] The origin of this fast and pump-fluence-dependent decay of the excitonic population has been discussed either in terms of carrier trapping effects,[14–16] i.e., at surface located defects, or Auger recombination.[17–19]

Optical gain is observed when the negative nonlinear absorption exceeds the linear absorption (dotted horizontal lines in Fig. 2). The buildup time of the gain, as seen in each curve (1) in Figs. 2(a) and 2(b), is about 500 fs and the gain lasts for 5–6 ps. The maximum gain value is $gd = -(\alpha_0 + \Delta\alpha) d \approx 0.022$, which corresponds to 15% (a) and 28% (b) of the linear absorption. From the measured optical gain and the filling factor (0.15%) of the QDs in the glassy material, we estimate a material gain in the QDs of 80 cm^{-1}. This room-temperature material gain is large compared to earlier results of 33 cm^{-1} obtained by Butty et al.[20] in sol–gel-derived CdS QDs. The significant enhancement of the optical gain can be attributed to the stronger three-dimensional quantum confinement in our samples, which is expected to enhance the optical nonlinearities.[21] The difference in the quantum confinement can be seen if we compare the normalized dot radius $R/a_B = 1.3$ for the sample used in Ref. 20 to $R/a_B = 0.15$ in the PbS quantum-dot-doped glass used in the experiments presented here.

In Fig. 3, we illustrate the spectral dependence of the optical gain. Here, the spectral positions of the pump and probe pulses, as used in the experiments of Fig. 2(b), are compared to the linear absorption of the sample [Fig. 3(a)] and the calculated $1s-1p$ splitting [Fig. 3(b)]. When pumping into the $1p$-absorption resonance, optical gain is found only when the pump–probe detuning is close or equal to the $1s-1p$ splitting for a given dot size. More explicitly, gain is found only for pumping at 900 nm and probing at 1317 nm [see curve (1) of Fig. 2(a)] or for pumping at 980 nm and probing at 1352 nm [see curve (1) of Fig. 2(b)]. However, no gain is observed for pumping at 980 nm and probing at 1317 nm [see curve (2) of Fig. 2(a)] or for pumping at 900 nm and probing at 1352 nm. Since in our experiments, the inhomogeneous broadening of the $1p$ absorption is large compared to the spectral width of the pump pulse, the pump pulse only excites a small portion of all QDs for which the pump pulse

is resonant with the $1p$ transition. Optical gain is only possible in this subset of pump-pulse-selected QDs and will appear around the transition frequencies between the lowest confined electron and hole levels after relaxation of the excited electron–hole pairs to the exciton ground state. In this case, taking into account our dot-size-selective excitation, as the mismatch between the $1s-1p$ splitting and the pump–probe detuning increases, the ratio between gain from the excited QDs and absorption from the nonexcited QDs decreases. Consequently, the effective optical gain disappears if this mismatch is too large, as demonstrated in curve (2) in Fig. 2(a). Here, the detuning of the probe pulse from the maximum gain position is about 35 nm, which corresponds to the initial spectral distribution of the excited carriers given by the pump pulse.

So far, we neglected the Coulomb and spin-orbit interactions, which change the selection rules and, therefore, increase the number of dipole-allowed transitions.[22] These additional transitions give rise to optical gain at new frequencies. For example, Hu et al.[23] used a microscopic model to describe optical gain observed in CdS and CdSe QDs.[20,24] Here, the gain was spectrally broad and located on the low-energy side of the ground exciton absorption. This was explained by taking into account one and two electron–hole pair recombination, i.e., excitons and biexcitons. On the basis of these results, we would expect maximum gain at a pump–probe detuning slightly larger than the $1s-1p$ splitting when pumping into the $1p$ transition. Our limited spectral resolution and accuracy of the HB model to calculate the $1p$-transition energies does not allow a final conclusion whether or not a shift or increased gain bandwidth due to the biexcitonic contributions is present. Furthermore, our pronounced dot-size-dependent selective excitation prohibits a direct comparison of our experimental results and the earlier experiments on CdS and CdSe QDs.

In summary, PbS quantum-dot-doped glasses show room-temperature gain of 80 cm^{-1} in the communication wavelength region around 1.3 μm. We have shown that we can utilize the strong quantum-confinement effect and the inhomogeneous broadening due to dot-size fluctuations to tune the gain spectrum of an individual PbS-doped glass. Furthermore, because the exciton ground-state transitions, where the gain is observed, can be widely tuned by changing the size of the QDs, we believe that room-temperature optical gain in PbS quantum-dot-doped glasses is possible over a wide spectral range. This gain tunability together with the demonstrated possibility of optical pumping at the wavelength of commercially available laser diodes shows that PbS quantum-dot-doped glasses may be suitable low-cost alternatives to current amplifiers and lasers for optical communication applications.

[1] N. F. Borrelli and D. W. Smith, J. Non-Cryst. Solids 180, 25 (1994).
[2] We use the notation $1s$ and $1p$ for the first two energy transitions, which are dipole-allowed interband transitions in the absence of Coulomb interaction ($\Delta l = 0$).
[3] Y. Wang, A. Suna, W. Mahler, and R. Kasowski, J. Chem. Phys. 87, 7315 (1987).
[4] V. I. Klimov and D. W. McBranch, Phys. Rev. Lett. 80, 4028 (1998).
[5] U. Woggon, H. Giessen, F. Gindele, O. Wind, B. Fluegel, and N. Peyghambarian, Phys. Rev. B 54, 17681 (1996).
[6] K. Shum, W. B. Wang, R. R. Alfano, and K. M. Jones, Phys. Rev. Lett. 68, 3904 (1992).
[7] U. Bockelmann and G. Bastard, Phys. Rev. B 42, 8947 (1990).
[8] T. D. Krauss and F. W. Wise, Phys. Rev. Lett. 79, 5102 (1997).
[9] T. S. Sosnowski, T. B. Norris, H. Jiang, J. Shing, K. Kamath, and P. Bhattacharya, Phys. Rev. B 57, R9423 (1998).
[10] P. C. Sercel, Phys. Rev. B 51, 14532 (1995).
[11] U. Bockelmann and T. Egler, Phys. Rev. B 46, 15574 (1992).
[12] Al. L. Efros, V. A. Kharchenko, and M. Rosen, Solid State Commun. 93, 281 (1995).
[13] J. Warnock and D. D. Awschalom, Phys. Rev. B 32, 5529 (1985); Appl. Phys. Lett. 48, 425 (1986).
[14] T. Inokuma, T. Arai, and M. Ishikawa, Phys. Rev. B 42, 11093 (1990).
[15] V. I. Klimov, P. Haring Bolivar, and H. Kurz, Phys. Rev. B 53, 1463 (1996).
[16] M. Tomita and M. Matsuoka, J. Opt. Soc. Am. B 7, 1198 (1990); J. Puls, V. Jungnickel, F. Henneberger, and A. Schülzgen, J. Cryst. Growth 138, 1005 (1994).
[17] N. P. Ernsting, M. Kaschke, H. Weller, and L. Katsikas, J. Opt. Soc. Am. B 7, 1630 (1990).
[18] J. Z. Zhang, R. H. O'Neill, and T. W. Roberti, Appl. Phys. Lett. 64, 1989 (1994).
[19] V. S. Dneprovskii, Al. L. Efros, A. I. Ekimov, V. I. Klimov, I. A. Kudriavtsev, and M. G. Novikov, Solid State Commun. 74, 555 (1990); M. Ghanassi, M. C. Schanne-Klein, F. Hache, A. I. Ekimov, D. Richard, and C. Flytzanis, Appl. Phys. Lett. 62, 78 (1993).
[20] J. Butty, N. Peyghambarian, Y. H. Kao, and J. D. Mackenzie, Appl. Phys. Lett. 69, 3224 (1996).
[21] E. Hanamura, Phys. Rev. B 37, 1273 (1988).
[22] Y. Z. Hu, M. Lindberg, and S. W. Koch, Phys. Rev. B 42, 1713 (1990); Y. Z. Hu, S. W. Koch, M. Lindberg, N. Peyghambarian, E. L. Pollock, and F. F. Abraham, Phys. Rev. Lett. 64, 1805 (1990); S. Nomura and T. Kobayashi, Phys. Rev. B 45, 1305 (1993), and references therein.
[23] Y. Z. Hu, H. Giessen, N. Peyghambarian, and S. W. Koch, Phys. Rev. B 53, 4814 (1996); Y. Z. Hu, S. W. Koch, and N. Peyghambarian, J. Lumin. 70, 185 (1996).
[24] J. Butty, Y. Z. Hu, N. Peyghambarian, Y. H. Kao, and J. D. Mackenzie, Appl. Phys. Lett. 67, 2672 (1995); H. Giessen, U. Woggon, B. Fluegel, G. Mohs, Y. Z. Hu, S. W. Koch, and N. Peyghambarian, Opt. Lett. 21, 1043 (1996); Chem. Phys. 210, 71 (1996).

Fabrication of germanium-coated nickel hollow waveguides for infrared transmission

Mitsunobu Miyagi, Akihito Hongo, Yoshizo Aizawa, and Shojiro Kawakami

Research Institute of Electrical Communication, Tohoku University, Sendai, 980 Japan

Circular hollow nickel waveguides with an inner germanium layer are fabricated by using a method based on rf sputtering, plating, and etching techniques. Transmission losses less than 0.5 dB are achieved including launching losses for straight waveguides with 1.5 mmϕ × 1 m at 10.6-μm wavelength. Bending losses of the waveguides are also examined.

PACS numbers: 42.80.Lt, 42.60.Kg, 84.40.Ts, 84.40.Vt

Realization of flexible waveguides for CO_2 laser light becomes an important subject in industrial and medical applications. From the viewpoint of power handling capability, hollow-core waveguides seem to be suitable for practical use[1] and several kinds of hollow waveguides are proposed and fabricated such as so-called flexible-infrared transmissive waveguides,[1,2] helical-circular waveguides,[3] circular metallic waveguides,[4] dielectric-coated metallic waveguides,[5,6] and hollow glass waveguides.[7] Among the various hollow-core waveguides, the dielectric-coated metallic waveguide which we proposed can transmit the HE_{11} mode with low loss and high launching efficiency from commercially available CO_2 lasers and its transmission characteristics are fully analyzed in slab[5,8,9] and circular waveguides.[5,10,11] In this letter we report the first fabrication of the dielectric-coated metallic waveguides with relatively small transmission losses.

To fabricate the dielectric-coated metallic waveguides, two points were the main concern. One is the adhesion between the metal and dielectrics, and another is to form waveguides efficiently. In order to solve these problems, we developed a method based on rf sputtering, plating, and etching techniques as schematically shown in Fig. 1. As first trial, we select germanium as a transparent dielectric at 10.6-μm wavelength. Nickel is chosen as a metal because its plating techniques are well established[12] and also the thickness of several hundred microns of metal which makes waveguides mechanically strong can be obtained by plating. These two materials are also preferable because they are free from toxicity in our fabrication process of waveguides.
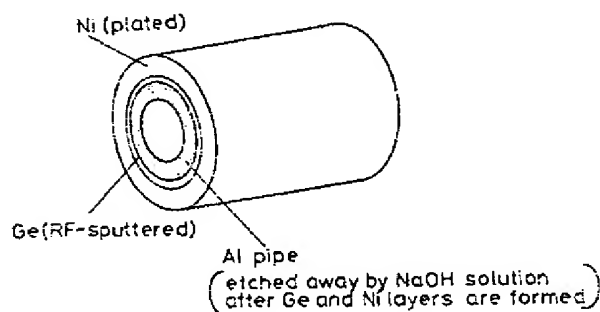
First, germanium is sputtered on a polished aluminum pipe (outer diameter of 1.5 mm, thickness of 0.2 mm, and length of 1.2 m) which is rotated with 10 rpm and moved axially with 10 cm/min in a vacuum chamber (2.0×10^{-2} Torr of argon gas) to obtain a uniform thin layer. Schematic view of the sputtering apparatus is shown in Fig. 2. Sputtered germanium on the aluminum pipe is observed to be amorphous according to the x-ray analysis, although an original material is single crystal. The sputtering rate is around 0.15 μm/h for 500-W rf power. A typical thickness of the germanium layer d is designed to be 0.45 μm so as to satisfy the minimum loss condition[10,11]:

$$(a^2 - 1)^{1/2}k_0 d = \pm \tan^{-1}\left(\frac{a}{(a^2 - 1)^{1/4}}\right) + s\pi,$$

where k_0 is the wave number in free space, a is the refractive index of the dielectric, i.e., 4.0 for germanium, and s is the integer.

In order to form a metallic pipe, nickel is directly plated onto the germanium layer. An anode of a nickel plate is formed to a circular cylinder whose diameter is 7.5 cm and length is 1.2 m and a cathode for plating is located at its center to form nickel uniformly. The plating bath is composed of $NiSo_4$ $6H_2O$ (240 g), $NiCl_2$ $6H_2O$ (45 g), and H_3BO_4 (30 g) in water of 1000 cm^3 in ratio. Although the pH changes from 1.3 to 3.7 during plating of several pieces of waveguides, a nickel layer of 70–200 μm is formed with sufficient mechanical strength. The current is 50 mA at an early stage of plating to form a pipe with a smooth surface and is gradually increased up to 2 A to form a pipe efficiently. Finally, the aluminum pipe is etched away by 10–20% NaOH solution and a circular hollow nickel waveguide with an inner germa-
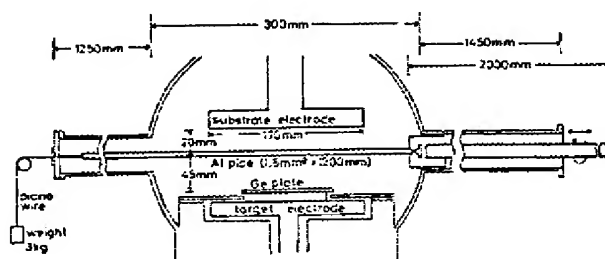

FIG. 1. Schematic method to fabricate germanium-coated nickel waveguides.

FIG. 2. Schematic view of the sputtering apparatus to form a germanium layer.
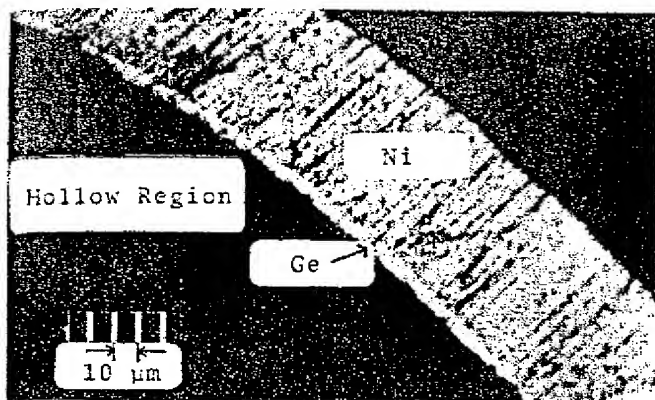
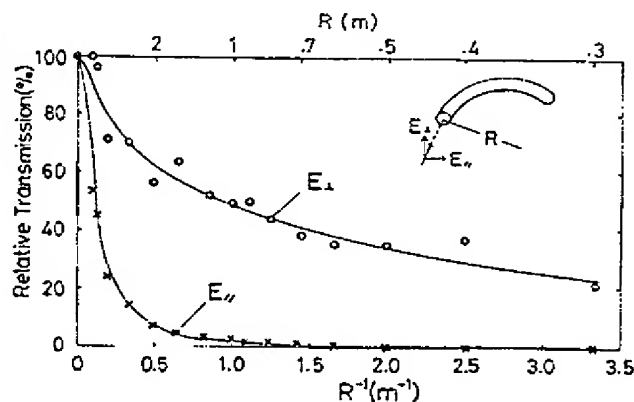FIG. 3. Cross-sectional view of a germanium-coated nickel waveguide.

FIG. 4. Bending losses of a nickel hollow waveguide with 1.5-mm diameter and 1.02-m-long whose straight-waveguide loss is 2.85 dB.

nium layer is fabricated. The cross-sectional view of the waveguide is shown in Fig. 3, where the germanium layer is made rather thick to show the adhesion between the nickel and germanium layers.

Several germanium-coated nickel waveguides are fabricated. Total transmission losses and polarization properties of the straight waveguides are measured and summarized in Table I as well as those of various hollow waveguides at 10.6 μm for comparison. Excitation of waveguides is conducted through a 20-cm-long waveguide with the same diameter of the test one by focusing a laser beam with a ZnSe lens ($f = 127$ mm). The diverging angle of the output beam from waveguides is around 16–21 mrad depending on waveguides, which shows that several higher order modes propagate, for the theoretical one of the HE_{11} mode is 10.8 mrad. It is seen that the losses of metallic waveguides can be reduced significantly by coating a dielectric material. Even when the laser beam is directly focused to the germanium-coated nickel waveguides, total transmission losses including launching losses increase by only 0.05 dB and never exceed 0.5 dB for 1-m-long waveguides. By connecting two waveguides carefully, total loss of 1 dB is achieved for 2-m-long waveguide. This

fact suggests that a waveguide with length of several meters can be realized by using the present fabrication techniques and equipment. Although a theory[10,11] predicts that the power loss of the HE_{11} mode is 3.2×10^{-2} dB/m, the difference between theoretical and present experimental results may be caused by roughness or gradual deformation of the waveguides and deviation of the thickness of the germanium layer from the optimum one which is not completely controlled at present.

Bending losses of nickel waveguides without and with an inner germanium layer are measured and shown in Figs. 4 and 5, where the first 20 cm is made straight and the rest of 80 cm of the waveguides is bent with a uniform curvature. When the polarization is parallel to the plane of curvature (denoted by $E_{\parallel}$), transmission is extremely small for the nickel waveguide even for large bending radii, whereas large improvement is done for the germanium-coated waveguide as well as when the polarization is perpendicular. If the dielectric-coated waveguides with smaller losses are realized in straight structures, the waveguides can be much sharply bent without significant loss increase.

TABLE I. Transmission properties of various hollow straight waveguides. Waveguides denoted by * are commercially available. Others are fabricated by the techniques presented in this paper.

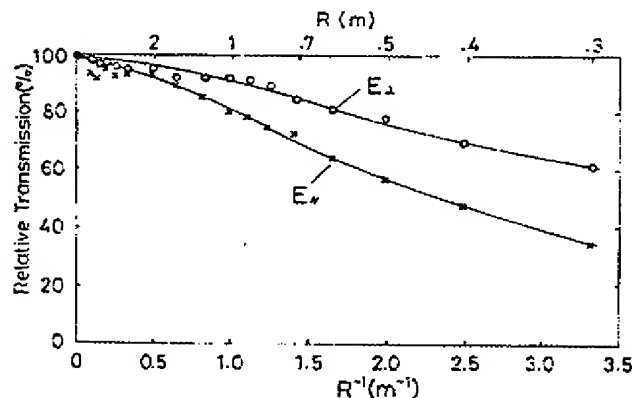| Hollow waveguides	Dimensions (mm$\phi \times$ m)	Total loss (dB)	Degree of polarization (%)
Pyrex glass	1.5×1.01*	1.22	99.1
Teflon	1.6×1.01*	4.42	99.1
Aluminum	1.6×1.01*	2.26	88.9
Nickel	1.6×1.01*	2.34	83.9
	1.5×1.02	2.85	81.7
Germanium-coated nickel	1.5×1.03	0.35	95.6
	1.5×1.01	0.40	98.2
	1.5×1.01	0.41	97.1
	1.5×1.01	0.43	93.2

FIG. 5. Bending losses of a germanium-coated nickel waveguide with 1.5-mm diameter and 1.01-m-long whose straight-waveguide loss is 0.43 dB.

[1] E. Garmire, T. McMahon, and M. Bass, Appl. Opt. 15, 145 (1976).

[2] E. Garmire, T. McMahon, and M. Bass, IEEE J. Quantum Electron. QE-16, 23 (1980).

[3] M. E. Marhic, L. I. Kwan, and M. Epstein, Appl. Phys. Lett. 33, 874 (1978).

[4] M. E. Marhic and E. Garmire, Appl. Phys. Lett. 38, 743 (1981).

[5] M. Miyagi, A. Hongo, and S. Kawakami, in Technical Digest, Institute of Electronics and Communication Engineers (IECE, Tokyo, 1981), paper OQE 80-128 (in Japanese).

[6] M. E. Marhic, Appl. Opt., 20, 3436 (1981).

[7] T. Hidaka, K. Kumada, J. Shimada, and T. Morikawa, J. Appl. Phys. 53, 5484 (1982).

[8] M. Miyagi and S. Kawakami, Appl. Opt. 24, 4221 (1981).

[9] M. Miyagi, A. Hongo, and S. Kawakami, IEEE J. Quantum Electron. QE-19, 136 (1983).

[10] M. Miyagi, Rec. Elect. Commun. Eng. Conv. Tohoku Univ. 51, 32 (1982) (in Japanese).

[11] M. Miyagi and S. Kawakami (unpublished).

[12] Handbook of Chemistry, edited by Chemical Society of Japan (Maruzen, Tokyo, Japan 1965), pp. 103–109 (in Japanese).

Transverse second-order mode oscillations in a twin-stripe laser with asymmetric injection currents

S. Mukai, H. Yajima, S. Uekusa,[a] and A. Sone[b]

Electrotechnical Laboratory, Sakura, Niihari, Ibaraki, Japan

Transverse second-order mode oscillations in asymmetrically pumped twin-stripe lasers are described. Both far-field patterns and near-field patterns have two peaks, and a stronger peak appears on the weakly pumped side. The dependence of light intensity in one peak of the far-field pattern on the current into one stripe shows threshold characteristics. On application of rectangular pulse to one stripe, switching from one peak to the other occurs within 5 ns.

PACS numbers: 42.55.Px, 42.80.Lt, 42.60.Da, 42.60.He

Asymmetric waveguide structures in semiconductor lasers cause asymmetry in far-field radiation patterns. Asymmetric far-field patterns were observed for lasers with a built-in asymmetric structure,[1] and were also observed for lasers with symmetric built-in structures using asymmetric distribution of injection currents.[2,3] The asymmetric far-field patterns were explained on the basis of Maxwell's equation for an asymmetric distribution of complex refractive indices.[1,2,4] However, investigations have so far been limited to transverse fundamental mode oscillations in an asymmetric waveguide, and very little is known about higher-order mode oscillations.[3] In the present letter, we report experimental results and some theoretical insight about transverse second-order mode oscillations in semiconductor lasers with asymmetric injection currents.

The device structure is similar to the one reported by Scifres et al.[2] The wafers were grown by liquid phase epitaxy and consisted of a Si-doped (2×10^{18} cm^{-3}) GaAs substrate, 2-μm-thick Te-doped (1×10^{17} cm^{-3}) Al$_{0.35}$Ga$_{0.65}$As layer, 0.2-μm-thick undoped active Al$_{0.05}$Ga$_{0.95}$As layer, 2-μm-thick Ge-doped (5×10^{16} cm^{-3}) Al$_{0.35}$Ga$_{0.65}$As layer, and 0.3-μm-thick Ge-doped (1×10^{19} cm^{-3}) GaAs. A 12-μm-wide mesa was formed by etching down to 0.5 μm above the active layer. After depositing a 0.1-μm-thick Si$_3$N$_4$ film, 2-μm-wide twin stripes on 8-μm centers was etched in the film

on the mesa. The p-side contacts were Cr and Au. The contact between the stripes were chemically etched. 200-μm-long chips were cleaved. They were pumped with 1-μs width rectangular pulses. The total threshold current was about 60
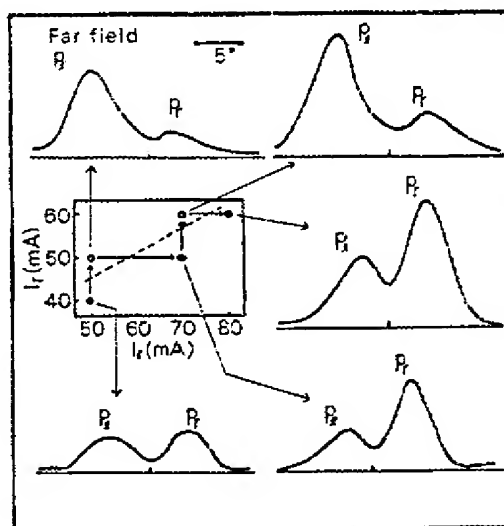

FIG. 1. Far-field patterns of a twin-stripe laser. I_l and I_r are currents injected into the left and right stripes. The inset shows currents at which the patterns were observed. Open circles mean that the left peak of the far-field pattern is higher than the right peak at these currents. Solid circles mean the opposite. The broken line approximately determines two current regions corresponding to the left peak (or right) peak being higher. The arrows connecting the circles show how the currents were varied.

[a] On leave from Department of Electrical Engineering, Meiji University, 1-1-1 Higashimita, Tama, Kawasaki, Japan.

[b] On leave from Hamamatsu Photonics Co., 1126-1 Ichinomachi, Hamamatsu, Japan.

A Review of IR Transmitting, Hollow Waveguides

JAMES A. HARRINGTON

Ceramic & Materials Engineering
Rutgers University
Piscataway, New Jersey, USA

Infrared (IR) transmitting hollow waveguides are an attractive alternative to solid-core IR fibers. Hollow guides are made from plastic, metal, or glass tubes that have highly reflective coatings deposited on the inside surface. These guides have losses as low as 0.1 dB / m at 10.6 μm and may be bent to radii less than 5 cm. For use in high-power laser delivery applications, the guides have been shown to be capable of transmitting up to 3 kW of CO_2 laser power. They are also finding uses in both temperature and chemical fiber sensor applications. This paper reviews the progress in hollow waveguide technology with emphasis on the best guides available today.

Keywords   IR fibers, hollow waveguides, laser power delivery, fiber sensors

Infrared (IR) optical fibers may be defined as fiber optics transmitting wavelengths greater than approximately 2 μm. The first IR fibers were fabricated in the mid 1960's from chalcogenide glasses such as arsenic trisulfide with losses in excess of 10 dB/m [1]. During the mid 1970's, the interest in developing an efficient and reliable IR fiber for short-haul applications increased partly in response to the need for a fiber to link broadband, long wavelength radiation to remote photodetectors in military sensor applications. In addition, there was an ever-increasing need for a flexible fiber delivery system for transmitting CO_2 laser radiation in surgical applications.

Around 1975, a variety of IR materials and fibers were developed to meet these needs. These included the heavy metal fluoride glass (HMFG) and polycrystalline fibers as well as hollow rectangular waveguides. While none of these fibers had physical properties even approaching that of conventional silica fibers, they were, nevertheless, useful in lengths less than 2–3 m for a variety of IR sensor and power delivery applications [2].

Infrared fiber optics may logically be divided into three broad categories: glass, crystalline, and hollow waveguides. These categories may be further subdivided, based on either the fiber material or structure or both, as shown in Table 1. Over the past 25 years, many novel IR fibers have been made in an effort to fabricate a fiber optic with properties as close to silica as possible, but only a relatively small number have survived. A good source of general information on these various IR fiber types may be found in the literature [3–6]. In this paper, the hollow waveguide technology will be reviewed only with emphasis on the best and most

J. A. Harrington

Table 1

Three main categories of IR fibers with examples of the most common type of fiber within the category of glass, crystalline, or hollow fibers

Main	Subcategory	Examples
Glass	Heavy metal fluoride (HMFG)	ZBLAN-(ZrF_4-BaF_2-LaF_3-AlF_3-NaF)
	Germanate	GeO_2-PbO
	Chalcogenide	As_2S_3 and AsGeTeSe
Crystal	Polycrystalline (PC)	AgBrCl
	Single crystal (SC)	Sapphire
Hollow waveguide	Metal/dielectric film	Hollow glass waveguide
	Refractive index < 1	Hollow sapphire at 10.6 μm

practical hollow waveguide candidates available today. In general, both the optical and mechanical properties of IR transmitting hollow waveguides remain inferior to silica fibers and, therefore, the use of hollow guides is still limited to nontelecommunication, short-haul applications requiring only a few meters of waveguide, rather than kilometer lengths common in telecommunication applications. The short-haul nature of these special IR fibers results from the fact that the guides have losses in the range of a few dB/m rather than a few dB/km. Also, hollow guides have an additional loss on bending, and they are also somewhat weaker than silica fiber. These deleterious features have slowed the acceptance of hollow guides and restricted their use today to applications in chemical sensing, thermometry, and laser power delivery.

Background

Hollow waveguides present an attractive alternative to other solid-core IR fibers [2]. Key features of hollow guides are their ability to transmit wavelengths well beyond 20 μm, their inherent advantage of having an air core for high-power laser delivery, and their relatively simple structure and potential low cost. Initially, these waveguides were developed for medical and industrial applications involving the delivery of CO_2 laser radiation, but more recently, they have been used to transmit incoherent light for broadband spectroscopic and radiometric applications [7, 8]. In general, hollow waveguides enjoy the advantages of high laser power thresholds, low insertion loss, no end reflection, ruggedness, and small beam divergence. Potential disadvantages, however, include an additional loss on bending and a small NA. Nevertheless, today they are one of the best alternatives for both chemical and temperature sensing as well as for power delivery in IR laser surgery or in industrial laser delivery systems with losses as low as 0.1 dB/m and transmitted cw laser powers as high as 2.7 kW [9].

Hollow-core waveguides may be grouped into two categories: 1) those whose inner core materials have refractive indices greater than one (leaky guides) and 2) those whose inner wall material has a refractive index less than one (attenuated total reflectance, i.e., guides). Leaky or $n > 1$ guides have metallic and dielectric films deposited on the inside of metallic, plastic, or glass tubing [10]. Attenuated
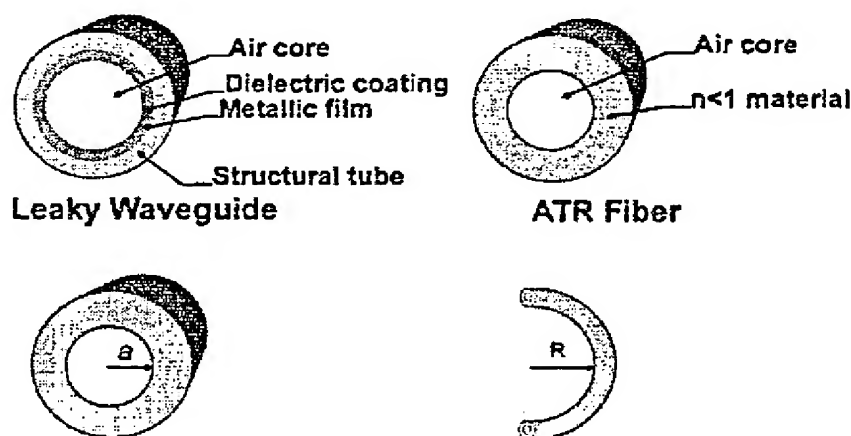
Figure 1. Structure of two types of hollow waveguides also showing the key parameters of bore and bending radius affecting the losses in hollow guides.

total reflectance guides are composed of dielectric materials with refractive indices less than one in the wavelength region of interest [11]. Therefore, $n < 1$ guides are fiberlike in that the core index ($n \approx 1$) is greater than the clad index. Hollow sapphire fibers operating at 10.6 μm ($n = 0.67$) are an example of this class of hollow guide [12]. The structure and key parameters for hollow guides are shown in Figure 1. In general, hollow structures with $n > 1$ have been made from metal, plastic, and glass tubes while the $n < 1$ or ATR guides are made of sapphire or some special $n < 1$ oxide glass.

The theory of hollow waveguide transmission has been described from the viewpoint of both wave and ray optics. Marcatili and Schmeltzer (MS) [13] have used a wave optic approach that predicts for either metallic or dielectric waveguides that $\alpha \sim 1/a^3$, where α is the attenuation coefficient and a is the bore radius. Bending the hollow waveguides increases the total loss. Recently, Miyagi et al. [14] have shown that the additional bending loss varies as $1/R$, where R is the bending radius. Therefore, we have in contrast to the solid-core fibers, a loss that depends strongly on the diameter and bending radius of the fiber. For the thin film waveguide structures, Miyagi and Kawakami [15] have shown that for dielectric coatings deposited over a metallic layer, the attenuation coefficient, is given by

$$\alpha_x = \left(\frac{U_o}{2\pi}\right)^2 \cdot \frac{\lambda^2}{a^3} \cdot \left(\frac{n}{n^2 + k^2}\right)_{metal} \cdot F_{film}, \qquad (1)$$

where α_x is the loss for a straight guide; U_o is a mode-dependent parameter that for the lowest order HE$_{11}$ mode equals 2.405; n and k in $(\ldots)_{metal}$ refer to the optical constants of metal film; and F_{film} is a term that accounts for the loss due to the dielectric film(s).

Metal-Tube Waveguides

Hollow core waveguides have been fabricated using a variety of techniques. Some of the methods include physical vapor deposition of silver and dielectric layers on metallic substrates [16], sputtering of metallic, dielectric, and semiconductor films
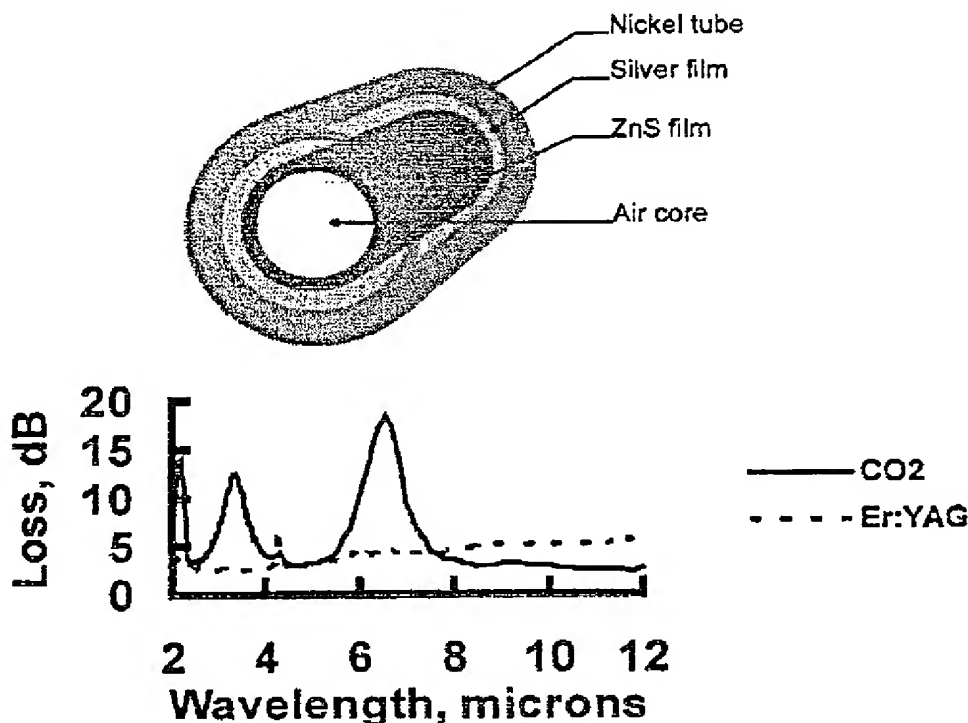
Figure 2. Structure and spectral losses for metallic waveguide fabricated by Miyagi's group at Tohoku University [22].

on a leachable mandrel followed by electroplating [17], and liquid phase formation of coatings inside plastic tubing [18], and glass tubing [19]. Most often the cross section of the guides is circular, but early work by Garmire et al. [20] and more recently by Kubo [21] on rectangular guides continues to be of interest. The advantage of the circular cross section is the ease of bending and the small overall size compared to rectangular or square cross section guides.

Professor Miyagi and his coworkers at Tohoku University [17] have pioneered the development of metallic waveguides based on a hollow nickel substrate. Their fabrication process involves three steps. In the first step, a pipe made typically of aluminum is placed in a sputtering chamber and a dielectric layer followed by a metallic film is deposited on the pipe. Next, the coated pipe is put into an electroplating tank, where a thick nickel layer is deposited on top of the sputtered layers. Finally, the pipe is etched away leaving the final structure shown in Figure 2.

In Figure 2, we also show a typical loss curve for one of their best dielectric coatings (ZnS) over silver. The data shown are for two 1000 μm-bore guides, one optimized for the 3 μm wavelength of the Er:YAG laser and the other optimized for the 10.6 μm wavelength of the CO_2 laser. The optimization for each wavelength results from adjusting the thickness of the thin-film dielectric coating. In Figure 3, bending losses for these hollow waveguides are given for both the CO_2 and Er:YAG laser wavelengths [22]. The losses are seen to be as low as 0.25 dB/m at 10.6 μm for light polarized perpendicular to the plane of bending, but slightly higher for parallel polarized light. This is as expected from waveguide theory or
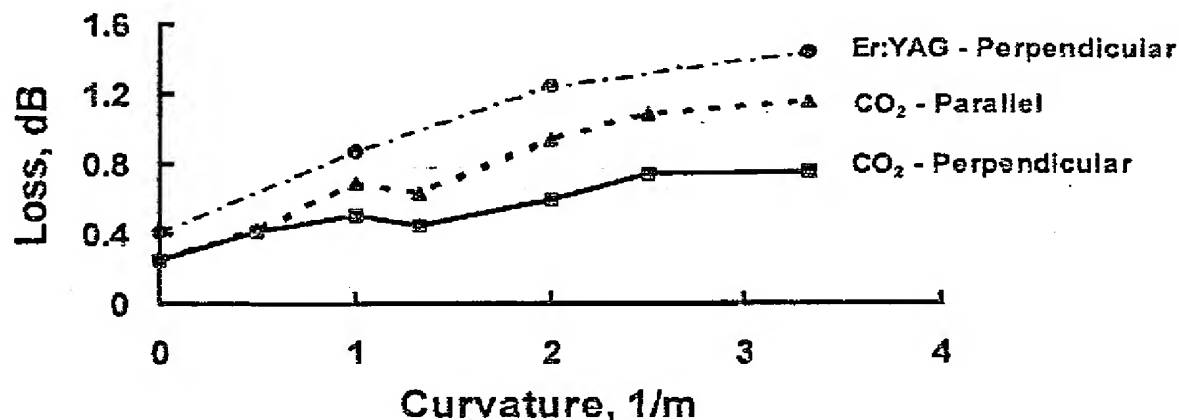
Figure 3. Losses for bent hollow metallic guides taken at both CO_2 and Er:YAG laser wavelengths [22].

from simple considerations based on Fresnel reflections from metal surfaces. The highest CO_2 laser power delivered using a 2000 μm bore metallic guide is over 3 kW [9]. Miyagi and his coworkers have also developed a hollow structure based on a square cross section [23]. To fabricate a square cross-section tube they have developed a process in which they first deposit, using evaporative techniques, thin-film coatings of ZnS, PbTe, and/or PbF_2 on phosphor bronze strips and then they solder four of these phosphor bronze metal strips together in a continuous process. The losses for these square guides are as low as 0.1 dB/m at 10.6 μm.

The waveguides developed by Morrow et al. [24] are constructed from a silver tube. Instead of depositing a metallic layer inside a hollow mandrel, they begin with an extruded silver tube and then deposit a silver halide film on the inside of the tube as shown in Figure 4. To ensure the lowest loss, Morrow et al. first etch the bore of the silver tubing to make it smooth. Then an AgBr film is applied on the inside using wet chemistry methods. The bending loss for a 1000 μm-bore tube, 1-m in length at 10.6 μm is also shown in Figure 4. It is noted from this data that the losses in the straight guide are quite low. Unfortunately, the guides tend to mix modes and, therefore, the beam output is rather multimode compared to the hollow glass or sapphire waveguides. This is due in large part to the rougher inner surface of the extruded tubing compared, for example, to the smooth inner surface of glass.

Luxar's approach is based on technology initially developed by Laakmann and her colleagues [16]. Their fabrication technique involves first depositing a silver film on a metal strip and then overcoating the silver with a thin film of PbF_2. The metal strip is then rolled and inserted into stainless steel hypodermic tubing as shown in Figure 5. The bending loss for one of their guides is also shown in Figure 5. This waveguide had a 750 μm bore, 1-m length and the losses shown are for 10.6 μm. Like the other hollow waveguides, the losses are quite low at CO_2 laser wavelengths. Furthermore, the $1/R$ behavior of the loss on bending is noted. This is, of course, characteristic of all hollow guides, but the magnitude of this loss depends largely on the quality of the inner surface. In general, these bending losses are tolerable for the radii normally encountered in practical applications.
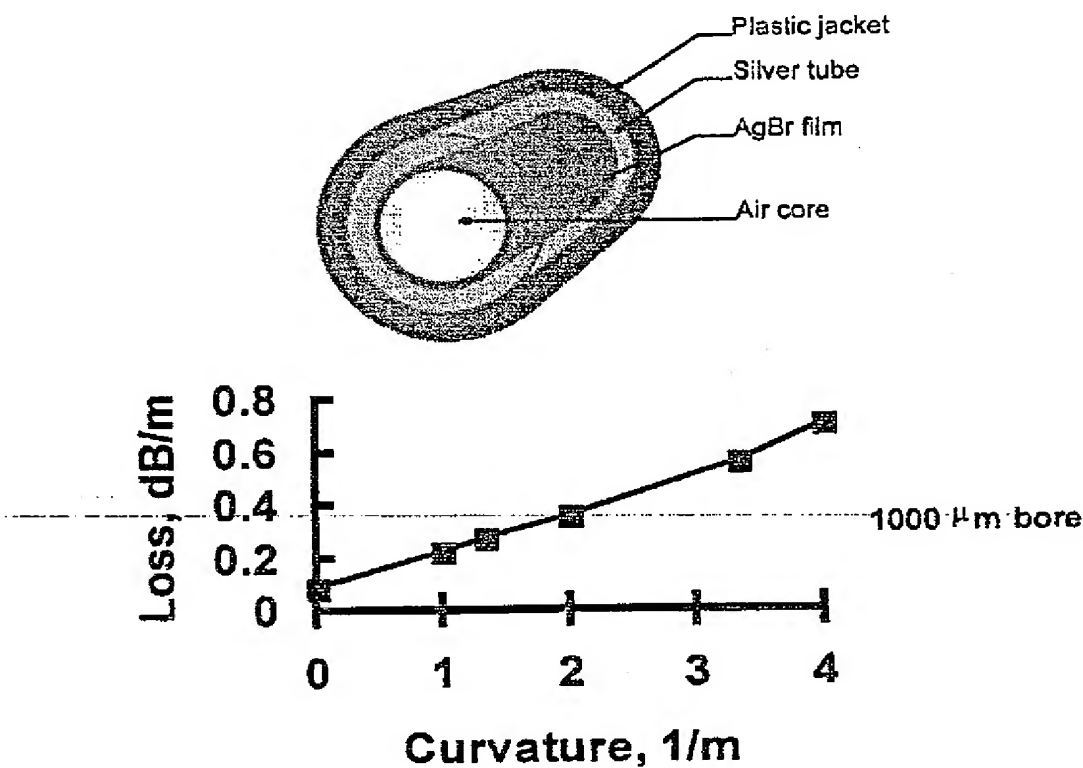
Figure 4. Structure and bending loss for hollow guide made from silver tubing with a AgBr film deposited on the inside surface [24].
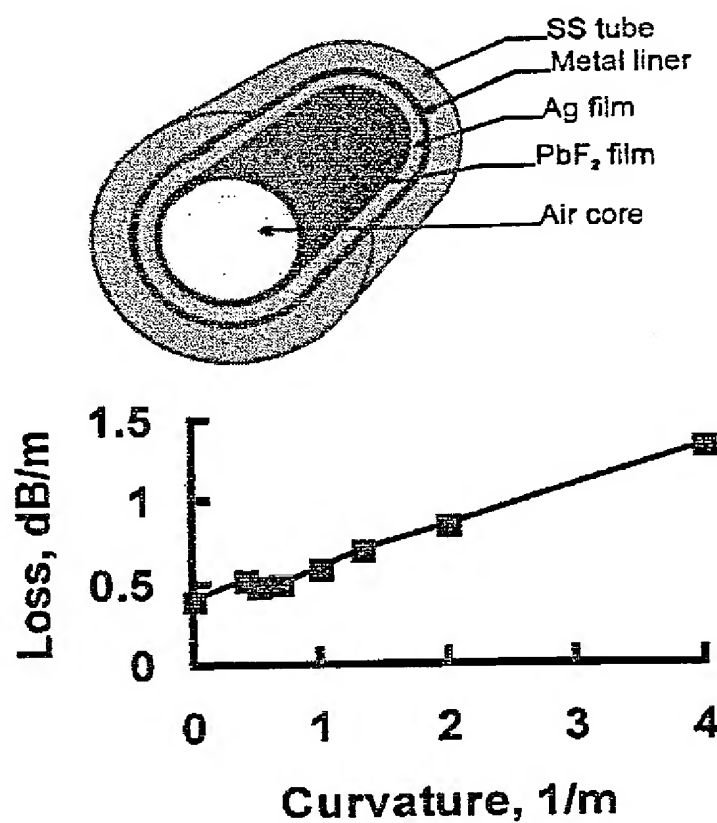

Figure 5. Structure and bending loss for hollow guides made by Luxar [16].

Plastic-Tube Waveguides

Hollow waveguides may also be formed on the inside of plastic tubing. This leads to a very flexible structure that is inexpensive to fabricate and durable enough that a reasonable laser power (safe limit < 25 W) can be transmitted through the guides. Croitoru's group at Tel Aviv University has pioneered the approach of first depositing a silver film on the inside of Teflon and polyethylene plastic tubing (see Figure 6) and then overcoating the silver film with a dielectric layer of AgI [18] using wet-chemistry techniques [25]. Initially, Croitoru used rather large bore tubing, but more recently guides with bore sizes of about 1000 μm have been fabricated. In Figure 6 the bending loss is shown for a 1000 μm bore tube measured at 10.6 μm. The losses are somewhat higher than those measured for the metallic tubes. This is primarily due to increased scattering losses resulting from the rougher inner surface of the plastic tubing. In an independent measurement, the author was able to transmit over 65 W of CO_2 laser power for several minutes through an 1850 μm bore guide.

Losses in the plastic waveguides made by Croitoru may be reduced if smoother polymer tubing is chosen. Haan and Harrington [26] have used similar wet-chemistry methods to deposit Ag/AgI films inside polycarbonate tubing. Extruded polycarbonate tubing in lengths of 2 m and bore sizes from 840 μm to 2 mm was used to make the guides. Figure 7 shows the lowest straight losses for several hollow waveguide structures—two polycarbonate waveguides, a Teflon waveguide,
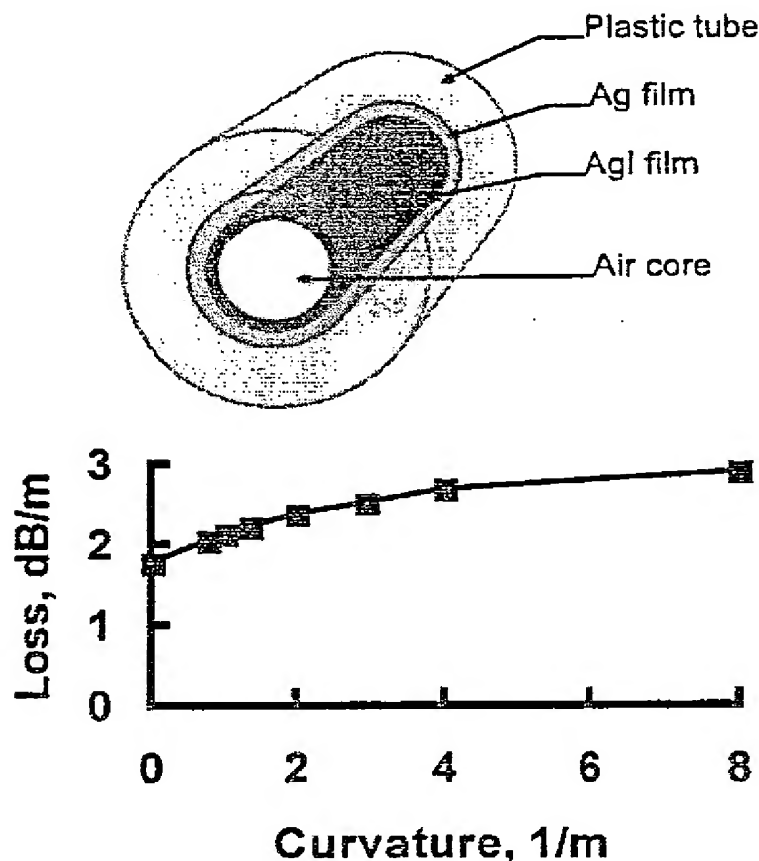

Figure 6. Structure and bending loss for hollow plastic waveguide made by Croitoru's group at Tel Aviv University [18].
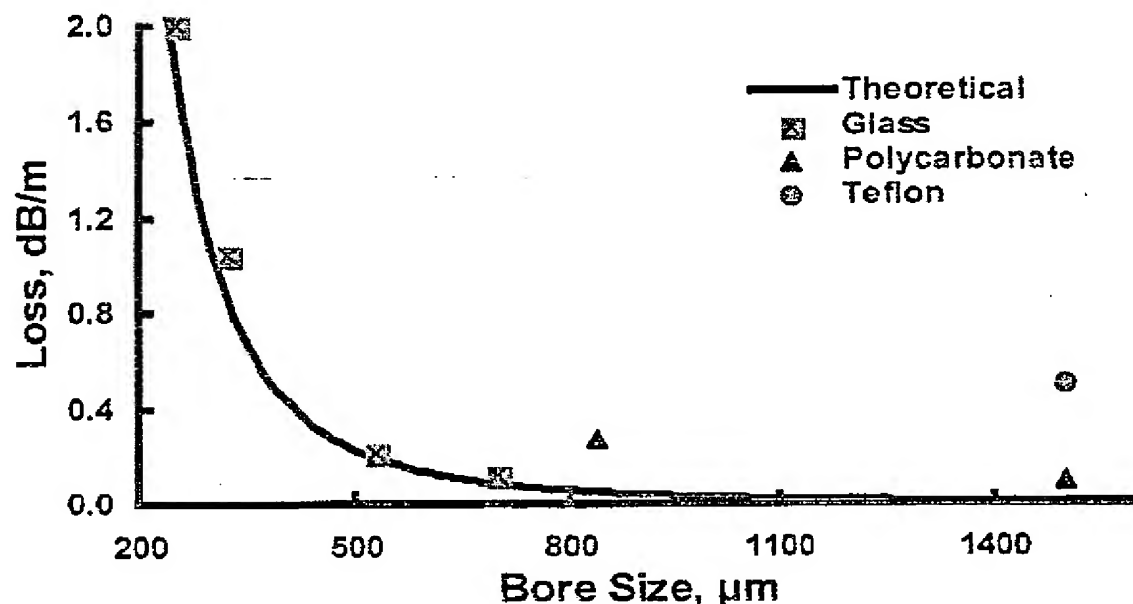
Figure 7. Composite data for hollow glass and plastic waveguides. Note the low loss at 10.6 μm for the glass guides in comparison to the plastic guides.

and hollow glass waveguides (see next section) measured using a CO_2 laser. The solid curve is calculated for the lowest order mode at 10.6 μm using Eq. 1. The attenuation values of 0.22 dB/m for an 840 μm PC guide and 0.10 dB/m for a 1500 μm PC guide show the improvement over the Teflon or polyethylene waveguides. In a simple power test using a CO_2 laser, the 1500 μm waveguide was able to withstand more than 25 W of incident laser power.

Hollow Glass Waveguides

One of the most popular hollow waveguides today is the hollow glass waveguide (HGW) developed by Harrington's group at Rutgers University. This hollow glass structure has the advantage over other hollow structures because it is simple in design, extremely flexible, and, most important, has a very smooth inner surface. Hollow glass waveguides have a metallic layer of Ag on the inside of silica glass tubing and then a dielectric layer of AgI over the metal film identical to that used to make the hollow plastic guides. Figure 8 shows a cross section of the structure of the HGWs. The fabrication of HGWs begins with silica tubing, which has a polymer (UV acrylate or polyimide) coating on the outside surface. A wet-chemistry technique (see Figure 9), similar to that used by Croitoru and his coworkers [18, 27] to deposit metal and dielectric layers on the inside of plastic tubing, is employed to first deposit a silver film using standard Ag plating technology [28]. Next, a very uniform dielectric layer of AgI is formed through an iodization process in which some of the Ag is converted to AgI [29]. Using these methods, HGWs with bore sizes ranging from 250 to 1000 μm and lengths as long as 13 m have been made.

The spectral response for HGWs depends critically on the thickness of the dielectric film. Generally, for the AgI films, the film thickness ranges from 0.2 to
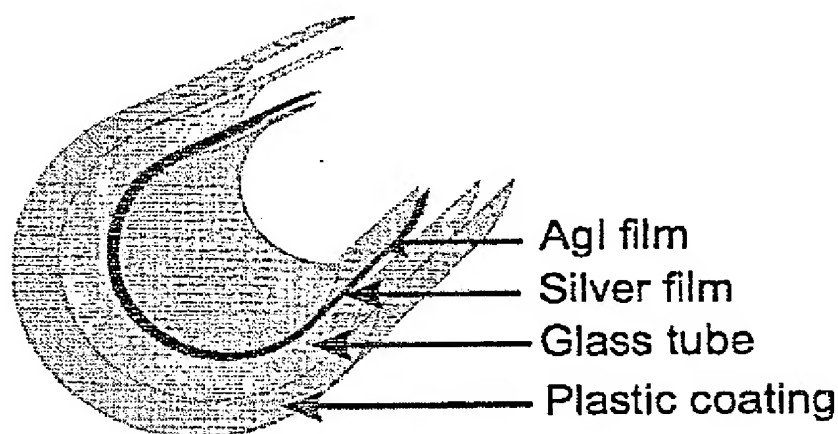
Figure 8. Structure of the HGWs showing the metallic and dielectric films deposited inside silica glass tubing.

0.8 μm. In Figure 10, we show the spectral response of two waveguides that have different thickness films deposited on the inside of a 700 μm bore silica tube, 1 m in length. The thickest film gives a minimum loss at 10.6 μm, while the thin film was selected for minimum loss near 3 μm. The latter guide has a fairly flat response beyond 3 μm and, therefore, this guide would be useful in broadband applications. The structure observed in the spectra is due to thin-film interference effects similar to that commonly observed in thin-film coatings on optical components. These effects have been observed and extensively discussed in the work of Matsuura et al. [30].
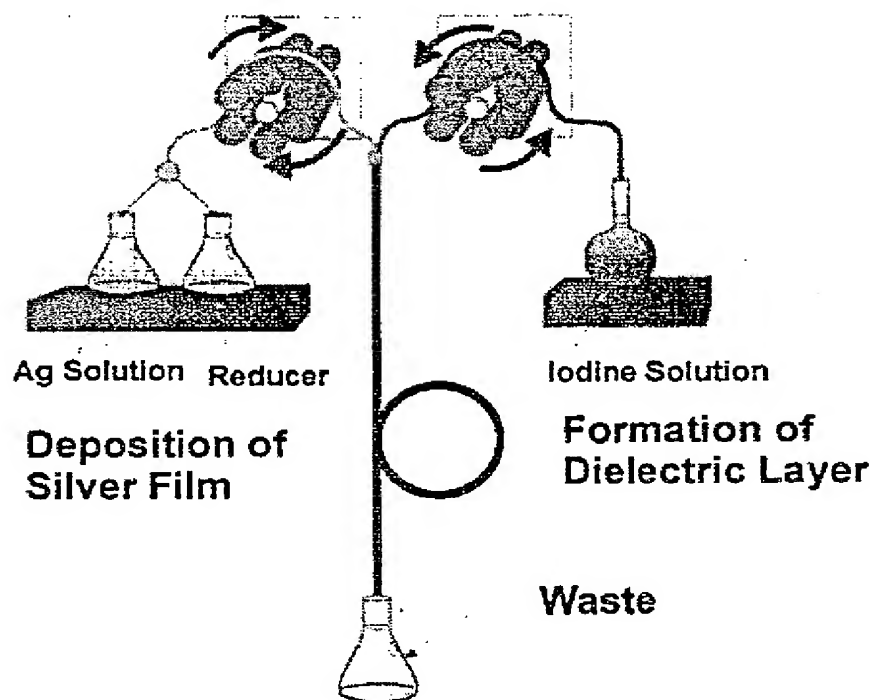

Figure 9. Schematic of the experimental set-up for depositing the Ag metallic and AgI dielectric films inside silica tubing to form the HGWs.
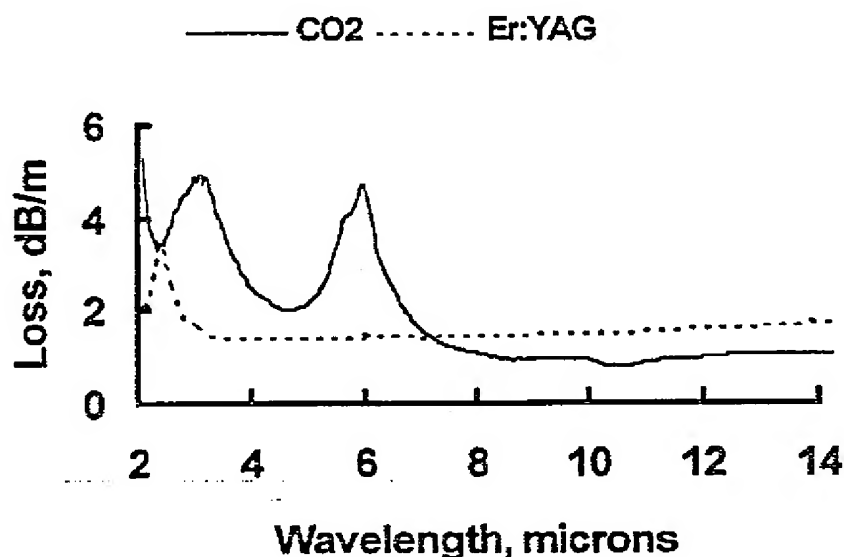
——— CO2 ······· Er:YAG

Figure 10. Spectral response of two HGWs—one designed for low loss at the CO_2 laser wavelength of 10.6 μm and the other for low loss at the Er:YAG laser wavelength of 2.94 μm.

The strong bore-size dependent loss for straight HGWs is shown for two guides in Figure 11 [28]. These data were taken using CO_2 and Er:YAG lasers and the guides were optimized for minimal loss at 10 and 3 μm, respectively. The solid curves are theoretical calculations of the losses for the lowest order HE_{11} mode. At the CO_2 laser wavelengths, one can see not only the strong $1/a^3$ dependence predicted by MS theory, but also that there is good agreement with the experimental results. However, at 3 μm the calculated losses are much lower than the measured values. This is a result of increased scattering losses at the shorter wavelengths and the multimode character of the Er:YAG laser.

Bending increases the loss in hollow waveguides beyond that shown for the straight loss seen in Figure 12. The additional bending loss varies as $1/R$ as
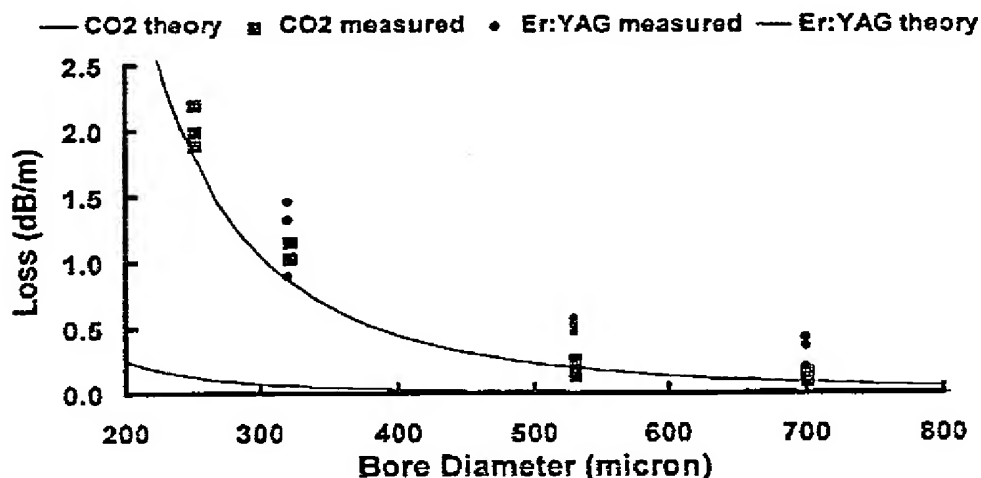
——CO2 theory   ■ CO2 measured   ● Er:YAG measured   ——Er:YAG theory

Figure 11. Measured losses for straight HGWs using CO_2 and Er:YAG lasers. Note that the predicted losses are well below the measured ones at 2.94 μm.
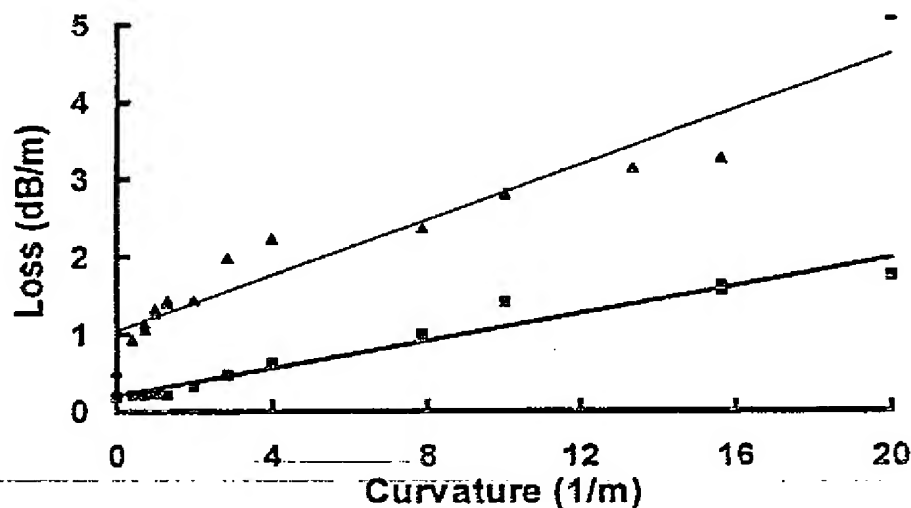
Figure 12. Bending losses for two 530-μm-bore HGWs measured at 10.6 (■) and 2.94 (▲) μm.

reflected in the data for two 530 μm bore guides in Figure 12. These data show the total loss for guides with a constant length of fiber under bending. A curvature of 20 represents a bend diameter of only 10 cm. This is sufficiently small for most applications.

Hollow $n < 1$ Waveguides

The idea of an $n < 1$ structure originated with Hidaka et al. in 1981 [31]. In this structure, the air core ($n = 1$) has a refractive index greater than the inner wall, cladding material, and, therefore, this type of waveguide is fiberlike in that $n_{clad} < n_{core}$. This is also referred to as an attenuated total reflectance (ATR) guide in contrast to the leaky structure of the $n > 1$ guides discussed above (see Figure 1). To be useful for laser transmission, the ATR guides must have the region of anomalous dispersion, where n is less than 1, fall within some useful laser wavelength range. The first $n < 1$ guides studied by Hidaka et al. [32] focused on glass tubes made from lead and germanium-doped silicates. By adding heavy ions to silica glass, he was able to shift the infrared edge to longer wavelengths so that the $n < 1$ region of anomalous dispersion occurred within the CO_2 laser wavelength band. Worrell [33] also studied $n < 1$ glasses, in particular, the germanate glasses. The losses in the hollow glass, $n < 1$ fibers, however, were very high due to a high k or extinction coefficient and this technology has largely been abandoned.

A more promising $n < 1$ structure is hollow sapphire. It was first pointed out by Harrington and Gregory [11] that sapphire or Al_2O_3 has $n < 1$ from 10 to 16.7 μm and, in addition, it has a very small k value of 0.05 at 10.6 μm. This means that the theoretical loss predicted by MS theory is very low (less than 0.1 dB/m for a 1,000-μm-bore tube) for this material. Single-crystal sapphire tubing is fabricated by Saphikon, Inc. in Milford, NH in bore sizes ranging from 250 to 1070 μm. In Figure 13 we show the measured straight losses for five different bore sizes. Also in Figure 13, the theoretical losses for both the lowest order HE_{11} and next higher order HE_{12} modes are plotted. The measured losses are somewhat higher than that predicted by MS theory as a result of the roughness of sapphire's inner wall.
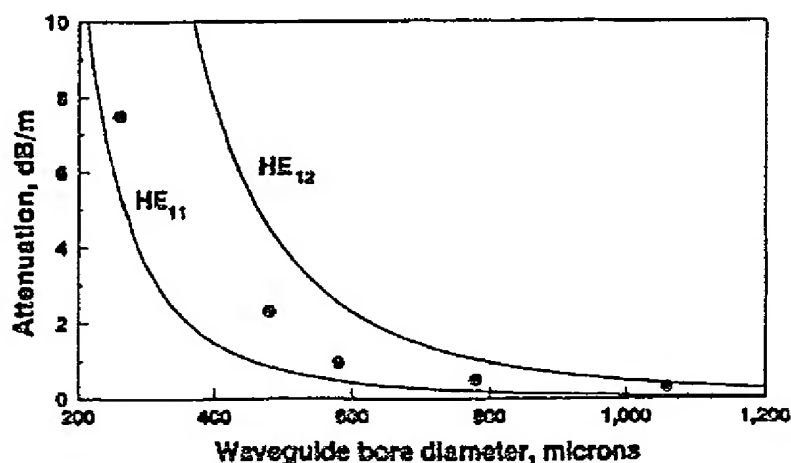
Figure 13. Measured loss at 10.6 μm for straight, hollow sapphire waveguides. Note that the losses fall between the theoretical losses for the HE_{11} and HE_{12} modes. This is a result of surface roughness of the sapphire tubing.

Gregory and Harrington [11] showed that the surface roughness of hollow sapphire accounted for the increased attenuation over that predicted by theory for the HE_{11} mode. Figure 14 shows the bending loss for the 530 μm bore tube. The curvature is not as great as it is for the HGWs, because sapphire has a high modulus and, therefore, cannot be bent to small diameters. Hollow sapphire delivery systems have been coupled to CO_2 lasers for use in gynecology and orthopedic surgery and they have been packaged in a water-cooled jacket for the delivery of over 1900 W of CO_2 laser power [34].

Laser Power Delivery in Hollow Glass Waveguides

Hollow waveguides are ideal for high power laser delivery because of the inherently high damage threshold of an air-core structure. For most medical and some low-power industrial applications, it is sufficient to be able to deliver up to 100 W of laser power. For these purposes, the HGWs can be used without cooling,
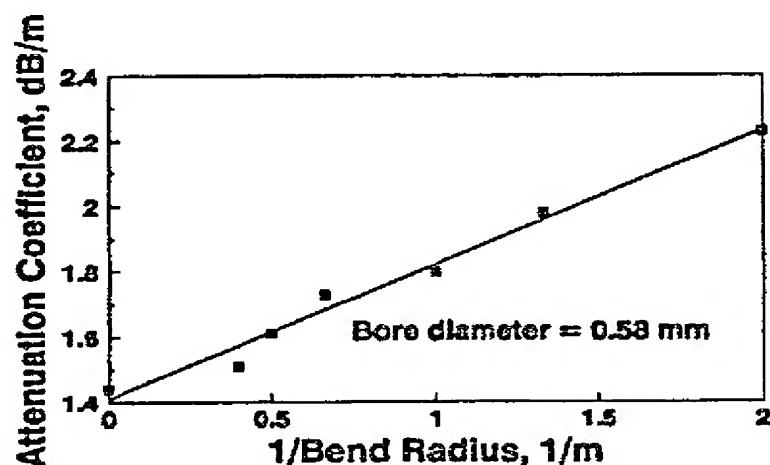

Figure 14. Bending loss for 560 μm bore, hollow sapphire tubing at 10.6 μm.
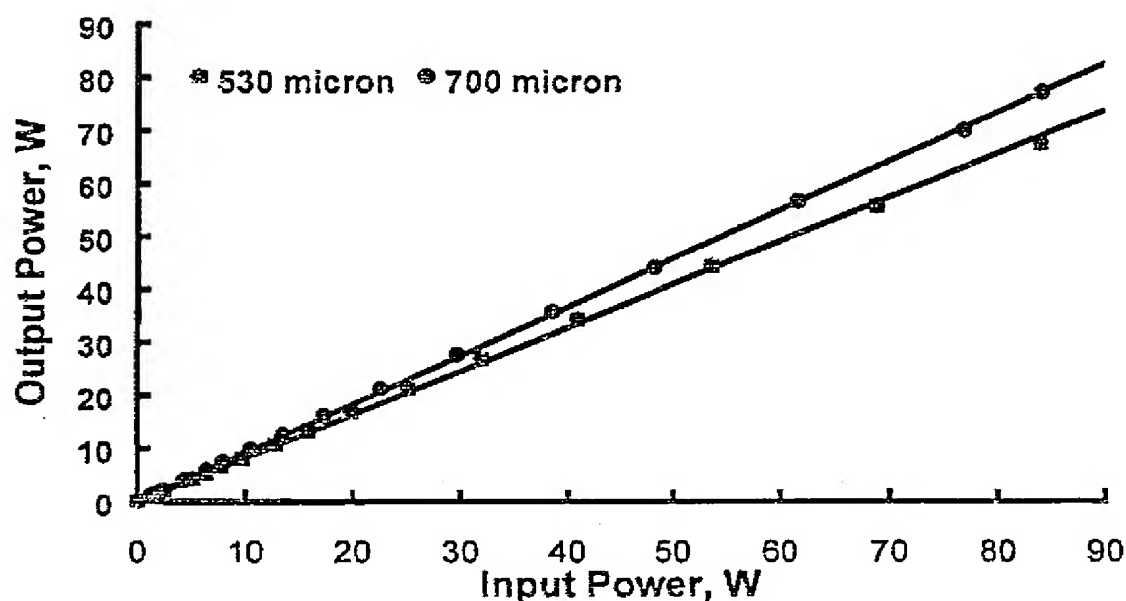
Figure 15. Low CO_2 laser power delivery for two bore size HGWs with no cooling. This is the typical laser power used in medical lasers and for low power cutting and marking.

although it is often helpful if an inert gas is used to purge the bore of the guide. In Figure 15, the results of low-power, CO_2 laser power delivery through 700 and 530 μm bore HGWs is shown. It is also possible to delivery higher CO_2 laser powers through the guides if active cooling is incorporated. In Figure 16, the results of high-power CO_2 laser transmission is shown through a 700-μm-bore HGW that
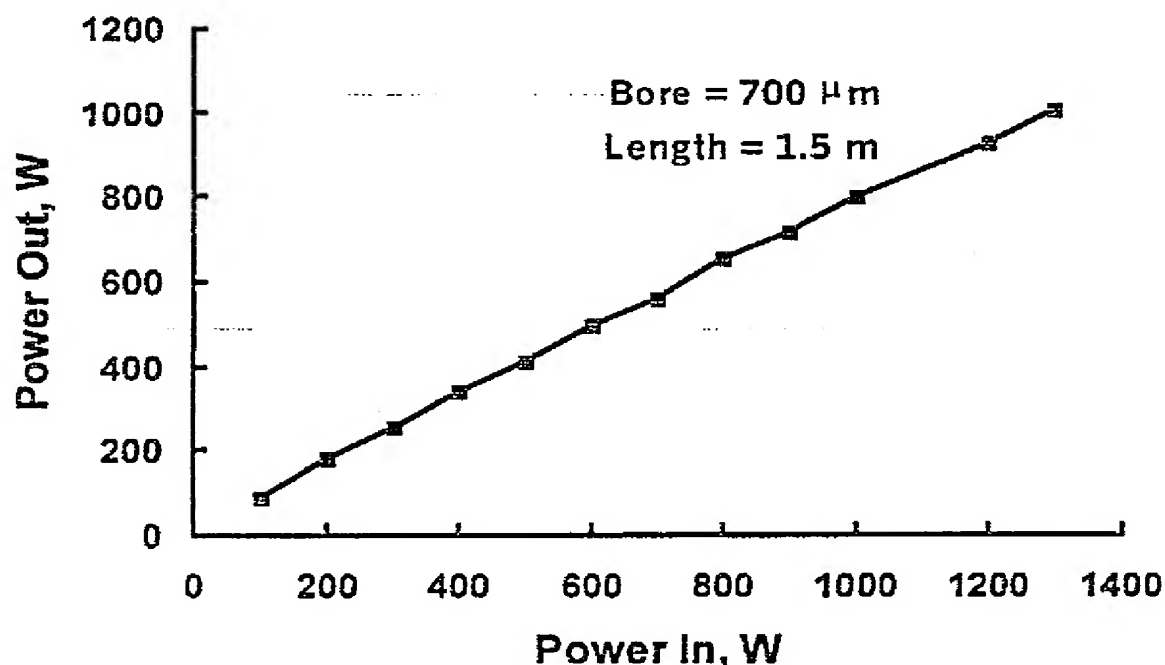

Figure 16. High CO_2 laser power delivery for a 700 μm bore HGW with a water cooling jacket. Note that the maximum power is just over 1,000 W!
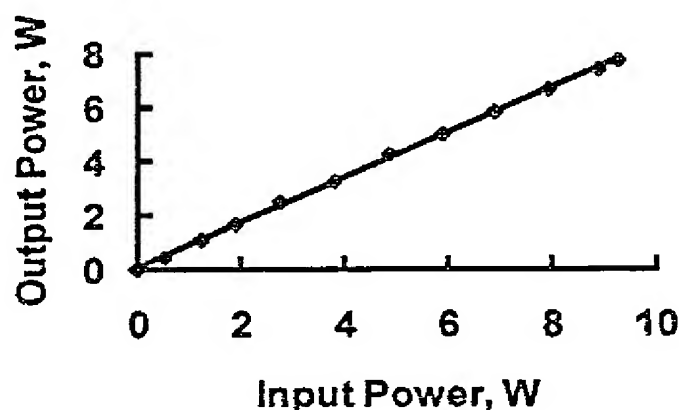
Figure 17. Power delivery though a HGW using an Er:YAG laser.

has a water jacket surrounding the guide. The maximum laser power delivered through the guide was just over 1000 W [34]!

The 2.94-μm, pulsed Er:YAG laser is becoming an important medical laser because the depth of ablation is very shallow and, therefore, this laser has great potential in surgical applications involving precise cutting and ablation. In Figure 17 the average 3 μm laser power delivered by the 1000 μm-bore HGW is shown. These data were obtained using a multimode Er:YAG laser made by Continuum. The maximum average output power of about 8 W represents a substantial average power for this wavelength. This power is sufficient for most surgical and dental applications.

The output beam profile of the HGW is important for many applications. In principle, the HGWs are nearly single-mode because the higher order modes are attenuated by the factor $(U_0)^2$ (see Eqn. 1). In practice, however, mode distortion can occur even with a $TEM_{(K)}$ input beam. The spatial profile can worsen on bending due to increased coupling into higher order modes. The amount of coupling into higher order modes is a function of the diameter of the waveguide, the roughness of the surface, and the refractive indices of the material. The spatial profile of a 530-μm-bore HGW is shown in Figures 18A and 18B. From the data one sees that it is possible to generate a single-mode HE_{11} output when the guide is straight or bent (Figure 18A), but, at other times when the guide is bent, low-order modes can be generated resulting in the modal pattern in Figure 18B. An important point is that the smaller the bore size the better the modal purity even on bending. A 250-μm bore, straight or bent guide, for example, retains a nearly perfect single mode output [35]. The near single-mode output from the glass waveguides is very important when small spot sizes are needed for precise cutting or marking.

Applications of Hollow Waveguides

Applications of hollow waveguides fall into two broad categories: laser power delivery and fiber sensors. As fiber sensors, hollow waveguides are generally used either to transmit black-body radiation for temperature measurements or as an active or passive link for chemical sensing. Saito and Kikuchi [36] give a good review of the use of hollow guides as IR fiber sensors. The use of hollow glass or
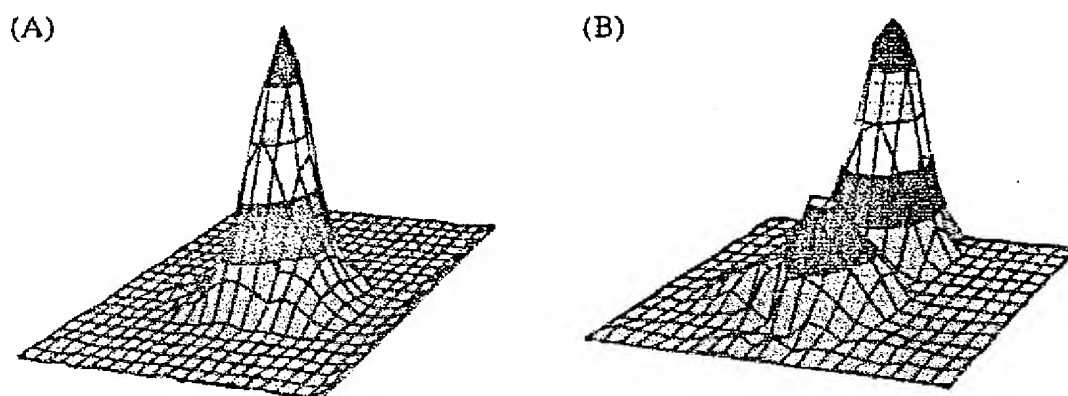
Figure 18. (A) High quality output beam profile from a bent 530 μm bore HGW and (B) A similar HGW, but with the output beam profile distorted somewhat by pushing against the side of the guide.

metallic waveguides to deliver laser power has largely been relegated to laser surgery where the required power is less than 100 W. Furthermore, most of the surgical applications to date involve the CO_2 laser, as this laser is one of the most commonly used medical lasers. As mentioned above, the HGWs are capable of delivering over a kilowatt of CO_2 laser power, yet they have not been accepted as flexible delivery systems for industrial lasers. There are two most likely explanations for this: 1. hollow guides have a somewhat higher loss when compared to current articulated arm technology; 2. industrial applications generally require a high quality (low M^2) laser output mode, whereas hollow waveguides can distort the TEM_{00} input beam of the CO_2 laser and this can lead to unacceptable kerfs and welds in cutting and welding applications.

Hollow waveguides are an ideal means of transmitting black-body radiation for thermometric measurements. In particular, the peak of black-body radiation near room temperature is around 10 μm where these guides transmit very well. They have also been used to transmit radiation above 1,000°C for the measurement of jet engine blade temperatures. As a delivery system in chemical sensing applications, hollow guides may be used merely as a passive fiber link from the chemical processing area to a remote detector, or they may play a more active role in which the guide is filled with the gas to be sensed. The latter application involves using the hollow guide itself as both the container for the gas sample and as a waveguide [26]. That is, a coiled hollow guide can replace a standard White cell to give a long pathlength and a small volume cell. Several researchers have used this method to measure small quantities of benign gases [26].

Conclusions

Hollow, IR transmitting waveguides are becoming an attractive fiber optic for the delivery of high power laser radiation as well as for important temperature and chemical fiber sensor applications. In general, these guides enjoy losses of a few tenths of a dB/m and are quite flexible. Because the energy is carried in the hollow core, there is no core material that might be easily damaged by high peak or average laser powers as there would be in a comparable solid-core IR fiber. In

addition, there is no Fresnel loss; this is especially important in comparison to the chalcogenide glass fibers, where Fresnel losses can be as high as 25%/surface. When selecting a hollow guide, it is important to remember that the optical principles are different between a hollow core guide and a solid-core fiber. The most important distinctions are that the hollow guides have a loss that varies as the reciprocal of the bore radius cubed and that there is an additional loss on bending which varies as $1/R$. These properties are not shared by conventional solid-core fibers. It is the authors' experience, however, that most applications of IR fibers do not require tight bending radii so that the additional loss on bending is not prohibitive. Two other advantages of hollow guides are important: these guides are nearly single mode and there seems to be no loss due to aging as no change in transmission has been observed after storage of the guides for over 2 years.

References

1. Kapany, N. S., and R. J. Simms. 1965. Recent developments of infrared fiber optics. *Infrared Phys.* 5:69–75.
2. Harrington, J. A. 1990. *Selected papers on infrared fiber optics*, Milestone Series, Volume MS-9, Bellingham, WA: SPIE.
3. Sanghera, J., and I. Aggarwal. 1998. *Infrared fiber optics*. Boca Raton, FL: CRC Press.
4. France, P., M. G. Drexhage, J. M. Parker, M. W. Moore, S. F. Carter, and J. V. Wright. 1990. *Fluoride glass optical fibres*. London: Blackie.
5. Aggarwal, I., and G. Lu. 1991. *Fluoride glass optical fiber*. New York: Academic Press.
6. Katsuyama, T., and H. Matsumura. 1989. *Infrared optical fibers*. Bristol: Adam Hilger.
7. Saggese, S. J., J. A. Harrington, and G. H. Sigel, Jr. 1991. Attenuation of incoherent infrared radiation in hollow sapphire and silica waveguides. *Opt. Lett.* 16:27–29.
8. Saito, M., Y. Matsuura, M. Kawamura, and M. Miyagi. 1990. Bending losses of incoherent light in circular hollow waveguides. *J. Opt. Soc. Am. A* 7:2063–2068.
9. Hongo, A., K. Morosawa, K. Matsumoto, T. Shiota, and T. Hashimoto. 1992. Transmission of kilowatt-class CO_2 laser light through dielectric-coated metallic hollow waveguides for material processing. *Appl. Opt.* 31:5114–5120.
10. Matsuura, Y., and M. Miyagi. 1992. Bending losses and beam profiles of zinc selenide-coated silver waveguides for carbon dioxide laser light. *Appl. Opt.* 31:6441–6445.
11. Gregory, C. C., and J. A. Harrington. 1993. Attenuation, modal, polarization properties of $n < 1$, hollow dielectric waveguides. *Appl. Opt.* 32:5302–5309.
12. Harrington, J. A., and C. C. Gregory. 1990. Hollow sapphire fibers for the delivery of CO_2 laser energy. *Opt. Lett.* 15:541–543.
13. Marcatili, E. A. J., and R. A. Schmeltzer. 1964. Hollow metallic and dielectric waveguides for long distance optical transmission and lasers. *Bell Syst. Tech. J.* 43:1783–1809.
14. Miyagi, M., K. Harada, and S. Kawakami. 1984. Wave propagation and attenuation in the general class of circular hollow waveguides with uniform curvature. *IEEE Trans. Microwave Theory and Techniques* MTT-32:513–521.
15. Miyagi, M., and S. Kawakami. 1984. Design theory of dielectric-coated circular metallic waveguides for infrared transmission. *J. Lightwave Technology* LT-2:116–126.
16. Laakmann, K. D., and M. B. Levy. 1991. U.S. Patent No. 5,005,944.
17. Miyagi, M., A. Hongo, Y. Aizawa, and S. Kawakami. 1983. Fabrication of germanium-coated nickel hollow waveguides for infrared transmission. *Appl. Phys. Lett.* 43:430–432.
18. Croitoru, N., J. Dror, and I. Gannot. 1990. Characterization of hollow fibers for the transmission of infrared radiation. *Appl. Opt.* 29:1805–1809.
19. Abel, T., J. Hirsch, and J. A. Harrington. 1994. Hollow glass waveguides for broadband infrared transmission. *Opt. Lett.* 19:1034–1036.

20. Garmire, E., T. McMahon, and M. Bass. 1980. Flexible infrared waveguides for high-power transmission. *IEEE J. Quantum Electron.* QE-16:23–32.
21. Kubo, U. 1994. Medical applications of optical fibers. *Review of Laser Engineering* 2:329–337.
22. Matsuura, Y., and M. Miyagi. 1993. Er:YAG, CO, and CO_2 laser delivery by ZnS-coated Ag hollow waveguides. *Appl. Opt.* 32:6598–6601.
23. Machida, H., Y. Matsuura, H. Ishikawa, and M. Miyagi. 1992. Transmission properties of rectangular hollow waveguides for CO_2 laser light. *Appl. Opt.* 31:7617–7622.
24. Bhardwaj, P., O. J. Gregory, C. Morrow, G. Gu, and K. Burbank. 1993. Performance of a dielectric-coated monolithic hollow metallic waveguide. *Mater. Lett.* 16:150–156.
25. Dahan, R., J. Dror, and N. Croitoru. 1992. Characterization of chemically formed silver iodide layers for hollow infrared guides. *Mater. Res. Bull.* 27:761–766.
26. Haan, D. J., and J. A. Harrington. 1999. Hollow waveguides for gas sensing and near-IR applications. In *Specialty Fiber Optics for Medical Applications*, eds. A. Katzir and J. A. Harrington, Proc. SPIE, Vol. 3596, 43–49.
27. Alaluf, M., J. Dror, R. Dahan, and N. Croitoru. 1992. Plastic hollow fibers as a selective infrared radiation transmitting medium. *J. Appl. Phys.* 72:3878–3883.
28. Matsuura, Y., T. Abel, and J. A. Harrington. 1995. Optical properties of small-bore hollow glass waveguides. *Appl. Opt.* 34:6842–6847.
29. Matsuura, K., Y. Matsuura, and J. A. Harrington. 1996. Evaluation of gold, silver, and dielectric-coated hollow glass waveguides. *Opt. Eng.* 35:3418–3421.
30. Matsuura, Y., A. Hongo, and M. Miyagi. 1990. Dielectric-coated metallic hollow waveguide for 3-μm Er:YAG, 5-μm CO, and 10.6-μm CO_2 laser light transmission. *Appl. Opt.* 29:2213–2217.
31. Hidaka, T., T. Morikawa, and J. Shimada. 1981. Hollow-core oxide-glass cladding optical fibers for middle-infrared region. *J. Appl. Phys.* 52:4467–4471.
32. Hidaka, T., J. Kumada, J. Shimada, and T. Morikawa. 1982. GeO_2-ZnO-K_2O glass as the cladding material of 940-cm^{-1} CO_2 laser-light transmitting hollow-core waveguide. *J. Appl. Phys.* 53:5484–5490.
33. Worrell, C. A. 1989. Transmission properties of some hollow glass waveguides at 10.6 μm wavelength. *Elect. Lett.* 25:570–571.
34. Nubling, R., and J. A. Harrington. 1996. Hollow-waveguide delivery systems for high-power, industrial CO_2 lasers. *Appl. Opt.* 34:372–380.
35. Matsuura, Y., T. Abel, J. Hirsch, and J. A. Harrington. 1995. Small-bore hollow waveguide for delivery of near single-mode IR laser radiation. *Electron. Lett.* 30:1688–1690.
36. Saito, M., and K. Kikuchi. 1997. Infrared optical fiber sensors. *Optical Review* 4:527–538.

Biography

James A. Harrington is Professor of Ceramic and Materials Engineering at Rutgers University in Piscataway, NJ. Dr. Harrington's basic research interests are in the area of specialty fiber optics and the optical properties of solids. Since 1977, he has worked on all aspects of infrared fibers, including fabrication, characterization, and applications. His current research interests include the development of IR fiber optics for use in the delivery of laser power in surgical and industrial applications and for use as chemical and thermal fiber sensors. Specifically, these fibers include hollow glass waveguides and single-crystal sapphire fibers.

RAPID COMMUNICATIONS

Template-directed vapor–liquid–solid growth of silicon nanowires

Kok-Keong Lew, Cordula Reuther, Altaf H. Carim, and Joan M. Redwing[a)]
Department of Materials Science and Engineering, Materials Research Institute, The Pennsylvania State University, University Park, Pennsylvania 16802

Benjamin R. Martin
Department of Chemistry, The Pennsylvania State University, University Park, Pennsylvania 16802

The synthesis of Si nanowires in nanoporous anodic alumina membranes was demonstrated using a combination of Au electrodeposition and vapor–liquid–solid growth at 500 °C using SiH_4 as the Si source. The average diameter of the nanowires was 200 ± 54 nm which was close to the pore size distribution of the membranes. High-resolution transmission electron microscopy revealed that the nanowires consist of a crystalline Si core, oriented in the $\langle 100 \rangle$ or $\langle 211 \rangle$ growth direction, with a thin (<3 nm) native oxide coating. In this process, Au terminates both ends of the growing wires, resulting in the formation of Au–Si–Au nanowires. © 2002 American Vacuum Society. [DOI: 10.1116/1.1430240]

I. INTRODUCTION

There is currently intense interest in one-dimensional nanostructures, such as nanotubes and nanowires, due to their potential to test fundamental concepts of dimensionality and to serve as building blocks for nanoscale devices.[1] Carbon nanotubes have been the focus of much of this work, however, it has proven difficult to control conductivity in these structures[2,3] which restricts their application. As a result, there is renewed interest in the synthesis and properties of semiconductor nanowires, such as Si, Ge, and GaAs, and the development of assembly methods to fabricate functional nanoscale electronic[4,5] and optical devices[6] using these structures.

The electrical and optical properties of semiconductor nanowires strongly depend on the wire diameter[7] as well as the crystallographic orientation[8] and defect structure of the material. Synthesis techniques have therefore been directed at producing large quantities of single crystal nanowires with uniform diameters and controlled growth orientations. In one approach, nanoporous materials, such as anodized aluminum, have been used as templates for nanotube and nanowire synthesis via electrodeposition[9,10] or chemical vapor deposition.[11,12] Template-directed synthesis affords good control over nanowire diameter and uniformity and provides a support structure for the fabrication of multi-layered nanowires.[13] Direct deposition into nanopores, however, typically yields polycrystalline material. Alternatively, vapor–liquid–solid (VLS) growth has been used to produce single crystal semiconductor nanowires such as Si[14] and GaAs.[15] In the VLS growth of Si nanowires, a metal, such as gold (Au) is used as a catalyst agent to nucleate whisker growth from a Si-containing vapor.[16] Au and Si form a liquid alloy that has a eutectic temperature of 363 °C, which, upon supersaturation, nucleates the growth of a Si wire. The fabrication of nanometer-size wires can be achieved through careful control of the metal particle size and the growth conditions.[17] VLS growth of Si nanowires has been demonstrated using techniques in which the metal particles were either fabricated by metal deposition and photolithography on a Si surface,[18] produced in the gas phase via laser ablation[19,20] or evaporation,[21] or were in the form of nanocrystals suspended in a supercritical solution.[22] These methods yield crystalline Si nanowires and afford some degree of control over the wire diameter. However, given the lack of a support structure for nanowire fabrication, it is difficult to produce multi-layered nanowires using these techniques.

This report demonstrates the synthesis of Si nanowires by VLS growth in nanoporous anodic alumina membranes. By combining template-directed synthesis with VLS growth, this technique provides a simple method to produce large quantities of crystalline Si nanowires with uniform diameters that are determined by the pore size of the membrane. Furthermore, by combining metal electrodeposition with VLS growth in nanoporous membranes, this technique enables the fabrication of metal-Si-metal nanowires.

II. EXPERIMENT

Commercially available anodic alumina membranes (Whatman Scientific) with a nominal pore diameter of 200 nm and thickness of 60 μm were used as templates in this initial study. Alumina membranes with pore diameters ranging from 4 nm to greater than 200 nm can be produced through the anodization of aluminum in various acids as described by Routkevitch *et al.*[23] The Au catalyst for VLS

[a)]Electronic mail: jmr31@psu.edu

growth was electrodeposited into the membranes using a process described by Martin *et al.*[24] In order to control the placement of the Au catalyst relative to the top surface of the pore, a 10–30 μm long segment of silver (Ag) was initially deposited in the pores, followed by a thin (0.2–1.2 μm) segment of Au. The Ag was then removed by etching in 8.0 M HNO$_3$, leaving only the thin Au segment near the center of the membrane. The membrane was cleaned with distilled water in an ultrasonic bath and dried under ambient conditions. Vapor–liquid–solid growth was carried out at 500 °C in a low pressure, isothermal reactor using a 5% mixture of SiH$_4$ in H$_2$.

Plan view and cross sectional images of the membranes after VLS growth were analyzed using a 30 kV Philips XL20 scanning electron microscope (SEM). A transmission electron microscope (TEM) sample was prepared by scraping a portion of the nanowires off the top surface of the membrane onto a TEM grid. High-resolution transmission electron microscope (HREM) images and electron diffraction patterns of the Si nanowires were recorded at 200 kV using a Hitachi HF2000 field emission transmission electron microscope.

III. RESULTS AND DISCUSSION

In traditional VLS growth, the metal particle is either supported on a surface or produced in the gas phase and is readily accessible to the vapor phase growth species. In our application, the gold catalyst was buried deep within the pore. Consequently, a careful choice of reaction conditions was required to ensure that the vapor phase species diffused far into the pore and preferentially reacted with the metal catalyst rather than the internal walls of the pore or the top surface of the membrane. A model of gas phase diffusion and reaction in a cylindrical pore[25] was used to predict the SiH$_4$ concentration profile within a 200 nm diameter pore as a function of temperature and pressure in order to define initial conditions for VLS growth. At a pressure of 10 Torr, SiH$_4$ was predicted to diffuse the entire pore length (60 μm) with minimal Si deposition for temperatures less than 600 °C. In order to extend this technique to 10 nm diameter pores, the growth temperature must be reduced to less than 400 °C to prevent Si deposition on the internal walls of the pore. Initial growth experiments, carried out at 500 °C, 13 Torr total pressure and a SiH$_4$ partial pressure of 0.65 Torr, on membranes that did not contain Au resulted in negligible Si deposition on the membrane surfaces for growth times up to 45 min.

Growth experiments were then carried out under identical conditions (500 °C, 13 Torr, 0.65 Torr SiH$_4$) using the Au-impregnated nanoporous anodic alumina membranes. Gold catalyzes the decomposition of SiH$_4$ under these conditions resulting in the rapid growth of Si nanowires within the pores. Nanowires began to emerge from the top of the pores after approximately 15 min [Fig. 1(a)] and populated the surface after 20 min of growth [Fig. 1(b)]. Si nanowires were observed growing in nominally every pore of the membrane. The presence of Au at the tip of the nanowires, as confirmed
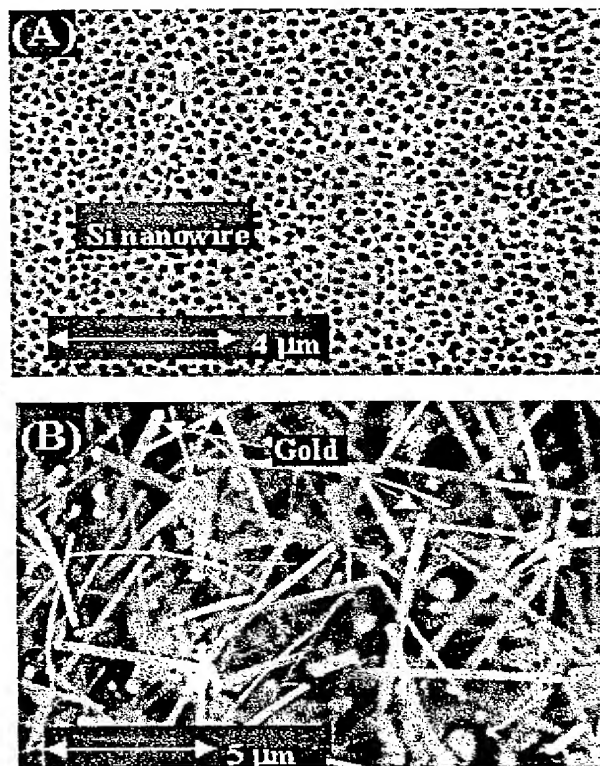

FIG. 1. Scanning electron microscopy images of the top surface of Au-impregnated alumina membranes during various stages of VLS growth from the nanopores. After 15 min (A) Si nanowires began to emerge from the pores and fully covered the surface after 20 min (B). Gold balls present at the tips of the nanowires in (B) are evidence of a VLS growth mechanism.

by energy dispersive x-ray spectroscopy, provided evidence of a VLS growth mechanism.

During growth, the Si nanowire fills the entire internal diameter of the pore and pushes a portion of the Au–Si alloy toward the pore surface as the wire grows in length. As a result, the final diameter of the Si nanowire is determined exclusively by the initial diameter of the pore. The pore diameter of the anodic alumina membranes ranged from 110 nm to 270 nm (sample of 280 pores) with an average diameter of 194 ± 33 nm. Correspondingly, the diameter of the Si nanowires ranged from 100 nm to 340 nm (sample of 50 nanowires) with an average diameter of 200 ± 54 nm.

A low magnification TEM image of a sample of nanowires removed from the membrane surface is shown in Fig. 2. The long wire near the center of the image is aligned with the beam parallel to the $[01\bar{1}]$ zone axis. The growth direction of the nanowire is [100]. Crystallographic analysis of the TEM images revealed Si nanowires characterized by two distinct growth axes: $\langle 100 \rangle$ and $\langle 211 \rangle$. The $\langle 211 \rangle$ orientation has previously been observed in Si nanowires fabricated by VLS growth from a surface[26] or via laser ablation,[19,20] while $\langle 100 \rangle$-oriented wires were obtained in supercritical fluid growth.[22] HREM analysis of the Si nanowires, shown in Fig. 3, revealed a nearly defect-free Si core with a 2–3 nm thick amorphous native oxide coating. All of the $\langle 100 \rangle$-oriented
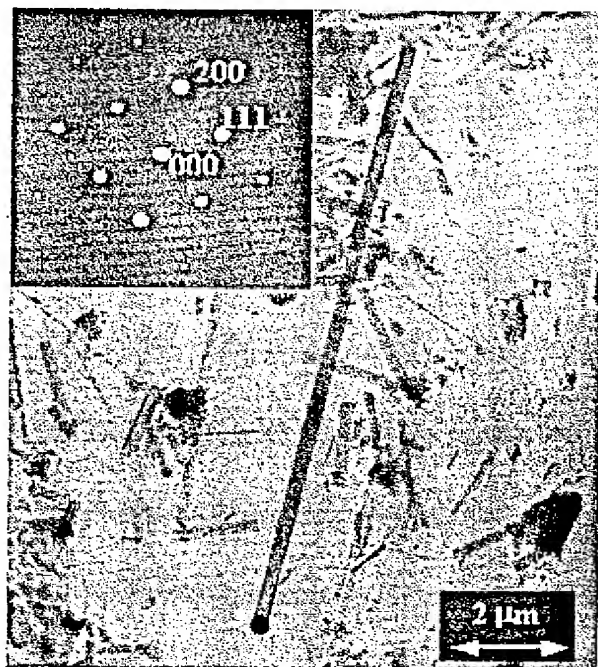
FIG. 2. Low magnification transmission electron microscopy (TEM) image of nanowires removed from the top surface of the membrane and supported on a grid. The insert is the parallel-beam diffraction pattern along the [01$\bar{1}$] zone axis of the Si nanowire shown at the center of the image, which has a [100] growth direction.

wires observed thus far by TEM appear to be single crystals, based on diffraction contrast imaging, high-resolution imaging, and electron diffraction.

The nanowires were removed from the anodic alumina membranes by wet etching in 5.0 M NaOH for approximately two hours at room temperature. Figure 4 is a SEM photo of a Au–Si–Au nanowire produced by template-directed VLS growth after removal from the membrane. In this case, the initial gold segment in the membrane was 1.2 μm long and the growth time sufficiently short (15 min) so
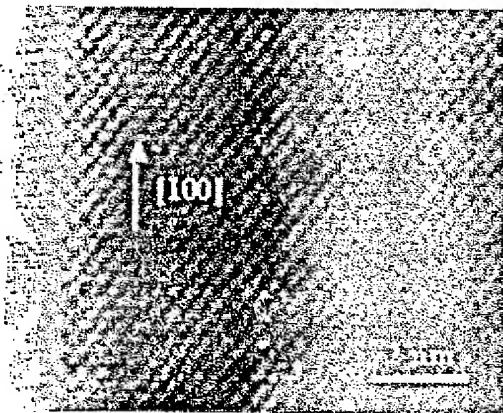

FIG. 3. High-resolution transmission electron microscopy (HREM) image near the edge of a nanowire. A thin (<3 nm) sheath of amorphous native oxide was found at the edge of the nanowire.
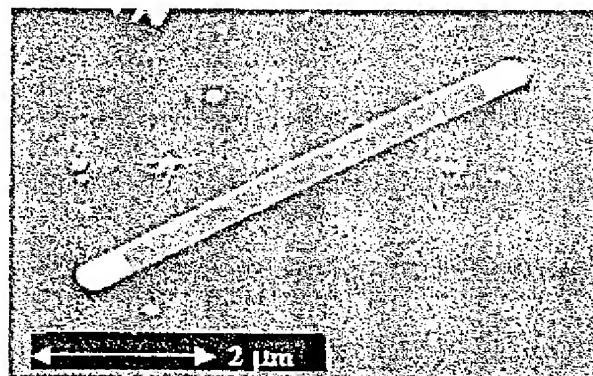

FIG. 4. Scanning electron microscopy image of a Au–Si–Au nanowire after release from the membrane by wet etching. Both ends of the nanowire are capped with approximately 0.6 μm long segments of Au.

that the length of the wire did not extend beyond the top surface of the membrane. As shown in Fig. 4, the nanowire consists of an approximately 4 μm long central region of Si with 0.6 μm long segments of Au at each end of the nanowire. Gold tips are always observed at both ends of the Si nanowires produced in this process. These results indicate that Si nucleates near the center of the Au–Si liquid alloy in this process and the crystal grows outward along the pore axis, leaving a segment of Au at each end of the nanowire. This is in contrast to Si nanowires produced by VLS growth from a surface[18] or by laser ablation[20] in which the metal particle is present at only one end of the wire. Interactions between the liquid alloy drop and the internal pore walls are likely responsible for the modification in VLS growth observed in this study.

IV. CONCLUSIONS

The fabrication of Si nanowires has been demonstrated using a combination of template-directed synthesis and VLS growth. The use of nanopores for VLS growth provides control over nanowire diameter while also enabling the production of single crystal material. This work demonstrated the synthesis of nominally 200 nm diameter Si nanowires in nanoporous anodic alumina membranes using electrodeposited Au as the metal catalyst for VLS growth. The nanowires consist of a crystalline Si core with a ⟨100⟩ or ⟨211⟩ growth direction surrounded by a thin (<3 nm) oxide coating. The ends of the Si nanowires are capped with segments of Au, which result from the VLS mechanism of growth. It is anticipated that this technique can be extended to the synthesis of smaller diameter nanowires through the use of anodized aluminum oxide templates with pore sizes in the range of 10–100 nm.[9] The results of this study demonstrate the potential for using template-directed VLS growth in combination with metal electrodeposition for the fabrication of single crystal Si nanowires and multi-layered metal-Si-metal nanowires.

ACKNOWLEDGMENTS

[1]C. Dekker, Phys. Today 52, 22 (1999).

[2]T. W. Odom, J. L. Huang, P. Kim, and C. M. Leiber, Nature (London) 391, 62 (1998).

[3]J. W. G. Wildöer, L. C. Venema, A. G. Rinzler, R. E. Smalley, and C. Dekker, Nature (London) 391, 59 (1998).

[4]S. W. Chung, J. Y. Yu, and J. R. Heath, Appl. Phys. Lett. 76, 2068 (2000).

[5]Y. Cui and C. M. Lieber, Science 291, 851 (2001).

[6]X. Duan, Y. Huang, Y. Cui, J. Wang, and C. M. Lieber, Nature (London) 409, 66 (2001).

[7]L. Brus, J. Phys. Chem. 98, 3575 (1994).

[8]H. Yorikawa, H. Uchida, and S. Muramatsu, J. Appl. Phys. 79, 3619 (1996).

[9]D. Al-Mawlawi, C. Z. Liu, and M. Moskovits, J. Mater. Res. 9, 1014 (1994).

[10]D. Xu, X. Shi, G. Guo, L. Gui, and Y. Tang, J. Phys. Chem. B 104, 5061 (2000).

[11]J. Li, C. Papadopoulos, J. M. Xu, and M. Moskovits, Appl. Phys. Lett. 75, 367 (1999).

[12]K. B. Shelimov and M. Moskovits, Chem. Mater. 12, 250 (2000).

[13]D. Routkevitch, A. A. Tager, J. Haruyama, D. Almawlawi, M. Moskovits, and J. M. Xu, IEEE Trans. Electron Devices 43, 1646 (1996).

[14]J. Westwater, D. P. Gosain, S. Tomiya, S. Usui, and H. Ruda, J. Vac. Sci. Technol. B 15, 554 (1997).

[15]K. Hiruma, M. Yazawa, T. Katsuyama, K. Ogawa, K. Haraguchi, M. Koguchi, and H. Kakibayashi, J. Appl. Phys. 77, 447 (1995).

[16]R. S. Wagner and W. C. Ellis, Appl. Phys. Lett. 4, 89 (1964).

[17]E. I. Givargizov, J. Cryst. Growth 31, 20 (1975).

[18]J. Westwater, D. P. Gosain, and S. Usui, Jpn. J. Appl. Phys. 36, 6204 (1997).

[19]A. M. Morales and C. M. Lieber, Science 279, 208 (1998).

[20]Y. F. Zhang, Y. H. Tang, N. Wang, D. P. Yu, C. S. Lee, I. Bello, and S. T. Lee, Appl. Phys. Lett. 72, 1835 (1998).

[21]D. P. Yu, Z. G. Bai, Y. Ding, Q. L. Hang, H. Z. Zhang, J. J. Wang, Y. H. Zou, W. Qian, G. C. Xiong, H. T. Zhou, and S. Q. Feng, Appl. Phys. Lett. 72, 3458 (1998).

[22]J. D. Holmes, K. P. Johnston, R. C. Doty, and B. A. Korgel, Science 287, 1471 (2000).

[23]D. Routkevitch, J. Chan, J. M. Xu, and M. Moskovits, Electrochem. Soc. Proc. 97, 350 (1997).

[24]B. R. Martin, D. J. Dermody, B. D. Reiss, M. Fang, L. A. Lyon, M. J. Natan, and T. E. Mallouk, Adv. Mater. 11, 1021 (1999).

[25]E. Fitzer, W. Fritz, and G. Schoch, J. Phys. IV 1, 143 (1991).

[26]J. Y. Yu, S. W. Chung, and J. R. Heath, J. Phys. Chem. B 104, 11 864 (2000).